8-31-2011

Effects of non-planar distortions in porphyrin compounds on their properties and functionality

Raid Haddad

Recommended Citation

Haddad, Raid. "Effects of non-planar distortions in porphyrin compounds on their properties and functionality." (2011).
https://digitalrepository.unm.edu/cbe_etds/14

Raid Haddad
Candidate

Chemical & Nuclear Engineering
Department

This dissertation is approved, and it is acceptable in quality and form for publication:

Approved by the Dissertation Committee:

Plamen Atanassov, Chairperson

John A Shelnutt, Co-Chair

EFFECTS OF NON-PLANAR DISTORTIONS IN PORPHYRIN COMPOUNDS ON THEIR PROPERTIES AND FUNCTIONALITY

BY

RAID E. HADDAD

B.S., Chemical Engineering, University of New Mexico, 1996

DISSERTATION

Submitted in Partial Fulfillment of the
Requirements for the Degree of

Doctor of Philosophy
Engineering

The University of New Mexico
Albuquerque, New Mexico

May 2011

DEDICATION

I dedicate this dissertation to my two children, Iman and Daniel, who are my source of joy and my inspiration. I thank my wife, Dalila, for her patience and sacrifices, and for her unconditional love. This work would not be possible without the love and support of my parents who always believed in me and taught me to persevere.

ACKNOWLEDGEMENTS

I gratefully acknowledge, first of all, my research advisor Dr. John Shelnutt, for his guidance and support throughout my PhD research. Not only is he is a scientist of exceptional brilliance but also a wonderful mentor and a very humble person who treats his mentees as equals and cares for their wellbeing; I am honored to call him a friend. I am also very grateful to Dr. Plamen Atanassov, my dissertation committee chair, whose advice and encouragement were invaluable to me, and who will always go to great lengths to help his students. Very special thanks also to Dr. Hongyou Fan, with whom I worked for a couple of years and collaborated on many projects. He is a terrific research advisor, a great motivator, and a true friend. Thanks also to dissertation committee members Dr. Steven Graves and Dr. John Grey for their time in reviewing my dissertation.

I would also like to thank my research group members for their guidance and helpful discussions. Dr. Craig Medforth was involved in all the projects in this dissertation and was very much like a second mentor together with Dr. Shelnutt. Dr. Yi Lu helped train me on the spectrometers and show me around the lab when I joined the group. Mrs. Yan Qiu was also very helpful in the lab and with administrative tasks. Mr. Lisong Sun helped to modify part of the NSD code for my research. Dr. Yujiang Song and Dr. Zhongchun Wang also worked together with me on several projects.

Finally, I would like to thank our collaborators Dr. Frank van Swol, Dr. Sivakumar Challa, Dr. Jeffrey Brinker and his group, and members of the Fan group.

EFFECTS OF NON-PLANAR DISTORTIONS IN PORPHYRIN COMPOUNDS ON THEIR PROPERTIES AND FUNCTIONALITY

BY

RAID E. HADDAD

ABSTRACT OF DISSERTATION

Submitted in Partial Fulfillment of the
Requirements for the Degree of

Doctor of Philosophy
Engineering

The University of New Mexico
Albuquerque, New Mexico

May 2011

EFFECTS OF NON-PLANAR DISTORTIONS IN PORPHYRIN COMPOUNDS ON THEIR PROPERTIES AND FUNCTIONALITY

BY

RAID E. HADDAD

B.S., Chemical Engineering, University of New Mexico, 1996

Ph.D., Engineering, University of New Mexico, 2011

ABSTRACT

Porphyrins and related compounds are ubiquitous in nature, performing diverse functions including solar energy transduction, electron transport, molecular transport and storage, and catalysis. Due to their unique photophysical and chemical properties, they are excellent candidates for application as photosensitizers, catalysts, photocatalysts, molecular electronics and opto-electronics. Several properties of porphyrins are sensitive to small variations in their structure, and this dissertation investigates the effects of out-of-plane distortions of the macrocycle on optical properties, reactivity to axial ligands, and substituent rotation. The structure-functions relationships are examined using molecular simulations, UV-visible absorption spectroscopy, resonance Raman

spectroscopy, and normal-coordinate structural decomposition (NSD) analysis of simulated and X-ray crystal structures.

Concerning the optical properties, the view that the large red shifts seen in the optical absorption bands of peripherally crowded nonplanar porphyrins are the result of nonplanar deformations of the macrocycle had been challenged in the literature by studies suggesting that the shifts arise from substituent-induced changes in the macrocycle bond lengths and bond angles, termed in-plane nuclear reorganization (IPNR). The origins of the red shifts were here studied computationally and spectroscopically in a series of nickel or zinc *meso*-tetraalkyl porphyrins with graded amounts of ruffling deformations, as well as a series of novel bridled nickel chiroporphyrins in which ruffling deformation is determined by bridle length while other substituent effects are minimal. Using various structural restraints, the computational studies demonstrated conclusively that the large Soret band red shifts (~ 40 nm) seen for very nonplanar tetra(tert-butyl) porphyrin compared to tetra(methyl) porphyrin are primarily the result of nonplanar deformations and not IPNR. Strikingly, nonplanar deformations along the high-frequency $2B_{1u}$ and $3B_{1u}$ normal coordinates of the macrocycle are shown to contribute significantly to the observed red shifts, even though these deformations are an order of magnitude smaller than the observed ruffling ($1B_{1u}$) deformation. Other structural and electronic influences on the UV-visible band shifts are discussed and problems with the previous studies that lead to a mistaken attribution of the red shift to IPNR are examined. These results suggest that adjustment of nonplanarity may be used to tweak porphyrin properties for specific applications, and that UV-visible band shifts of tetrapyrroles in proteins are potentially useful indicators of changes in nonplanarity provided other structural and electronic factors can be eliminated.

With the aim of investigating the utility of axial ligand binding to drive porphyrinic molecular devices, the effects of nonplanarity on the axial ligation properties of nickel porphyrins were studied using again a series of *meso*-tetraalkyl porphyrins. Increased porphyrin ruffling is spectroscopically found to cause a drastic decrease in the binding affinity for pyrrolidine and piperidine, such that the affinity is greatly lowered for the tetraalkyl porphyrins porphyrins with methyl or primary alkyl groups compared to nearly planar NiTPP, and ligand binding is nearly completely inhibited for those with secondary or tertiary alkyl groups (i.e., cyclohexyl, cyclopropyl, iso-propyl, or tert-butyl). Ligand binding energies obtained from molecular mechanics calculations were in agreement with the spectroscopic results, and MM calculations determined that the lowered affinity is the result of the cores of the sterically crowded porphyrins being unable to expand and flatten to accommodate the larger high-spin nickel(II) ion. The computational studies also show that the switch to high-spin nickel has a marked effect on the conformational energy landscape of the nickel tetraalkylporphyrins; an αβαβ ruffled conformation is strongly favored for low-spin nickel, whereas different conformations of the macrocycle (e.g., αααα domed) are more energetically accessible for high-spin nickel. The possible uses of the small but energetically significant structural change at the nickel ion to drive larger structural changes in nickel porphyrin-based molecular devices are discussed. Specifically, the utility of axial ligation as a mechanism for producing a switchable molecular device (e.g., nanotweezers) was demonstrated by computational and spectroscopic studies of the bridled nickel chiroporphyrin NiBCP-8.

Porphyrins are an also an ideal platform for molecular rotors due to the versatility provided by the multiple substituent positions combined with their unique electronic and chemical properties potentially allowing several driving and switching mechanisms for rotation. Computer simulations were here used to explain the unusual experimentally observed rotational behavior of aryl substituents on porphyrins. *Meso* aryl rotational barriers might be expected to be much higher in dodecaaryl porphyrins than in tetraaryl porphyrins due to the great difference in peripheral crowding, and those NMR studies had found this indeed to be the case for the porphyrin dication (having four protons at the core). Suprisingly, however, small increases were found for the equivalent porphyrins with either nickel or zinc ions at the core. Previous studies of TArPs attributed variance in rotational barrier with core substituent to differing macrocycle nonplanar distortions caused by these substituents. However, it was shown here that the rotational barrier variance could not be accounted for merely by structural differences as observed in the static picture from x-ray crystal structures. Rather, molecular simulations showed that nonplanar deformability of the macrocycle, allowing substituents to move farther out-of-plane than their equilibrium positions, is important in lowering the activation energy for aryl-porphyrin rotation. Furthermore, uni-directional rotation, which is of technological interest since it is often considered a prerequisite for molecular motors, was demonstrated in a dodecaaryl porphyrin dication. This is likely the case for many other aryl-porphyrin rotors, particularly in similarly saddled structures.

TABLE OF CONTENTS

Chapter Page

LIST OF TABLES

Table Page

LIST OF FIGURES

Figure Page

CHAPTER 1: INTRODUCTION

1.1 Porphyrins & their Role

Nature has provided inspiration and guidance for many technological advances. This dissertation examines a fascinating class of macrocyclic compounds, the porphyrins, that is ubiquitous in nature and, akin to a biological Swiss-Army-knife, performs pivotal functions in photosynthesis, cell respiration, transport, accumulation and exchange of gases, blood cell formation processes, and pigmentation.[1] The porphyrin compound is usually part of a biological system where it is the active component of the system or in some way intimately connected with the activity of the system.

Among the best known porphyrin-based compounds in nature are hemes, chlorophylls, and vitamin B-12, and in total more than 150 different natural tetrapyrroles have been identified.[2] Moreover, the same porphyrin cofactor is often involved in several processes where the reactions involved are chemically quite distinct. For example, proteins containing heme (an iron porphyrin) serve as agents for O_2 storage and transport (myoglobin and hemoglobin), electron transport (cytochromes b and c), and O2 activation and utilization (cytochrome P450 and cytochrome oxidase).[3]

A highly interesting attribute of porphyrins is how small variations in their structure lead to wide diversity in biochemical functions.[4] For example, in the hemoglobin scaffolding, heme is used to transport oxygen around the body, whilst the minor structural deviation in the myoglobin protein scaffolding alters the reversible binding of oxygen so that heme is used to store oxygen in muscle tissue.[4] In cytochrome c, the different binding environment of heme's core iron atom allows it to cycle between +2 and +3 oxidation states, so performing the function of electron transfer for cell respiration.[4]

The capabilities of porphyrins to bind and release gases and to act as active centers in catalytic reactions, makes porphyrin appealing candidates for nanoporous catalytic materials as well as chemical and gas sensors. Their outstanding ability to mediate photo-electronic energy transfer processes, as demonstrated in photosynthesis, makes porphyrins and their supramolecular assemblies ideal candidates for applications in opto-electronics, data storage and solar cells. The possibility to tailor their physical and chemical properties at the molecular level – including very large dipole moments, polarizability, non-linear optical response, absorption spectrum, energy transfer and catalytic properties – make porphyrins and metalloporphyrins extremely versatile synthetic base materials for research projects in many areas, like electronics, opto-electronics, electrochemistry, catalysis and photophysics. [3]

In this dissertation, I will examine how variations in non-planar distortions of porphyrins impact various properties and explore how these distortions may be utilized in pertinent technological applications.

1.2 Porphyrin Structure

The porphyrin basically consists of four pyrrolic subunits, linked in a circle by four methine bridges. The porphyrin skeleton consists of four nitrogen atoms and twenty carbon atoms, numbered as shown in Figure 1.1. The figure also illustrates the three classifications of carbon atoms: α for the 8 pyrrolic carbons connected to core nitrogens (positions 1, 4, 6, 9, 11, 14, 16, 19); β for the 8 peripheral pyrrolic carbons (positions 2, 3, 7, 8, 12, 13, 17, 18); and *meso* for the 4 methine bridge (positions 5, 10, 15, 20).

This macrocycle contains 18 delocalized π-electrons, thus forming an aromatic system according to the Hückel's rule of aromaticity (4n+2 delocalized π-electrons). Despite its aromaticity, the macrocycle is highly flexible. The size of the core, together with the flexibility of the macrocycle, enables the insertion of almost any metal ion in the center, forming metalloporphyrins. Typical core metals include Fe, Zn, Mg, Cu, Ni, and Co. A metal-free porphyrin, called the free base, has two hydrogen atoms bound to opposite nitrogens.

The most basic porphyrin, porphine, has hydrogen atoms bound to all twelve peripheral carbons (the 8 β carbons and 4 *meso* carbons). The family of porphyrin compounds builds on this versatile macrocycle by introducing substituents at these twelve sites. Furthermore, the core metal may bind axial ligands depending on the metal and the availability of suitable ligands.

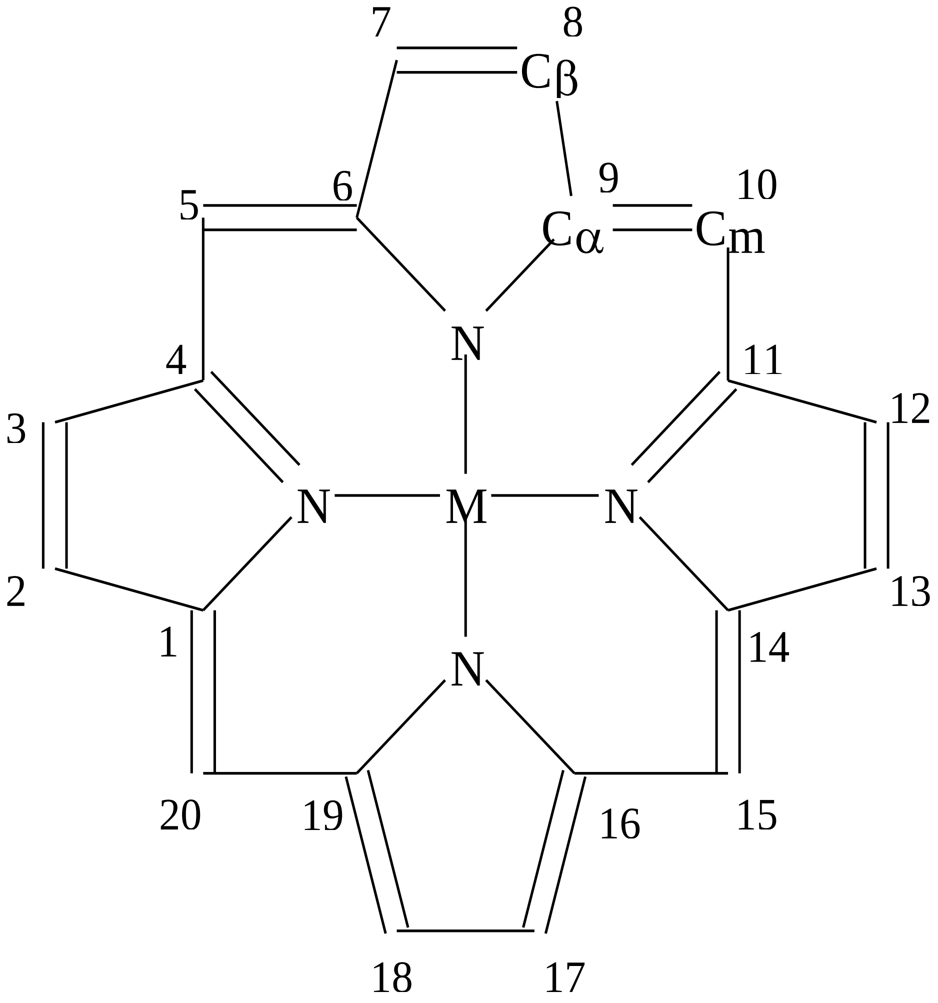

Figure 1.1 The porphyrin skeleton with the numbering scheme and the three carbon atom position types (a, β, and *meso*) indicated.

1.3 Out-of-Plane Distortions & Structure-Function Relationships

Biological studies have established that an important aspect of how porphyrin dependent biological reactions are facilitated and regulated in nature is by control of the conformations of the porphyrin macrocycles.[2] The realization that porphyrins can exhibit a considerable degree of conformational flexibility and that different macrocycle conformations result in significantly altered physicochemical properties and novel chemical reactions has given a major boost to the field of porphyrin biomimetics, allowing the development of conformationally designed systems. [2] Some of the physical and chemical properties known to be significantly altered by nonplanar distortions in porphyrins include redox and optical shifts, sites of oxidation, spin states and orbital occupancy, mixing of orbitals in cation radicals, lifetimes of excited states, and ligation and deligation photophysics.[5]

There are several chemical means by which the porphyrin macrocycle conformation may be varied, including[2]: introduction of sterically demanding substituents at some of the twelve peripheral sites; introduction of metals of different sizes at the core; addition of axial ligands to the core metal; degree of reduction; alteration of the conjugated system; N-substitution (to pyrrole nitrogens); cation radical formation; ‘‘strapping’’ of the macrocycle via covalent linkage of the *meso* or β pyrrole positions; and heteroatom substitution.

1.3.1 Classifying and Quantifying Out-of-Plane Distortions with Normal Structural Decomposition

In order to study the effects of nonplanarity and understand how it influences the properties of the porphyrin macrocycle, one needs a way to define the types of nonplanar deformation present in the porphyrin system an accurately quantify them. In early crystallographic studies of porphyrins, non-planar deformations were generally referred to as ruffling, and more useful definitions did not emerge until the work of Scheidt in the late 1980s.[6] Ruffling (*ruf*) then took on a more specific meaning, namely, an alternate clockwise or anticlockwise twisting of the pyrrole rings such that the meso carbon atoms are displaced alternately above or below the porphyrin plane (see Figure 1.2). In contrast, saddling (*sad*) was defined as an alternate up or down tilting of the pyrrole rings of the porphyrin macrocycle.

The Shelnutt group has developed[7,8] an effective method for uniquely identifying and quantifying the distortions of tetrapyrroles. In this normal-coordinate structural decomposition (NSD) analysis, distortions are represented in terms of the 66 vibrational modes, both out-of-plane and in-plane, of the molecule. NSD is used extensively in this dissertation to obtain a detailed analysis of the deformations present in the calculated porphyrin structures.

The six lowest frequency (softest) out-of-plane deformations are depicted in Figure 1.2. Besides saddling and ruffling (described above), these include doming (*dom*), waving (*wav*) in x and y directions, and propelling (*pro*). Doming is the deformation in which all pyrrole rings tilt up or all tilt down. In the waving (wav) deformation, one pyrrole ring tilts up and the opposite one tilts down. In propelling (pro), all pyrroles are twisted in the same direction like the blades of a propeller.

While the NSD analysis determines the contribution of all 66 in-plane and out-of-plane normal coordinates of the macrocycle to a distorted porphyrin structure, a combination of the displacements for just the six lowest frequency deformations mentioned above frequently provides a reasonably accurate picture of the out-of-plane distortion of the porphyrin. It is not surprising that these deformations are expected to predominate in the observed porphyrin structures because these modes are the softest ones for distortion of the porphyrin, i.e., the restoring forces and the macrocyclic distortion energies are the smallest for displacements along these normal coordinates. In particular, the ruffling and saddling deformations corresponding to the two lowest frequency out-of-plane vibrational modes of the porphyrin macrocycle most commonly observed in porphyrin crystal structures.[7] Doming is also often observed, particularly for metalloporphyrins where the metal takes a fifth (axial) ligand.[9]

Saddling, *sad* (B2u) Ruffling, *ruf* (B1u)

Doming, *dom* (A2u) x-Waving, *wav(x)* (Eg_x)

y-Waving, *wav(y)* (Eg_y) Propellering, *pro* (A2u)

Figure 1.2 Illustrations of the six lowest-frequency out-of-plane deformation modes used to decompose porphyrin structures in the NSD procedure,[10] with abbreviations and symmetry types indicated. Static displacements represent approximately a 1-Å deformation along each mode.

CHAPTER 2: METHODOLOGY

2.1 Spectroscopy

Among the most studied aspects of porphyrins and their relatives, both biologically and technologically, have been their fascinating photophysical properties, and Chapter 3 of this dissertation will examine the relation of porphyrins' optical properties to non-planar deformations of the macrocycle. Because of the intense interaction of porphyrins with light, spectroscopy provides an excellent tool for studying them and probing their structure.

2.1.1 Optical Absorption (UV-vis) Spectra and Electronic Structure

Among the most studied aspects of porphyrins and their relatives, both biologically and technologically, have been their fascinating optical properties. The various intense colors arise from their absorption properties, and Chapter 3 of this dissertation will examine the relation of the absorption of light to non-planar deformations of the macrocycle. Figure 2.1 shows the UV-vis absorption spectrum of nickel porphine, a typical metalloporphyrin spectrum illustrating the characteristic peaks. The most significant peaks are the B and Q bands, using the nomenclature of Platt.[11] The B band, commonly referred to as the Soret band after its discoverer, is an exceedingly intense band between approximately 380 and 450 nm. Slightly to the left (blue) of this

B(0,0) band of electronic origin, better-resolved spectra may show another band, denoted B(1,0), that is attributed to addition of a vibrational excitation mode. The Q bands appear in the region between approximately 500 and 600 nm. The lower-energy band of electronic origin is denoted Q(0,0) (or α) and the higher-energy band including vibrational excitation is denoted Q(1,0) (or β). The positions and relative intensities of the major bands depend strongly on the central metal ion, as well as on the porphyrin peripheral substituents, the spin state of the central metal ion and the axial ligands.

It is worth noting that the spectra of free base porphyrins (where the core metal ion is replaced by two protons) resemble those of metalloporphyrins, but the fact that they possess a two-fold symmetry rather than 4-fold leads to separation of some transitions that are degenerate for the metalloporphyrins; some bands will hence be split, resulting in four Q bands. Protonation with acid to form a porphyrin dication (two additional protons on the core nitrogens) will again raise the symmetry and the four Q bands collapse to two.

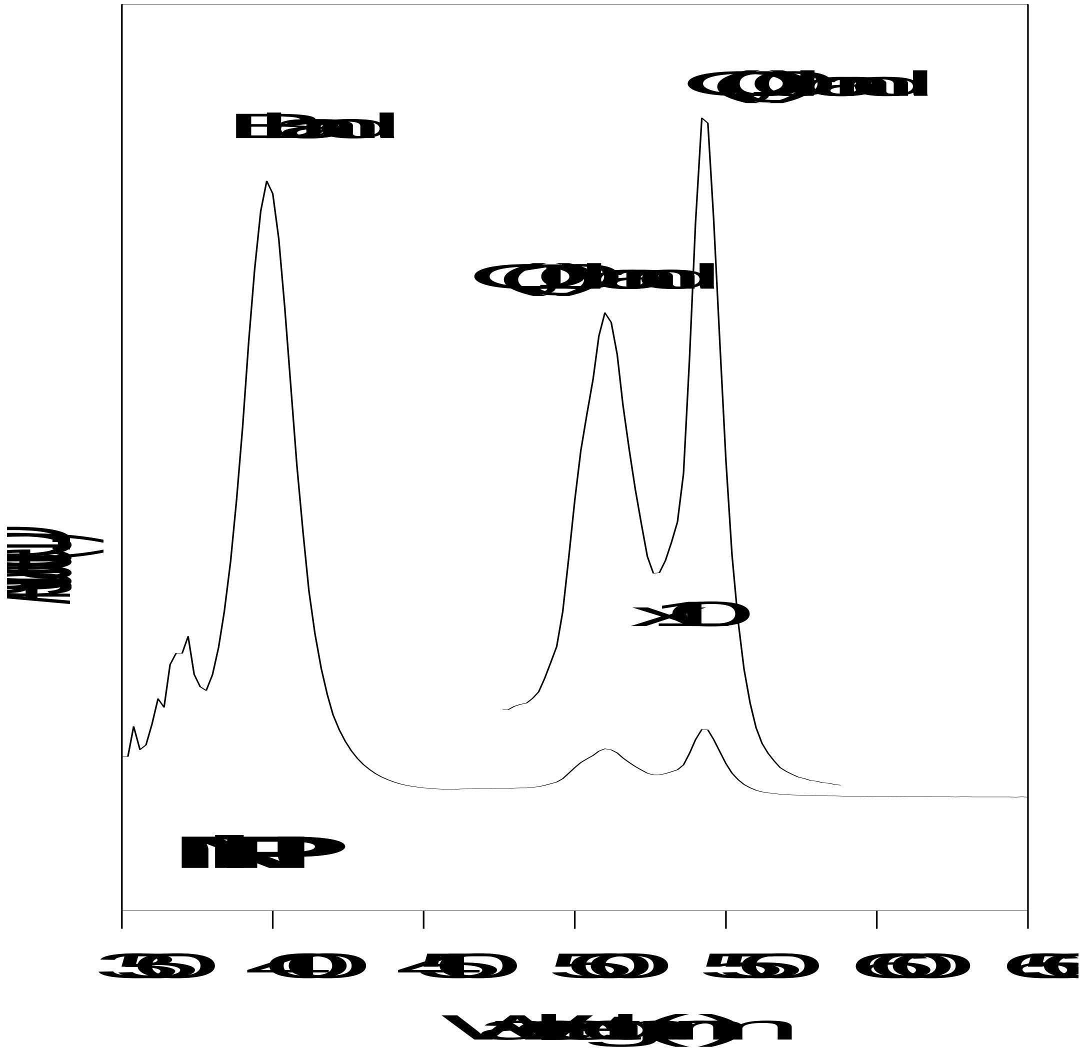

Figure 2.1 UV-visible absorption spectrum of nickel porphine (NiP) in CS_2.[12] Q bands are magnified for clarity.

Because of the importance of porphyrins and their relatives, there have been many attempts to theoretically explain their absorption spectra, historically including free electron theory, cyclic polene theory, and simple Hückel theory.[4] A model using configuration interaction was developed by Gouterman,[13,14] and although more sophisticated models have now superseded it,[4] it still provides an useful qualitative picture for understanding the electronic basis for the major features of porphyrin spectra.

Gouterman's model is called the four-orbital model, as it considers the two highest occupied molecular orbitals (HOMOs) and the two lowest unoccupied molecular orbitals (LUMOs). The orbitals are pictorially illustrated in Figure 2.2. The HOMOs, labeled a_{2u} and a_{1u} for their symmetry, are nearly degenerate (equal in energy) and the LUMOs, labeled $e_{g,x}$ and $e_{g,y}$, are degenerate under idealized four-fold (D_{4h}) symmetry (in fact, they are equivalent by a rotation, hence the sub-labels x & y). The B and Q electronic states result from $\pi \rightarrow \pi^*$ transitions from the HOMOs to the LUMOs.

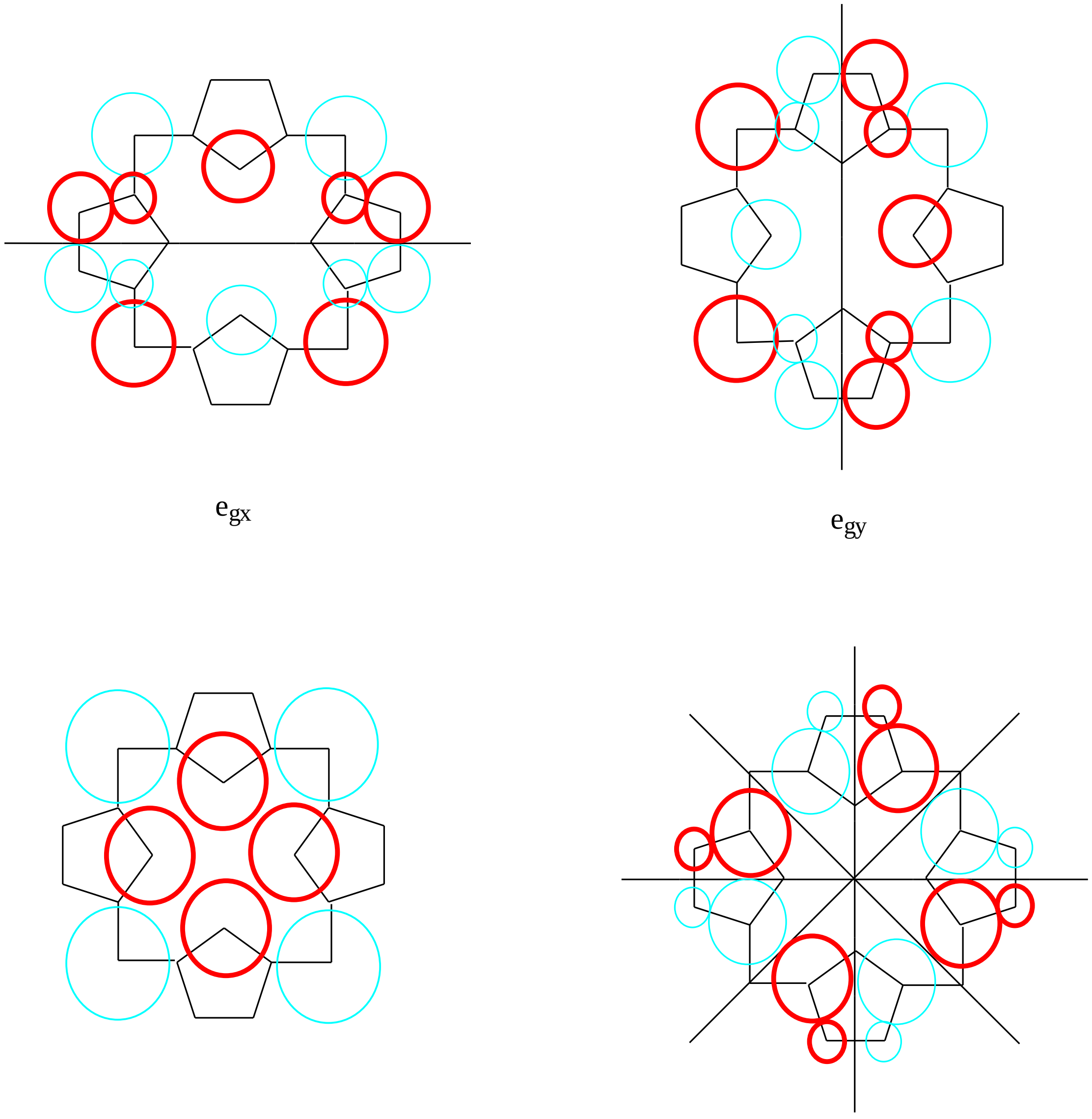

e_{gx} e_{gy}

a_{2u} a_{1u}

Figure 2.2 Porphyrin Orbitals used in the Four-Orbital Model: HOMOs (a_{1u} and a_{2u}) and LUMOs ($e_{g,x}$ and $e_{g,y}$).[12] Circle sizes are roughly proportional to the orbital coefficients, and color (red or cyan) indicates sign. Symmetry nodes are drawn in straight lines.

2.1.2 Resonance Raman (RR) Spectroscopy

Raman spectroscopy, like infrared (IR) spectroscopy, is a probe of the vibrations of molecules, but the two methods can “see’ different transitions: IR spectroscopy relies on vibrations causing a net change in dipole moment, and Raman on changes in the polarizability. Whereas IR spectroscopy directly measures the photon energy absorbed to excite molecular bond vibrations, Raman spectroscopy measures the excitation of bond vibrations in an indirect manner, utilizing the phenomenon of scattering. When molecules absorb photons, they are first excited to a virtual energy state, then scatter light in all directions as they relax. A molecule may relax back elastically to the same vibrational state it started in, such that the reemitted photon has the same energy as the absorbed photon (Rayleigh scattering); alternatively, it may relax inelastically to a vibrational state of either higher or lower energy so that the emitted photon will be correspondingly lower (Stokes scattering) or higher (anti-Stokes) energy, respectively. The Raman spectrum is generated by plotting the intensity of the inelastically reemitted light versus the energy difference (generally in wavenumber) between the scattered and incoming light.

In Resonance Raman spectroscopy, the frequency of the incoming light (laser beam) is chosen to be near an electronic transition (resonance) in the target molecule so that it is excited to one of its excited electronic states rather than to a virtual energy state. The vibrational modes associated with that particular transition thus exhibit a greatly increased scattering intensity, overwhelming Raman signals from other transitions. For instance, resonance with a π-π* transition (such as the Soret or Q bands of porphyrins) enhances stretching modes of the π-bonds involved with the transition. Resonance Raman spectroscopy has proved to be one of the best probes of the conformation of porphyrins.[15,16]

In order to assign the peaks in the porphyrin RR spectra to molecular vibrations, they are compared to the nickel octaethylporphyrin (NiOEP) standard; the assignments for NiOEP can be found in literature references.[15,17,18] The frequencies of several of these peaks have been found to correlate with core size and spin state, as well as oxidation state. These correlations serve to provide useful structural information, and we are most interested here in nonplanar distortions. Besides being affected by the choice of central metal and its spin state, core size (defined as the length of the projection of the metal-nitrogen bond into the average plane of the heavy atoms of the porphyrin macrocycle) can also be affected by the nonplanar distortion of the macrocycle. It was noted by Hoard[19] that the porphyrin core size decreases as the degree of nonplanarity increases, and this trend was verified by Shelnutt et al.,[20] who found that the relationships between Raman frequencies and core size are very different for series of porphyrins with increasing nonplanarity from those observed for planar porphyrins: Raman frequencies (such as ν_2, ν_3, and ν_4) show positive correlation versus core size in the non-planar series but negative slopes for planar porphyrins. Also of interest here are correlations to spin state, which will be used in Chapter 4 to detect binding of axial ligands.

2.2 Molecular Mechanics

Molecular mechanics (MM) is a computational method to find optimum geometric configurations (and their associated energies) of molecular systems by minimizing along a potential energy surface determined by a *force field*. Force field based simulation is a way of modeling inter-atomic interactions using empirically derived equations whose mathematical form is familiar from classical mechanics; for example, a bond stretch can be represented simply as two weights connected by a spring. Although a complete treatment of molecular systems would require invoking quantum mechanics, it is computationally expedient to treat atomic nuclei as classically interacting particles with empirical models embodying the electronic behavior.

A force field is comprised of the functional form of the *potential energy expression* and the parameters needed to fit the expression for the *atom types* contained in the model. Besides the element, the *atom type* takes into account its chemical environment, such as hybridization or oxidation state. The *energy expression* is a summation over the pertinent valence (or bonded) interactions and non-bonded (both inter- and intra-molecular) interactions. Valence interactions include bond stretches, bond angles, torsion angles, and inversions; non-bonded interactions include van der Waals, electrostatics, and hydrogen bonding. The energy expression can thus be written:

$$E = E_{valence} + E_{nonbond}$$

$$E = (E_{bond} + E_{angle} + E_{torsion} + E_{inversion}) + (E_{vdW} + E_{electro} + E_{H-bond})$$

As the energy expression is applied to a particular molecular system, the force field must contain parameters for all the types of atoms present and pertinent combinations thereof. Since the force field (both functional form and parameters) will determine the quality of the simulation, it must be of suitable quality and applicability to the model at hand in order to obtain good results. The custom force field used in this dissertation is a modification of the Dreiding II force field,[21] an all-purpose force field covering organic, biological, and main-group inorganic molecules. The Dreiding II force field allows for mixed usage of different functional forms for different combinations of atoms types. Generally, it uses harmonic bond stretch and bond angle terms, a cosine-Fourier expansion torsion term, and an umbrella functional form for inversions. On the non-bonded side, van der Waals interactions and hydrogen bonding are described by the Lennard-Jones potentials, and electrostatic interactions between atomic monopoles are described by a Coulombic term with (distance-dependent) screening using a dielectric constant in lieu of explicit solvent.[21]

Building upon Dreiding II, a custom force field for porphyrins was developed by Shelnutt et. al.[22] In the Shelnutt force field, custom atom types are defined for the porphyrinic core nitrogens and for the three distinct carbon atom positions: α, β, and *meso*. Coordination to a core metal is facilitated using a four-periodic function. For the peripheral substituents, standard DREIDING II force field parameters are used. This force field has been shown to accurately reproduce the crystal structures of both planar and nonplanar metalloporphyrins.[23-25]

In addition to structure prediction, the potential energy surface allows us to calculate the energy “penalty” for deviating for the equilibrium geometry, so that energetic barriers and transitions states may be obtained. One feature of force-field based simulations that is very useful for studies of structure-function relationships is the ease of adding constraints and/or restraints to the potential. *Constraints* (which can also be applied in quantum-based calculations) are absolute conditions, such as fixing certain atoms to desired positions and not allowing them to move. *Restraints* are extra terms added to the energy expression to bias or force the system in certain ways; for example, adding an extra torsion potential to a particular bond to bias the torsion angle toward a desired value.

2.3 Molecular Dynamics

Molecular dynamics is a simulation technique that considers the evolution of a molecular system with time, in contrast to molecular mechanics which focuses on finding particular geometries and their associated energies or other static properties. Like molecular mechanics, molecular dynamics is a force field based simulation method. Forces on each atom are obtained by calculating the spatial derivative of the potential energy given by the force field. Whereas molecular mechanics calculates the forces on the atoms and changes the atomic positions such as to minimize the interaction energies, molecular dynamics moves the atoms in response to the calculated forces according to Newtonian mechanics.

$$\boldsymbol{F}_i(t) = m_i\ \mathbf{a}_i(t)$$

$$-\frac{\partial V}{\partial \mathbf{r}_i} = m_i\ \frac{\partial^2 \mathbf{r}_i}{\partial t^2}$$

where $\boldsymbol{F}_i$, m_i, $\mathbf{a}_i$, and $\mathbf{r}_i$ are the force, mass, acceleration, and coordinates, respectively, of atom i; t is time; and V is potential energy. The Verlet routine,[26] which employs finite difference methods for numerically integrating the equations of motion, is commonly used in molecular dynamics to propel the system. Initial atomic coordinates are given as input (sometimes determined wholly or partly from a molecular mechanics energy minimization). Initial velocities are randomly generated at the beginning of a dynamics run, and scaled according to the desired simulation temperature. The Verlet velocity algorithm updates the positions ($\boldsymbol{r}$) and velocities ($\boldsymbol{v}$) after a time step Δt as follows:

$$\boldsymbol{r}(t+\Delta t) = \boldsymbol{r}(t+\Delta t) + \boldsymbol{v}(t)\,\Delta t + \frac{1}{2}\,\boldsymbol{a}(t)\,\Delta t^2$$

$$\boldsymbol{a}(t+\Delta t) = \frac{\boldsymbol{F}(t+\Delta t)}{m}$$

$$\boldsymbol{v}(t+\Delta t) = v(t) + \boldsymbol{v}(t)\,\Delta t + \frac{1}{2}\Delta t\,[\,\boldsymbol{a}(t) + \boldsymbol{a}(t+\Delta t)\,]$$

The coordinates (and velocities) obtained from a complete dynamics run are referred to as the *trajectory*. Although smaller time steps will lead to larger computational workloads, it is important that the time step be sufficiently small to account for the fastest vibrations in the system.

2.4 ZINDO/S

The classical simulation techniques discussed above (molecular mechanics and molecular dynamics) are highly efficacious for examining the geometries, (nuclear) motions, and relative conformational energies of molecular systems, requiring far less computer resources than quantum computational methods while providing a sufficiently high level of accuracy for many tasks. These classical methods cannot, however, simulate quantum electronic effects-- as the optical properties of porphyrins are of great interest, simulation of their absorption spectra is particularly desired here.

Various quantum mechanical computational techniques are capable of simulating absorption spectra. The principal drawback to “high level” ab initio or density functional theory (DFT) work is the enormous computational workload, with the desired optical characterizations requiring even more advanced techniques (e.g. time-dependent DFT) than basic geometry calculations. The computational workload can be greatly reduced by using mathematical approximations known as semi-empirical techniques, so called as they employ experimentally-obtained parameters to replace some difficult integrals that appear in truly first principles application of quantum mechanics.

In this dissertation, a technique is used known as ZINDO/s,[27] belonging to a class of semi-empirical methods (INDO, or Intermediate Neglect of Differential Overlap) that neglect certain differential overlap terms in the Schrödinger equation. ZINDO/s is specifically parameterized for spectroscopy, making it ideal for our purposes as we are using classical methods first to rapidly and efficiently obtain molecular geometries and only using the quantum computation to simulate optical spectra.

Obtaining the absorption spectra generally requires calculating the ground state wavefunction, then performing calculations to mix some of the virtual (unoccupied) orbitals into the ground state (occupied) orbitals while holding the geometry constant; this is called the configuration interaction method. Frequencies of spectral transitions are obtained from the difference between the ground state and various excited states according to $\nu = \Delta E/h$, where h is Planck’s constant.

CHAPTER 3: TUNING THE OPTICAL PROPERTIES OF PORPHYRINS WITH NON-PLANAR DEFORMATIONS

3.1 Introduction

Among the most studied aspects of porphyrins have been their fascinating optical properties. These chromophores have been termed the "colors of life"[4] as it is heme (an iron-containing porphyrin) that gives blood its red color and chlorophyll (magnesium-containing reduced porphyrin) that puts the green in plants. Having been used as pigments and dyes for centuries, porphyrins are today among the best candidates as photosensitizers for many advanced optical applications. Porphyrins could be incorporated as the photosensitive elements in photoresponsive systems in which optical signals are captured and converted to new physicochemical output functions (e.g. mechanical/ electrical); such systems could be used in a number of applications, such as phototriggered targeted drug delivery systems, photocontrolled enzymatic bioprocessing, and photocontrolled separation/recovery systems.[28] Porphyrins have been widely applied in photo-dynamic therapy for treatment of cancer tumors and, together with their excellent light-absorbing properties, their favorable redox potentials make porphyrins excellent candidates for photocatalysts.[29] In the near future, nanomaterials that absorb and/or emit light will be key components of optical and photonic devices.[30] Porphyrins can be controlledly assimilated into a wide variety of nanostructures;[31] as such, they will likely find new applications in non-linear optical materials, as parts of electrochromic displays, and for solar energy conversion.[29]

All these application require fine-tuning of the optical properties of the chromophores. In addition to tweaks in optical properties arising from the electronic effects of substituents at the periphery and the core, non-planarity of the porphyrin macrocycle is expected to play a role. Several spectral signatures of the porphyrin macrocycle have been shown to be significantly affected by substituent-induced nonplanar deformations, including those detected by resonance Raman, 1H NMR, and UV-visible spectroscopies.[10,32,33] Indeed, macrocycle distortion affects almost all photophysical parameters, including fluorescence yields, Stokes shifts, and lifetimes of excited state.[2] Delineating the relationship between the porphyrins' absorption bands and their non-planarity would allow development of design principle for chromophores or receptors of desired optical properties for specific applications. It is possible to tailor macrocycle conformations to achieve designed properties, as synthetic methods to prepare highly substituted porphyrins (including unsymmetrical substitutions) have seen great progress.[2] Establishment of a connection between optical characteristics and nonplanar deformations of the porphyrin macrocycle would also be useful for spectroscopically probing the structures of hemes (iron porphyrins), chlorophylls and related photosynthetic pigments, and other tetrapyrrole cofactors in proteins. Unlike structure determination via x-ray diffraction, which requires crystallization of the analyte, spectra can be used for determination of nonplanarity in solution, important to determining structure function relations.

This chapter will examine the effects of non-planar distortions on the optical spectra of nonplanar porphyrins, in particular the origin of the spectral red shifts seen for peripherally crowded nonplanar porphyrins. This is a topic that has generated considerable debate in the literature.[34-37]

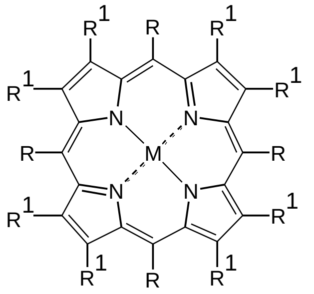

1 R = C_6H_5, $R^1 = CH_2CH_3$
2 R = $R^1 = C_6H_5$
3 R = C_6H_5, R^1 = Br
4 R = NO_2, $R^1 = CH_2CH_3$
5 R = $C(CH_3)_3$, R^1 = H
6 R = H, $R^1 = CH_2CH_3$
7 R = C_6H_5, R^1 = H
8 R = $(CF_2)_2CF_3$, R^1 = H
9 R = R^1 = H
10 R = CH_3, R^1 = H
11 R = CF_3, R^1 = H
17 R = CH_2CH_3, R^1 = H
18 R = $CH(CH_3)_2$, R^1 = H

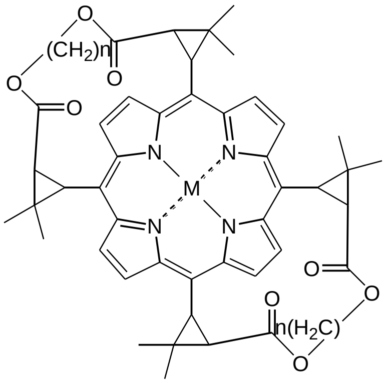

12 n = 8 (a), 9 (b), 10 (c), 11 (d), 12 (e), 14 (f), 16 (g)

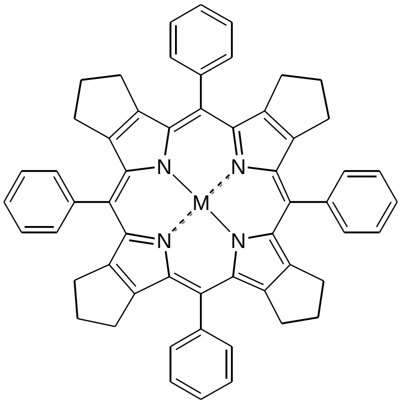

14 n = 1
15 n = 2
16 n = 3

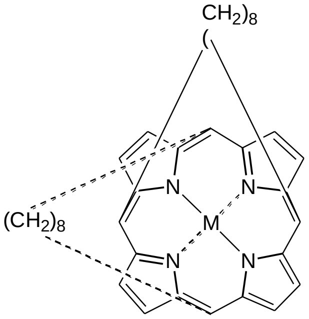

19

Figure 3.1 Structures of Compounds Discussed in Chapter 3

3.2 Background

The first analysis of the relationship between nonplanarity and red shifts in the optical spectra of peripherally crowded nonplanar porphyrins was in a study in which the optical spectrum of zinc octaethyltetraphenylporphyrin [ZnOETPP, **1** (M = Zn)][38] showed a large red shift compared to zinc octaethylporphyrin [ZnOEP, **6** (M = Zn)] or zinc tetraphenylporphyrin [ZnTPP, **7** (M = Zn)]. Semi-empirical (INDO/S) calculations indicated that this resulted from a greater destabilization of the highest occupied molecular orbital (HOMO) than of the lowest unoccupied molecular orbital (LUMO) in ZnOETPP compared to ZnOEP and ZnTPP. Consistent with this interpretation, ZnOETPP was easier to oxidize than ZnOEP or ZnTPP, but the first reduction potential did not change as significantly, confirming a narrowing of the HOMO-LUMO separation.

Additional experimental data and semi-empirical (INDO/S) calculations for a wide range of peripherally crowded nickel porphyrins including NiOETPP (1, M = Ni)[24] and NiT(tBu)P (5, M = Ni)[25] reinforced this view. While it has been noted that the observed red shifts depend both on the substituents present on the porphyrin ring and on the amount and type of substituent-induced nonplanar deformation[39], it had become generally accepted that a large red shift in the UV-visible bands is indicative of a very nonplanar porphyrin macrocycle.[10,32,33] However, doubt was cast on this notion by some workers in the field.

In the first of several recent papers concerning the red-shift/ nonplanarity connection, DiMagno[34] reported that cobalt-(II) tetrakis(heptafluoropropyl)porphyrin

[$CoT(C_3F_7)P$, **8** (M = CoII)] was very saddle distorted, as demonstrated by X-ray crystallography, but apparently did not show a red shift in solution or in the solid-state. Theoretical (AM1) calculations were reported which showed that constraining porphine [H_2P, **9** (M = 2H)] to a saddled geometry actually produced a blue shift for the Q(0,0) band, the lowest energy π-π^* transition. Based on these findings, it was suggested that the red shifts previously seen in nonplanar porphyrins were the result of different substituent effects in planar versus sterically crowded nonplanar porphyrins and, more specifically, the overlap of the aryl substituents in porphyrins **1**-**3** with the π-system of the porphyrin macrocycle.

The DiMagno paper was subsequently rebutted in a density functional theory (DFT) study of *ruffled* and *saddled* zinc porphyrins by Ghosh,[35] who calculated red shifts for both types of deformation. This latter finding was in agreement with the prevailing view that nonplanar distortions cause the large red shifts seen in the optical spectra of porphyrins.[10,32,33] Notably, the porphyrin macrocycle structure used in Ghosh's 2000 paper came from energy-optimized structures generated with the un-truncated macrocycle substituents, i.e., the whole substituent group.

Another paper by DiMagno[36] then used DFT to examine structural and electronic contributions to the electronic spectra of porphine [H_2P, **9** (M = 2H)], tetramethylporphyrin [$H_2T(Me)P$, **10** (M = 2H)], and tetrakis(trifluoromethyl)porphyrin [$H_2T(CF_3)P$, **11** (M = 2H)]. In this study, the contribution arising from nonplanarity was estimated by artificially constraining the porphyrin into progressively more ruffled conformations. It was again concluded that nonplanarity (in this case ruffling) had a negligible effect on the electronic spectrum, and the major contributor to the red shift was now proposed to be in-plane nuclear reorganization (IPNR). IPNR was defined as changes in the porphyrin bond lengths and bond angles induced by interactions between the substituent and the porphyrin macrocycle. Most recently, another paper was published by Ghosh[37] confirming that neither artificially ruffling nor artificially saddling the porphyrin produces a large red shift. Based on these findings, it was concluded[37] that IPNR rather than nonplanarity was indeed the dominant effect.

The fact that a porphyrin can apparently be deformed into a very nonplanar structure but not show a large red shift is startling and potentially draws into question the origin of the red shifts in highly substituted nonplanar porphyrins. However, assessment of the importance of IPNR using the published work[36,37] was confounded by the lack of specific information about which substituent-induced changes in bond lengths and/ or bond angles might produce the supposed IPNR red shift. It thus seemed that while an important question might have been raised about the origin of the red shift, the IPNR explanation for the missing red shift had not been adequately verified. We therefore decided to investigate the effect of structural perturbations on the electronic transitions of porphyrins in more detail, with the goals of understanding why the observed red shifts could not be reproduced by the constrained porphyrin structures and determining their true origin.

3.3 Experimental

3.3.1 Molecular Mechanics (MM), Molecular Dynamics (MD), and INDO/S Calculations; and Normal-Coordinate Structural Decomposition (NSD).

Molecular mechanics (MM) calculations using Cerius2 version 4.6 software (Accelrys Inc., San Diego) were carried out on a Silicon Graphics Octane workstation. The force field used in the calculations is based on DREIDING II,[40] modified to include force constants and equilibrium values for bonds, angles, torsions, and improper torsions as well as parameters describing the van der Waals and electrostatic interactions for the atoms of the porphyrin macrocycle,[22] and including the most recent revisions of these parameters.[41]

Energy-optimized structures of the tetraalkylporphyrins with and without various constraints and fixed atoms were generated. The electronic energy levels and absorption spectra of the resulting MM structures were obtained via INDO/s calculations performed using Hyperchem software version 7.0 (HyperCube Inc., Gainesville, FL) after altering the nickel β_d parameter as described in Jentzen et al.[25] The degree of nonplanar deformation was analyzed in terms of the magnitudes of the normal-coordinate deformations using our NSD program.[7,8]

In the case of the bridled chiroporphyrins (**12a-g**), determining energy-optimized structures is confounded by the multitude of configurations the long, flexible straps can adopt. For those molecules, rather than taking a single structure from a molecular mechanics minimization, an average was obtained from molecular dynamics (MD) trajectories simulated using the same software and force field as the MM calculations. Trajectories were obtained for 2-ns intervals at a fixed temperature of 300 K. Previous to running the dynamics calculations, the chiroporphyrin structures were built and equilibrated by running at least 100 ps of dynamics at an elevated temperature of 900 K (500 ps at 600 K for the eight- and nine-carbon strap chiroporphyrins). Snapshot structures extracted from the 2-ns MD trajectories at 0.10- or 0.05-ps intervals were then analyzed by NSD. The individual deformations for all 20,000 (or 40,000) snapshot structures from each trajectory were then averaged to determine the average degree of nonplanar deformation. NSD analysis of the MD snapshot structures was done with a version of the NSD program modified to provide automation for processing multiple related structures. To further sample configuration space, six independent 2-ns dynamics trajectories starting from different initial structures and velocities, obtained by additional MD simulations at elevated temperatures followed by cooling to 300 K. These time-averaged deformations give a measure of the distortion under solution conditions by averaging over the many conformations of the flexible portions of the chiroporphyrins, and the values reported are averages over the six trajectories.

3.3.2 UV-Visible Absorption Spectroscopy.

UV-visible spectra of bridled chiroporphyrin complexes **12a-g** (M = Ni, 2H) were measured on approximately 2 μM CS_2 or CH_2Cl_2 solutions in a 1-cm quartz cell with either a Perkin-Elmer Lambda 9 or a Hewlett-Packard HP9852A spectrophotometer. The spectrometer resolution is approximately 2 nm. Curve fitting indicates the presence of at least two structural forms or two electronic transitions making up the Soret band. To get a single value for the peak wavelength of the Soret band, a second-order polynomial is fit to the five points near the maximum and interpolated to get the λ_{max} values reported.

3.3.3 Resonance Raman Spectroscopy.

Raman spectra were obtained from the porphyrins **12a-g** (M = Ni) in CS_2 or CH_2Cl_2 (2-100 μM) in 3 x 3 x 30 mm quartz cells at room temperature. The spectra were excited by using the 406.7-nm line of a model 304 Kr+ laser (Coherent Inc.). Spectra were detected with a 0.75-m monochromator with a CCD detector system (JY Inc., Edison, NJ) described in Franco *et al*.[42] Peak frequencies were obtained by simulation of the spectra using Lorentzian line shapes and the program PeakFit (SPSS, Inc., Chicago, IL).

3.4 Survey of the UV-Visible Spectral Bands of Peripherally Crowded and Peripherally Uncrowded Porphyrins.

Seeking to build on previous anecdotal evidence of redshifts in absorption spectra associated with porphyrin nonplanar distortions, UV-visible spectral and X-ray structural data for free base and nickel porphyrins with various substituents resulting in a wide range of nonplanarity is compiled in Table A-1 to Table A-4 of Appendix A, summarized in Table 3.1, and plotted in Figure 3.2. The tables give the wavelengths of the Soret bands, the Q(0,0) bands, the total out-of-plane deformations d_{total} (calculated from the crystal structures using NSD), and $\Sigma\sigma_p$ (an estimate measure of the electron withdrawing or donating ability of the substituents, obtained by summing the Hammett constant σ_p for each substituent[43]).

Table 3.1 Absorption Maxima (λ_{max}, nm) in CH_2Cl_2 and Out-of-plane Deformations (d_{total}, Å) for Sterically Crowded (Highly Nonplanar) Porphyrins and Sterically Uncrowded (Planar to Moderately Nonplanar) Porphyrins.[a]

Group	M	$B_{(0,0)}$	$Q_{X(0,0)}$	d_{total}[b]	$\Sigma\sigma_p$[c]
Planar & Moderately Nonplanar	2H	377-420	613-659	0.046-1.207	-2.16, +1.08
Highly Nonplanar	2H	426-472	666-743	1.915-3.901	-1.24, +2.92
Planar & Moderately Nonplanar	Ni	385-425	536-586	0.087-2.238	-1.80, +0.00
Highly Nonplanar	Ni	416-459	579-690	2.287-4.003	-1.80, +4.00

---

[a] Details of the structures used to prepare this table are provided in Appendix Table A-1 to Table A-4.

[b] Total out-of-plane distortion from NSD.

[c] $\Sigma\sigma_p$ was calculated by summing σ_p values for the substituents.[43]

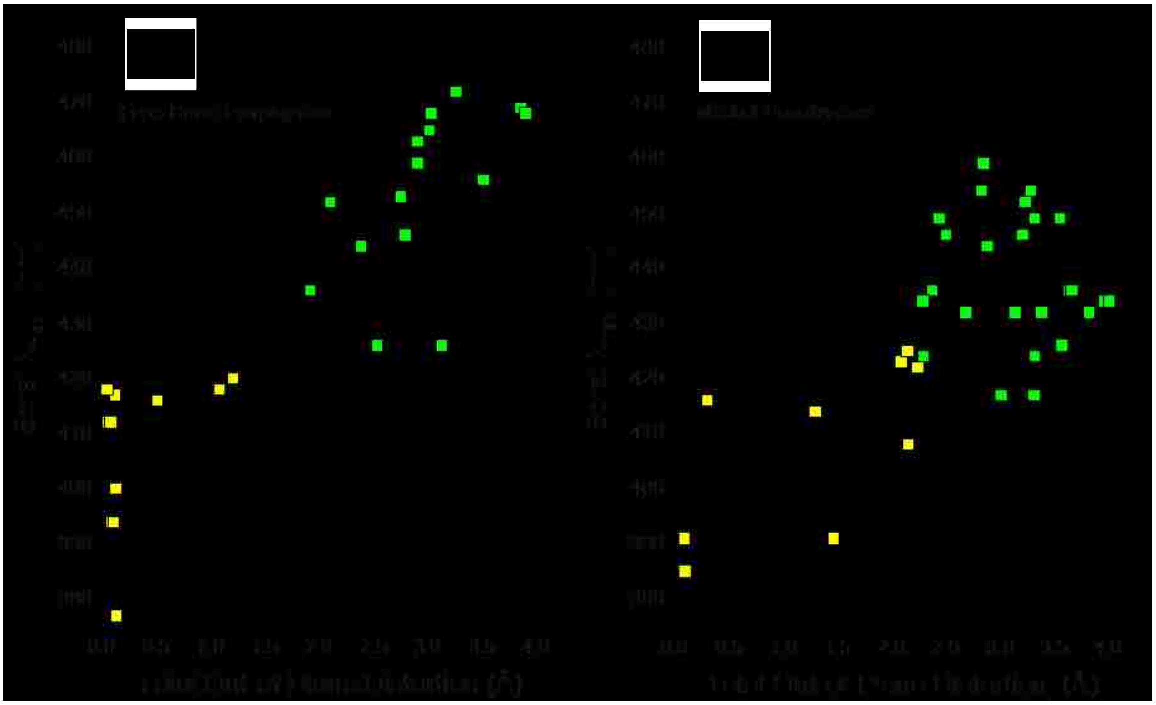

[redacted]

In Figure 3.2, the planar to moderately nonplanar compounds (d_{total} < ~2 Å, shown in yellow) are mostly porphyrins with fewer, non-bulky peripheral substituents such as OEP (**17**) and TPP (**7**), although some dodecasubstituted porphyrins, such as porphyrin **14**, are also included in this group as their substituents are known not to cause large nonplanar deformations.[22,44,45] The group of highly sterically crowded porphyrins, in contrast, exhibit large total distortions (d_{total} > ~2 Å, shown in green) and have strongly red-shifted absorption bands relative to the group of more planar porphyrins.

There is considerable scatter evident in the wavelengths of the absorption maxima (typically about 40 nm) for the B(0,0) (Soret) band within both the planar to moderately nonplanar porphyrins and the highly nonplanar porphyrins. This large range of absorption maxima within a group is likely related to several factors, including the electron donating/withdrawing effect of the substituents, the number of substituents, and the amount and type of nonplanar deformation. However, there is little overlap of the absorption maxima for the two groups of porphyrins, indicating a strong red shift for the peripherally crowded and highly nonplanar porphyrins. In other words, this red shift appears to be large enough that it is not obscured either by variation of the type and number of substituents or by core substituent (M = 2H or Ni).

That the red shifts are a consequence of nonplanarity and not the bulky substituents themselves is supported by studies of less sterically crowded NiOEP, for which both planar and nonplanar structures have been detected in solution and in the crystalline state.[46-48] In the crystalline state, the triclinic forms of NiOEP show essentially planar macrocycles (d_{total} ~ 0.1 Å), whereas the tetragonal form is ruffled (d_{total}

~ 1.5 Å). In solution, NiOEP exists as a mixture of planar and nonplanar forms with the nonplanar form exhibiting red-shifted absorption bands.

A similar phenomenon has been noted for NiT(Me)P. The crystal structure of NiT(Me)P has been reported[49-51] and is virtually planar (d_{total} ~ 0.3 Å), in contrast with the calculated structure that is considerably nonplanar (d_{total} ~ 1.9 Å). In agreement with the calculated structure, resonance Raman spectroscopic studies suggest that NiT(Me)P is nonplanar in solution.[25] This discrepancy is probably explained by crystal packing forces overcoming the shallow energy well favoring ruffling of NiT(Me)P.

3.5 Absorption Spectra in a Series with Controlled Substituent Electronic Effects

The presence of a large red shift for peripherally crowded nonplanar porphyrins is also confirmed by studies that used a series of porphyrins where the electronic effect of the substituents is more carefully controlled. In one case, the mostly *saddle* non-planar distortion varies with the size of rings fused to the pyrrole position of dodecasubstituted porphyrins (**14-16**).[22,44,45] In another case, the mostly *ruffle* distortion varies with the bulkiness of alkyl substituents at the meso positions (**10, 17, 18, and 5**).[25] The UV-visible data for these series are summarized in Table 3.2, and data for the ruffled series are plotted in Figure 3.3A. Progressively larger red shifts occur with increasing steric crowding of the substituents for both classes of porphyrin. The association of redshifts to nonplanarity is more clearly seen for these series of porphyrins because the number and nature of the substituents and the type of distortion (e.g., saddle versus ruffle, as determined crystallographically and/or by molecular modeling studies) is constant within each series. The trends for the ruffled and saddled series are similar even though the numbers and types of substituent and the types of deformation are markedly different for the two series.

Table 3.2 Absorption Maxima (λ_{max}, nm in CH_2Cl_2) for Porphyrins with Controlled Substituent Electronic Effects but Varying Degrees of Peripheral Steric Crowding and Macrocycle Nonplanarity.

Porphyrin	Free Base		Nickel		Ref.
	$B_{(0,0)}$	$Q_{X(0,0)}$	$B_{(0,0)}$	$Q_{X(0,0)}$	
14	414	634	408	554	45
15	438	678	424	579	45
16	464	704	440	595	45
10 (T(Me)P)	420	658	416	n/o	49-52
17 (T(Et)P)	412	656	416	n/o	49-52
18 (T(iPr)P)	420	658	423	586	53
5 (T(tBu)P)	446	691	453	629	53

3.6 MM and INDO/S Calculations for Tetraalkylporphyrin Series

The data presented in Sections 3.4 & 3.5 above provide clear experimental evidence for a very large red shift arising from steric crowding of the peripheral substituents. The important question though is whether this red shift is a consequence of the out-of-plane deformations that accompany peripheral steric crowding, as had generally been accepted,[10,32,33] or whether they are the result of some other effect such as IPNR.[36,37]

To answer this question, we began by calculating energy-minimized MM structures for porphine and several tetraalkylporphyrins containing Ni or Zn at their core. Using these MM structures, we then calculated π-π^* electronic transition energies (gap between ground and excited states, corresponding to wavelength of absorbed light) via the INDO/S semi-empirical method. Table 3.3 summarizes the ruffling dihedral angles and wavelengths of the UV-visible bands that are calculated using the MM/INDO procedure for the nickel and zinc tetraalkylporphyrins and compares the calculated transition wavelengths with the experimentally observed spectral data.

Table 3.3 Absorption Maxima for Nickel & Zinc Tetraalkylporphyrins, Experimentally Observed (in CH_2Cl_2) and Calculated by INDO/S using MM structures.

Porphyrin	Ruffling Angle (°)[a]	B(0,0) (nm)		Q(0,0) (nm)	
		Calc.[b]	Obs.[c]	Calc.[b]	Obs.[c]
		NICKEL			
NiP	0	325.4	385	616.3	536
NiT(Me)P	38	354.6	416	674.5	n/o
NiT(Et)P	37	353.4	416	671.1	n/o
NiT(iPr)P	45	364.4	423	697.7	586
NiT(tBu)P	56	395.9	453	784.2	629
		ZINC			
ZnP	0	329.4		628.4	
ZnT(Me)P	19	348.6		668.4	
ZnT(Et)P	18	349.5	419[d]	669.7	593[d]
ZnT(iPr)P	30	360.3	420	700.0	619
ZnT(tBu)P	44	397.1	458	810.9	657

[a] C_α-N-N-C_α (trans) torsion angle in unconstrained minimized structures.
[b] Average of two transitions.
[c] Values taken from literature.[52,53]
[d] For n-butyl derivative.

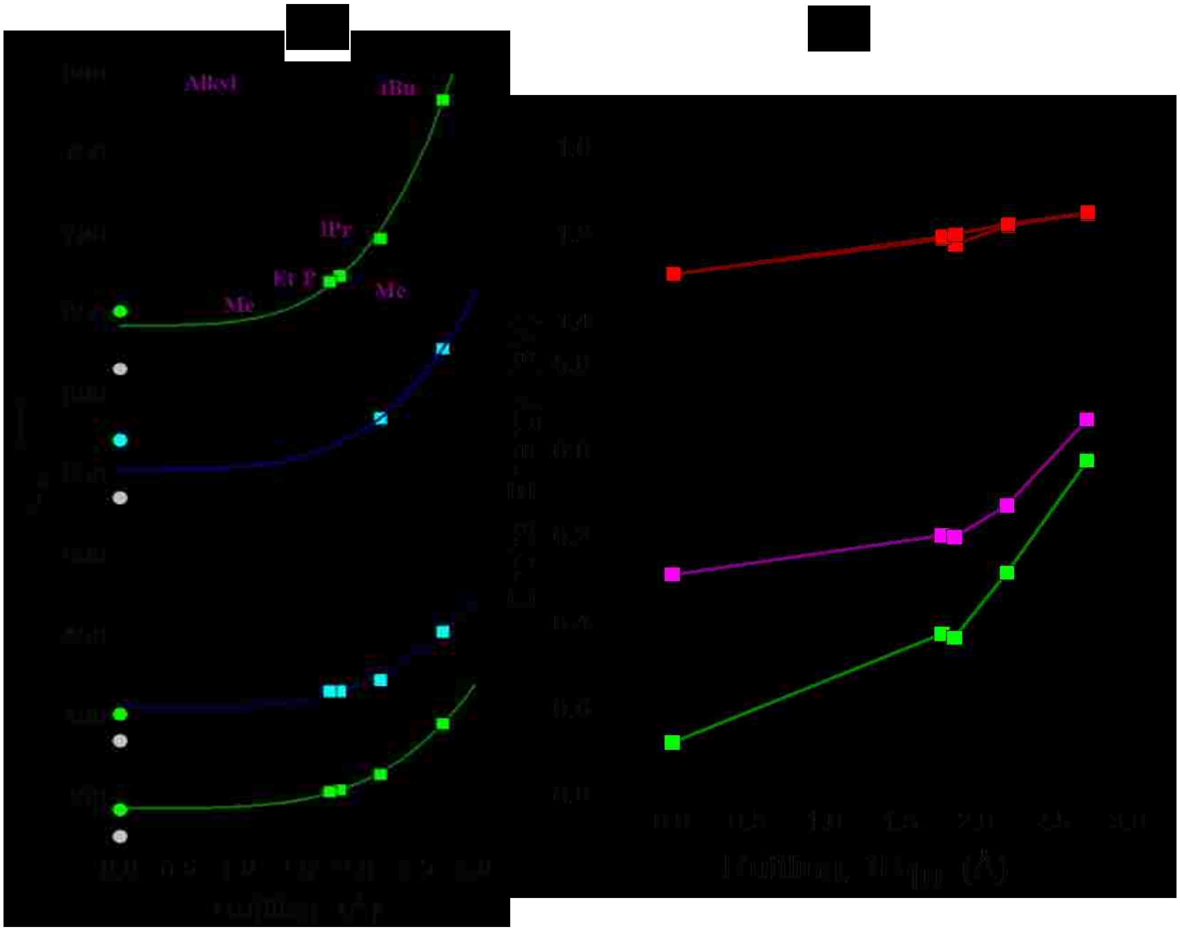

[redacted]

The trends in the UV-visible absorption maxima of the nickel tetraalkylporphyrins with the degree of ruffling are shown in Figure 3.3A. The experimental trends are clearly reproduced by the calculated transition wavelengths. The scatter in Figure 3.3A is less, as would be expected, for this homologous series of porphyrins than that seen in Figure 3.2 for a more varied group of porphyrins. The calculations consistently overestimate the energies of the Soret B(0,0) transitions and underestimate the energies of the Q(0,0) transitions. Further, the INDO calculations predict a red shift of 2942 cm^{-1} for the Soret band of NiT(tBu)P versus NiT(Me)P, which is larger than the experimentally observed red shift of 1963 cm^{-1}. Similar results are obtained for the zinc complexes, with a calculated red shift of 3504 cm^{-1} and an observed red shift of 2032 cm^{-1}.[53] Nevertheless, the agreement is reasonable, validating the MM/INDO methods used for the purposes of the study.

Figure 3.3B shows the relationship between the energies of the frontier molecular orbitals, as calculated by INDO, and the ruffling for the nickel tetraalkyl porphyrins. The highest occupied molecular orbitals (HOMOs), the a_{1u} and a_{2u} orbitals, are destabilized with increased ruffling as the macrocycle bonds are twisted, especially the a_{2u} orbital. On the other hand, the energy of the lowest unoccupied molecular orbitals (LUMOs), the two (degenerate) e_g orbitals, remains relatively constant. As the Soret (and Q) bands arise from transitions between these orbitals, it is the narrowing of the HOMO-LUMO energy gap that leads to absorption of higher wavelength light and causes the red shifts in the spectrum.

3.7 Possible Origins of the Large Red Shifts in the UV-Visible Bands of Sterically Crowded Porphyrins.

Of the tetra-alkyl series above, the extremes of MT(Me)P and MT(tBu)P (M = Ni or Zn) were chosen for more detailed studies of the factors causing the red shift. These two tetraalkylporphyrins are particularly good choices because while the substituents are expected to have similar electronic effects, the red shifts in the absorption spectra are very large, facilitating the examination of the effects on structure and minimizing the effect of computational errors. Also, there are fewer local minima for different substituent orientations than would be the case for less symmetric ethyl or isopropyl substituents. Furthermore, the force field used in the study was originally parameterized for porphyrins with a nickel core and alkyl substituents, hence it should give optimal predictions for related structures. Complementary calculations with a core of zinc, which is larger and produces a very different energetic/conformational landscape, provide assurance that the conclusions obtained are not specific to nickel.

For the energy minimized structures of MT(tBu)P and MT(Me)P (M = Ni or Zn), Table 3.4 (entries 1A and 1B) lists the calculated peak positions of the B(0,0) Soret band and the C_α-N-N-C_α dihedral angle, which geometrically most plainly typifies the ruffling of the macrocycle. These energy minimized structures were also analyzed by NSD and Table 3.5 lists the deformations in the ruffling-symmetry B_{1u} modes, as well as the total out-of-plane deformations. (The corresponding totally symmetric in-plane deformations are provided in Table A-5 for Ni and Table A-6 for Zn.) Smaller out-of-plane deformations are observed for Zn than for Ni, consistent with the metal-size dependence.[23,24] As expected, T(tBu)P is much more nonplanar than T(Me)P as a result of the greater steric bulk of the tert-butyl substituents (e.g., d_{total} = 2.75 Å in NiT(tBu)P versus 1.87 Å in NiT(Me)P). For both porphyrins, essentially all of the calculated out-of-plane distortion (d_{total}) is localized in the B_{1u} ruffling-symmetry modes (B_{1u} total) and mainly in the first-order (lowest frequency) B_{1u} deformation ($1B_{1u}$) that is commonly referred to as ruffling. However, the second-order $2B_{1u}$ and the third-order $3B_{1u}$ deformations are also significant irrespective of the porphyrin substituents and the central metal. We will return to the significance of these important higher order deformations in the following discussion.

The origins of the large red shifts of the UV-visible bands of MT(tBu)P versus MT(Me)P (M = Ni or Zn) were investigated in detail. The following discussion relates principally to the Soret band of the nickel complex, although similar results are obtained for the corresponding zinc complexes (Table 3.4 and Table 3.5) and for the Q-bands of both metal complexes (e.g., Table 3.3). As noted above, the calculated red shift for NiT(tBu)P versus NiT(Me)P is 2942 cm^{-1}.

Table 3.4 Absorption Soret Bands and Select Structural Parameters for Nickel and Zinc Tetraalkylporphyrins Calculated by Molecular Mechanics & INDO/S.

Entry	Compound	Description of structure	Ruf angle[a] (°)	B(0,0)[b] (nm)	δ^c (°)
		NICKEL			
1A	NiT(Me)P	unconstrained energy minimization	38	354.6	3.0
1B	NiT(tBu)P	unconstrained energy minimization	56	395.9	0.6
2	NiT(Me)P	methyl on tBu vector of NiT(tBu)P	56[d]	391.2	0.6
3A	NiT(Me)P	constrained ruffled and energy minimized	56[d]	361.0	4.6
3B	NiT(Me)P	constrained ruffled and energy minimized	60[d]	363.3	5.5
4A	NiT(Me)P	with constrained NiT(tBu)P bond lengths	60[d]	363.4	5.3
4B	NiT(Me)P	with bond lengths & C_α-C_m-C_α angles of NiT(tBu)P	60[d]	362.8	6.1
4C	NiT(Me)P	constrained planar and minimized	0[d]	341.9	0.2
4D	NiT(tBu)P	constrained planar and minimized	0[d]	336.9	0.0
5	NiT(Me)P	methyls constrained to C_α-C_α-C_m plane	56[d]	362.6	0.0
6A	NiT(Me)P	ruffled by steric interactions at methyl groups	60	380.8	6.4
6B	**19** (M= Ni)	ruffled due to 8-carbon straps	56	391.9	4.8
7A	NiT(Me)P	constrained ruffled, N-C_α-C_m-C_α torsion constrained to value of energy minimized NiT(tBu)P	56[d]	380.4	9.5
7B	NiT(Me)P	as above, corrected for droopy methyls	56[d]	388.0	0.0
		ZINC			
1A	ZnT(Me)P	unconstrained energy minimization	19	348.6	0.8
1B	ZnT(tBu)P	unconstrained energy minimization	44	397.1	1.3
2	ZnT(Me)P	methyl on tBu vector of ZnT(tBu)P	44	391.4	0.0
3A	ZnT(Me)P	constrained ruffled and energy minimized	44	355.9	3.3
5	ZnT(Me)P	methyls constrained to C_α-C_α-C_m plane	44	357.1	0.0
6B	**19** (M= Zn)	ruffled due to 8-carbon straps	46	404.5	8.8
7A	ZnT(Me)P	constrained ruffled, N-C_α-C_m-C_α torsion constrained to value of energy minimized ZnT(tBu)P	44	379.6	8.6
7B	ZnT(Me)P	as above, corrected for droopy methyls	44	387.3	0.0

[a] C_α-N-N-C_α (trans) torsion angle.

[b] Average of two closely spaced transitions.

[c] δ is the bond angle that the meso substituent makes with the C_α-C_α-C_m plane. Negative values indicate that the meso substituent is displaced toward the mean plane of the porphyrin and positive values are away from the mean plane.

[d] Constrained structure optimization.

Table 3.5 Out-of-Plane Total and B_{1u} Deformations of Nickel and Zinc Tetraalkylporphyrin Molecular Mechanics Structures

Entry[a]	Ruffling angle[b] (°)	d_{total} (Å)	B_{1u} (Å) Total	$1B_{1u}$ (Å)	$2B_{1u}$ (Å)	$3B_{1u}$ (Å)
			NICKEL			
1A	38 (min)	1.8650	1.8642	1.8578	0.1397	0.0656
1B	56 (min)	2.7499	2.7499	2.7290	0.3229	0.1012
2	56 (fixed)	2.7499[d]	2.7499	2.7290	0.3229	0.1012
3A	56 (const)	2.5644	2.5643	2.5613	0.1180	0.0374
3B	60 (const)	2.7063	2.7062	2.7037	0.1130	0.0265
4A	60 (const)	2.7179	2.7178	2.7155	0.1068	0.0267
4B	60 (const)	2.7467	2.7466	2.7423	0.1462	0.0429
4C	0 (const)	0.0072	0.0007	0.0006	0.0003	0.0003
4D	0 (const)	0.0016	0.0012	0.0012	0.0001	0.0010
5	56 (const)	2.5644[e]	2.5643	2.5613	0.1180	0.0374
6A	60 (sterics)	2.7704	2.7703	2.7667	0.0916	0.1077
6B	56 (straps)	2.7168	2.7003	2.6884	0.2213	0.1243
7A	56 (tors)	2.7283	2.7282	2.7153	0.2335	0.1261
7B	56 (+Me)	2.7271	2.7270	2.7145	0.2277	0.1282
			ZINC			
1A	19 (min)	0.9703	0.9613	0.9546	0.1052	0.0411
1B	44 (min)	2.2714	2.2714	2.2409	0.3566	0.1030
	X-ray[c]	2.4707	2.3954	2.3903	0.1424	0.0647
2	44 (fixed)	2.2714[d]	2.2714	2.2409	0.3566	0.1030
3A	44 (const)	2.0377	2.0377	2.0352	0.0968	0.0267
5	44 (fixed)	2.0377[e]	2.0377	2.0352	0.0968	0.0267
6B	46 (straps)	2.3792	2.3597	2.3413	0.2509	0.1542
7A	44 (tors.)	2.2705	2.2704	2.2520	0.2505	0.1425
7B	44 (+Me)	2.2702	2.2701	2.2522	0.2444	0.1451

[a] Description of structure as in Table 3.4.
[b] C_{α}-N-N-C_{α} (trans) torsion angle.
[c] Taken from the literature.[54]
[d] Same as entry 1B (core unchanged).
[e] Same as entry 3A (core unchanged).

3.7.1 Substituent Electronic Effects

The difference between the substituent electronic effects for a tert-butyl group compared to a methyl group is expected to be small. This was confirmed by using a structure where the tert-butyl group in the energy-minimized structure of NiT(tBu)P was replaced with a methyl group located along the same (C_m-C_1) vector (see Figure 3.4), and then just the methyl group was energy minimized while constrained to move along and reorient about this vector (The motive for maintaining this bearing is elaborated in Section 3.7.4). This methyl-substituted NiT(tBu)P macrocycle (entry 2 in Table 3.4 and Table 3.5) shows a small blue shift (303 cm^{-1}) compared to energy-minimized NiT(tBu)P as expected. This leaves a large calculated red shift of 2639 cm^{-1} that must be unrelated to a direct electronic effect of the different meso substituents.

3.7.2 Ruffling induced by C_α-N-N-C_α Dihedral Angle Drive

C_α-N-N-C_α dihedral angles across the porphyrin ring were used to constrain the MT(Me)P and MP (M= Ni or Zn) derivatives structures to various degrees of ruffling as defined by these dihedral angles. This is the same constraint that was used in some previous DFT calculations mentioned above[36], and the unsubstituted porphine was included here for comparison. Table 3.6 gives the transition wavelengths for the UV-visible bands calculated by INDO/S for these constrained ruffled structures. Significant red shifts in the absorption bands are predicted as the macrocycle is ruffled both for porphine and tetramethylporphyrin; from the planar structure to the 60° ruffled one, the red shift in the Soret band is 20-22 nm for Ni and slightly less for Zn. However, when one considers that the ruffling dihedral angle for energy-optimized NiT(Me)P is 38° and that for NiT(tBu)P it is 56°, then it is clear that the Soret red shift from this component cannot fully explain the experimentally observed value of 37 nm for NiT(tBu)P versus NiT(Me)P (Table 3.3). In other words, while increasing the ruffling angle from 38° to 56° does produce a small 500-cm^{-1} red shift (as seen by comparing entries 1A and 3A of Table 3.4), it is far less than that required to explain the full calculated or observed red shift between MT(Me)P and MT(tBu)P (M = Ni or Zn). The MM/INDO calculations for these constrained structures therefore agree with the results obtained from DFT calculations[36]; i.e., artificially ruffling the macrocycle does not produce the large experimentally observed UV-visible band red shifts.

Although it seems unlikely that the remaining red shift of 2138 cm^{-1} is related to the small underestimation of the $1B_{1u}$ ruffling for structure 3A compared to energy-minimized NiT(tBu)P (see Table 3.5), we also evaluated this effect by further ruffling the macrocycle using a higher constraint angle of 60° (entry 3B of Table 3.4 and Table 3.5). This increases the amount of ruffling ($1B_{1u}$) deformation to more closely match that seen in the energy-minimized structure of NiT(tBu)P ($1B_{1u} \approx 2.7$ Å) but resulted in only a small incremental red shift of 175 cm^{-1}. Thus, even after accounting for the electronic effect of the tert-butyl group (entry 2) and the $1B_{1u}$ ruffling deformation (entry 3B), there is still a large 1963 cm^{-1} red shift to be explained.

Table 3.6 Calculated Absorption Maxima (Soret and Q bands, nm) for Nickel and Zinc Porphyrins with the Porphyrin Macrocycle Constrained Into Artificially Ruffled Conformations.

Ruffling Angle[a] (°)	Nickel				Zinc			
	NiP		NiT(Me)P		ZnP		ZnT(Me)P	
	B(0,0)	Q(0,0)	B(0,0)	Q(0,0)	B(0,0)	Q(0,0)	B(0,0)	Q(0,0)
0	325.4	616.3	341.9	652.2	329.4	628.4	343.4	655.8
20	327.6	619.8	347.3	663.2	330.9	631.4	348.9	669.3
40	333.9	628.8	355.3	675.3	335.0	638.4	354.9	680.9
60	345.3	640.0	363.9	679.8	341.7	647.9	360.3	687.3

[a] C_α-N-N-C_α (trans) torsion angle.
[b] Average of two closely spaced transitions.

3.7.3 In-Plane Nuclear Reorganization (IPNR)

Previous studies have attributed the missing Soret red shift to changes in the bond lengths and angles of the macrocycle caused by the substituents, termed in-plane nuclear reorganization or IPNR, but have not analyzed these effects in detail nor attempted to demonstrate that the bond lengths and bond angles actually change enough to cause the red shift.[36,37] Our analysis of the bond lengths and angles of energy-minimized NiT(Me)P and NiT(tBu)P (Table 3.7) did reveal significant structural differences which might conceivably be responsible for the red shifts. These changes included a pronounced decrease in the C_α-C_m-C_α angle, an almost equally large increase in the C_β-C_α-C_m angle, and some small bond length changes.

To evaluate the possible effects of these structural changes (IPNR), we investigated several energy-minimized constrained structures. In one calculation, the macrocycle bond lengths in NiT(Me)P with the correct amount of $1B_{1u}$ ruffling were fixed to the values in energy-minimized NiT(tBu)P (entry 4A, Table 3.4 & Table 3.5). In another calculation, both the bond lengths and the C_α-C_m-C_α bond angles of NiT(Me)P were constrained at the values seen in the energy-minimized structure of NiT(tBu)P (entry 4B). Neither of these constrained structures produced a significant red shift compared to the 60°-ruffled NiT(Me)P structure. Then, as a way of maximizing the IPNR, NiT(Me)P and NiT(tBu)P were each constrained to be planar (entries 4C and 4D) using the C_α-N-N-C_α dihedral angle constraint. IPNR must be very great for planar NiT(tBu)P and planar NiT(Me)P because steric interaction of the substituents with the macrocycle must be relieved entirely within the planar macrocycle. Further, because of the greater bulk of the tert-butyl substituents, IPNR must be tremendous for planar NiT(tBu)P. These planar constrained structures do yield significant bond-length and bond-angle differences between the tert-butyl and methyl derivatives, with the pattern of bond length and angle differences being similar to but not the same as for the unconstrained nonplanar energy-minimized structures (Table 3.7). However, a large red shift is not observed for the planar constrained structure of NiT(tBu)P relative to NiT(Me)P (Table 3.4); planar NiT(tBu)P actually shows a blue shift compared to planar NiT(Me)P. These results suggest that, contrary to recent proposals,[36,37] IPNR is unlikely to be the origin of the missing Soret red shift in NiT(tBu)P, although it may be important for other porphyrin systems. It should also be recognized at this point that significant bond-angle changes are expected for the nonplanar NiT(tBu)P structure even without a direct substituent IPNR effect but instead as a natural consequence of the large torsion-angle changes associated with nonplanar distortion.

Table 3.7 In-Plane Structural Parameters for Minimized & Constrained Planar NiT(Me)P and NiT(tBu)P Molecular Mechanics Structures.

Bond Length (Å) or Angle (°)	Minimized[a]			Planar[b]		
	NiT(Me)P	NiT(tBu)P	Diff tBu-Me	NiT(Me)P	NiT(tBu)P	Diff tBu-Me
Ni-N	1.9032±0.0005	1.8453d	-0.0579[d]	1.9486±0.0019	1.9644±0.0002	-0.0042
N-C_α	1.3800±0.0004[c]	1.3746	-0.0054	1.3879±0.0012	1.4134±0.0033[f]	0.0255
C_α-C_β	1.4310±0.0003	1.4308	-0.0002[e]	1.4307±0.0011	1.4215±0.0010	-0.0092
C_β-C_β	1.3301±0.0002	1.3364	0.0063	1.3203±0.0003	1.2937±0.0000	-0.0266
C_α-C_m	1.3893±0.0002	1.4006	0.0113	1.3871±0.0005	1.4097±0.0024[f]	0.0226
N-M-N	90.01±0.04	90.00	-0.01e	90.03±0.03	90.00±0.07	-0.03[e]
M-N-C_α	127.10±0.14	126.14	-0.96	127.69±0.16	127.20±0.79[f]	-0.49[e]
N-C_α-C_m	125.15±0.08	123.37	-1.78	126.60±0.24	129.66±0.95[f]	3.06
C_β-C_α-C_m	125.31±0.08	128.33	3.02	123.60±0.27	122.84±0.95[f]	-0.76[e]
C_α-C_m-C_α	119.58±0.02	115.83	-3.75	120.34±0.02	116.29±0.04	-4.05
C_α-N-C_α	105.80±0.04	107.71	1.91	104.59±0.06	105.60±0.01	1.01
N-C_α-C_β	109.37±0.05	108.15	-1.22	109.81±0.10	107.51±0.01	-2.30
C_α-C_β-C_β	107.72±0.04	107.98	0.26	107.83±0.09	109.69±0.26	1.86

[a] Unconstrained (non-planar) energy minimized structure.
[b] Constrained planar minimized structures.
[c] Range of bond lengths or bond angles.
[d] All values are identical so no range is given.
[e] Not statistically significant.
[f] The large ranges in some of the bond lengths and bond angles are probably related to the asymmetry induced by the tert-butyl group in the planar constrained structure.

3.7.4 Droopy Methyls

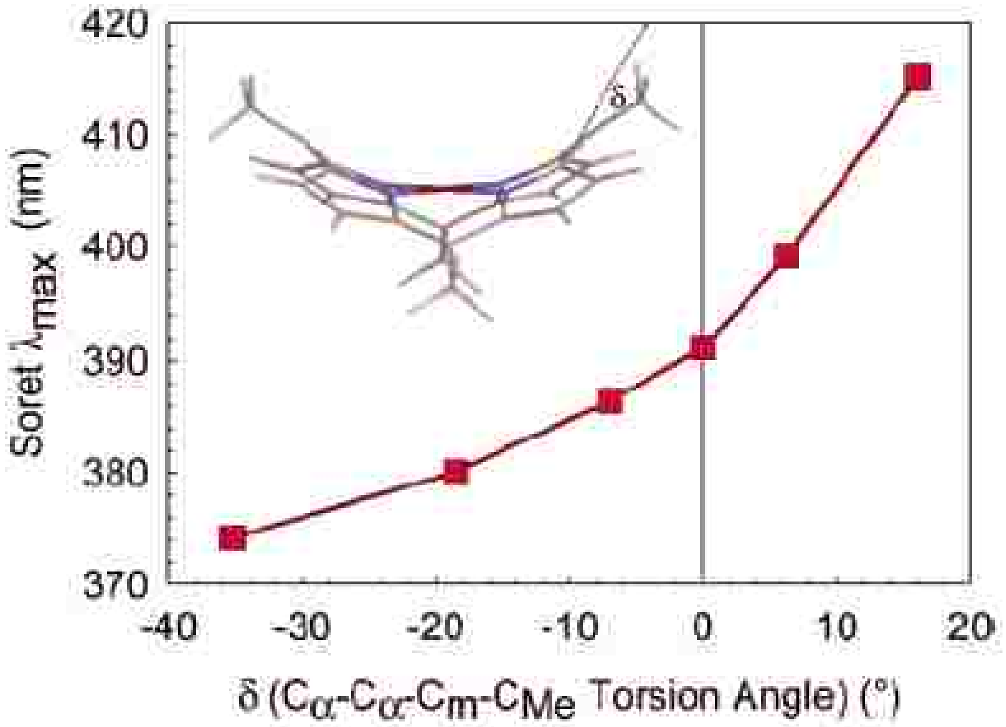

Figure 3.4 Effect of the methyl droop effect (illustrated in inset) on the wavelength of the Soret band for various methyl constraint angles δ from C_a-C_α-C_m plane. The methyl groups droop toward the macrocycle mean plane for NiT(Me)P artificially ruffled beyond its equilibrium geometry.

In examining the MM calculated structures for other clues as to what other factor or factors might explain the large red shifts for NiT(tBu)P, one apparent structural change in the NiT(Me)P structures over-ruffled to match NiT(tBu)P is a tendency for the methyl groups to "droop" back toward the porphyrin plane (see Figure 3.4). This substituent droop lowers the C_β-C_α-C_m-C_1 torsion angle to near zero, minimizing this strain contribution. The structural change is made possible by the lack of significant steric repulsion between the methyl group and the macrocycle in the over-ruffled porphyrin. The alkyl group position relative to the C_α-C_m-C_α plane is measured by the angle we label δ (i.e., the angle between the C_α-C_m-C_α plane and the C_m-C_1 vector (illustrated in Figure 3.4), as listed. In the energy-minimized structures of NiT(Me)P and NiT(tBu)P (entries 1A & 1B in Table 3.4), the alkyl group is either in or slightly above the C_α-C_m-C_α plane. In contrast, for the artificially ruffled energy-minimized constrained NiT(Me)P structures (entries 3A & 3B), the methyl groups droop toward the porphyrin plane ($\delta < 0$); the steric repulsion between the methyl and the porphyrin ring is simply not sufficient to hold the methyl above the C_α-C_m-C_α plane.

The curve in Figure 3.4, which was generated by constraining the methyl group's δ to different values using the fixed NiT(tBu)P macrocycle (entry 1B), demonstrates that only small deformations from the C_α-C_m-C_α plane are needed to cause significant shifts in the Soret band, especially for blue shifts caused by positive values of δ. A large blue shift arising from the methyl droop might explain why the constrained structures do not show the large red shifts. In other words, the absence of a large red shift could be an artifact of over-ruffling the porphyrin past its equilibrium geometry and an odd placement of the methyl groups, a structural effect most likely occurring in the DFT calculations as well.[36,37] Taking the 56°-constrained structure of NiT(Me)P (entry 3A) and constraining the methyl group into the C_α-C_m-C_α plane (entry 5 in Table 3.4 & Table 3.5) did produce an additional red shift, but it was only 122 cm^{-1} and clearly insufficient to explain the missing red shift (1963 cm^{-1}). Nevertheless, circumstances might arise for which δ is large and its contribution would become significant.

3.7.5 Higher-Order B_{1u} Deformations

The inability to generate significant red shifts using the mechanisms of IPNR or droopy substituents led us to more thoroughly investigate the structural differences between the T(tBu)P structures and the unconstrained and constrained T(Me)P. For both MT(tBu)P and MT(Me)P (M = Ni or Zn), it was shown by NSD analysis (Table 3.5) that essentially all of the calculated out-of-plane distortion (d_{total}) is localized in the B_{1u} ruffling-symmetry modes (B_{1u} total).

For the energy minimized structures of MT(tBu)P and MT(Me)P (M = Ni or Zn), this B_{1u} distortion is mainly in the first-order (lowest frequency) B_{1u} deformation, $1B_{1u}$, that is commonly referred to as ruffling, but there are significant amounts of the second-order $2B_{1u}$ and the third-order $3B_{1u}$ deformations as well (entries 1A/1B). These contributions are present irrespective of the porphyrin substituents (Me or tBu) and the central metal (though smaller out-of-plane deformations are overall observed for Zn than for Ni, consistent with the metal-size dependence).[23,24] For the energy minimized structures, all three contributions are much higher in MT(tBu)P than in MT(Me)P (entry 1B vs. 1A).

When the MT(Me)P porphyrin structure is artificially constrained to match MT(tBu)P using the C_α-N-N-C_α dihedral angles (entries 3A/3B), the large $1B_{1u}$ deformations of MT(tBu)P (entry 1B) were reproduced, but the smaller $2B_{1u}$ and $3B_{1u}$ out-of-plane deformations were not. The three B_{1u} modes are pictorially illustrated in

Figure 3.5. For the $2B_{1u}$ and $3B_{1u}$ modes, the 2-Å deformations shown are about a factor of 10 over the size of deformations that are actually observed for the sake of clarity. The significance of these deformations, is underscored when one considers the large deformation energies required to induce even small displacements for these high-order modes, given that the distortion energy depends on the square of the frequency of the out-of-plane mode (see caption of Figure 3.5).[7,8] A significant role for the $2B_{1u}$ and $3B_{1u}$ deformations would explain why INDO/S (and presumably DFT[35]) calculations on nonplanar porphyrin macrocycles generated by peripheral steric crowding give the large red shifts but the structures internally constrained to be nonplanar do not.

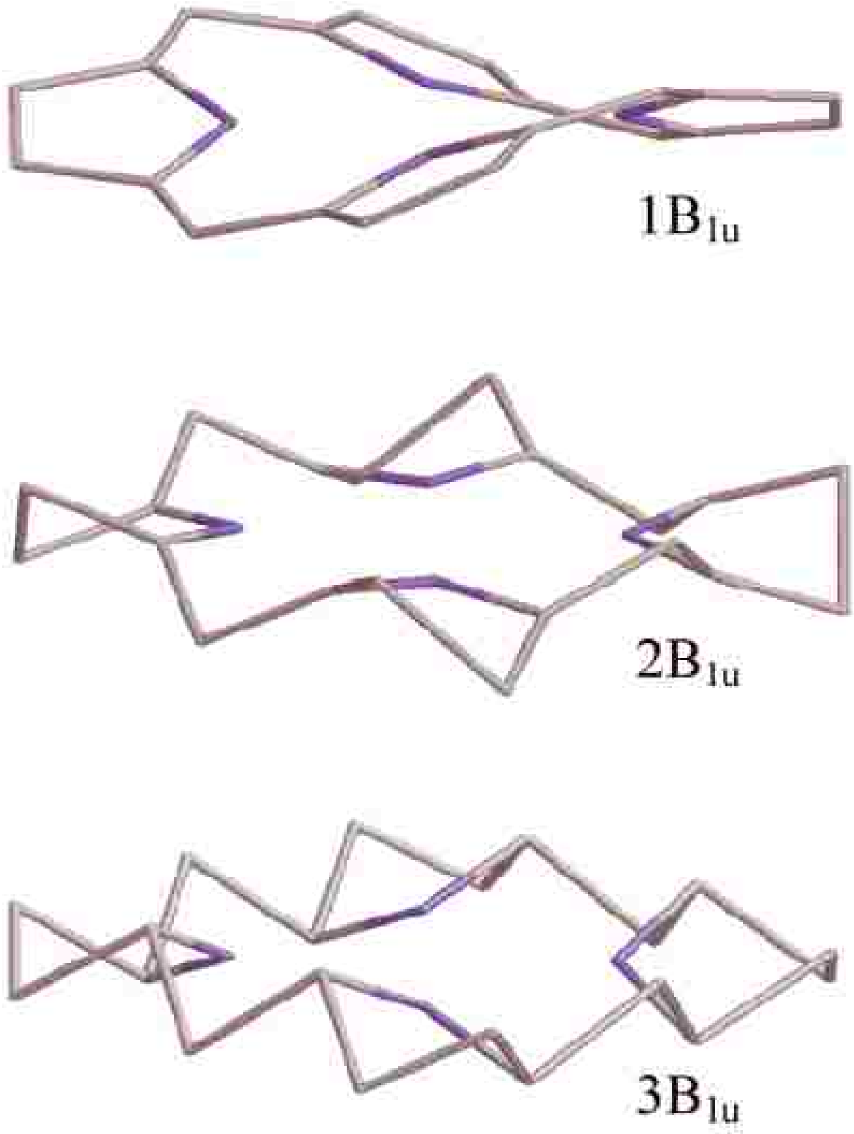

Figure 3.5. B_{1u} normal coordinates of the porphyrin macrocycle. The frequency of the $1B_{1u}$ deformation is the lowest (88 cm^{-1}), and the frequencies of the $2B_{1u}$ (516 cm^{-1}) and $3B_{1u}$ (727 cm^{-1}) deformations are much higher. Thus, using the harmonic approximation and the frequencies given, a deformation along the $2B_{1u}$ mode requires 34.5 times the strain energy of an equivalent deformation along the $1B_{1u}$ normal coordinate. A 2-Å deformation or displacement is shown for each normal coordinate, although such a large displacement for the high-order modes would never be observed experimentally because of the extreme strain energy required to produce the deformation.

In order to assess the whether the presence of these higher order deformations is particular to the case of MT(Me)P and MT(tBu)P (entries 1A & 1B) or is a pervasive trend among ruffled porphyrins, $2B_{1u}$ and $3B_{1u}$ deformations are plotted versus the $1B_{1u}$ deformation for nickel tetraalkylporphyrin complexes in Figure 3.6, both calculated and experimental (x-ray crystal structures). For the calculated structures, the $3B_{1u}$ deformation increases linearly with the amount of $1B_{1u}$ deformation. The linear relationship suggests an equal partitioning of strain energy into the $1B_{1u}$ and $3B_{1u}$ modes. In contrast, the $2B_{1u}$ deformation increases in a nonlinear fashion with $1B_{1u}$; the differences between the $2B_{1u}$ and $3B_{1u}$ contributions are discussed further below. The molecular mechanics structures on this point are in broad agreement with the X-ray crystallographic structures in that both data sets show deformations in these high-order modes and the deformations increase with increased ruffling, though the shapes of the curves and overall magnitudes are somewhat different in the two cases.

Crystallographic data has been reported for ZnT(tBu)P-(pyridine),[54] and NSD results for this structure are included in Table 3.5. The crystal structure contains approximately the same amount of total nonplanar deformation and $1B_{1u}$ ruffling deformation seen in the molecular mechanics structure, with additional small saddling (B_{2u}) and doming (A_{2u}) deformations, probably due to the presence of an axial ligand and to crystal packing forces not included in the calculation. In agreement with the molecular mechanics calculations, significant $2B_{1u}$ and $3B_{1u}$ deformations are seen in the crystal structure of ZnT(tBu)P(pyridine). However, the amount of these deformations is less than in the calculated structures, consistent with the dependence on the amount of $1B_{1u}$ deformation shown in Figure 3.6B for a wide variety of ruffled Ni porphyrin crystal structures. Nevertheless, it is clear that deformations in these high-frequency modes are present in nonplanar porphyrin crystal structures as they are in the calculated structures.

The following section discusses ways to induce the $2B_{1u}$ and $3B_{1u}$ deformations missing in the internally constrained structures so that we can then determine whether these modes produce large red shifts in the UV-visible bands similar to those seen for the sterically crowded porphyrins.

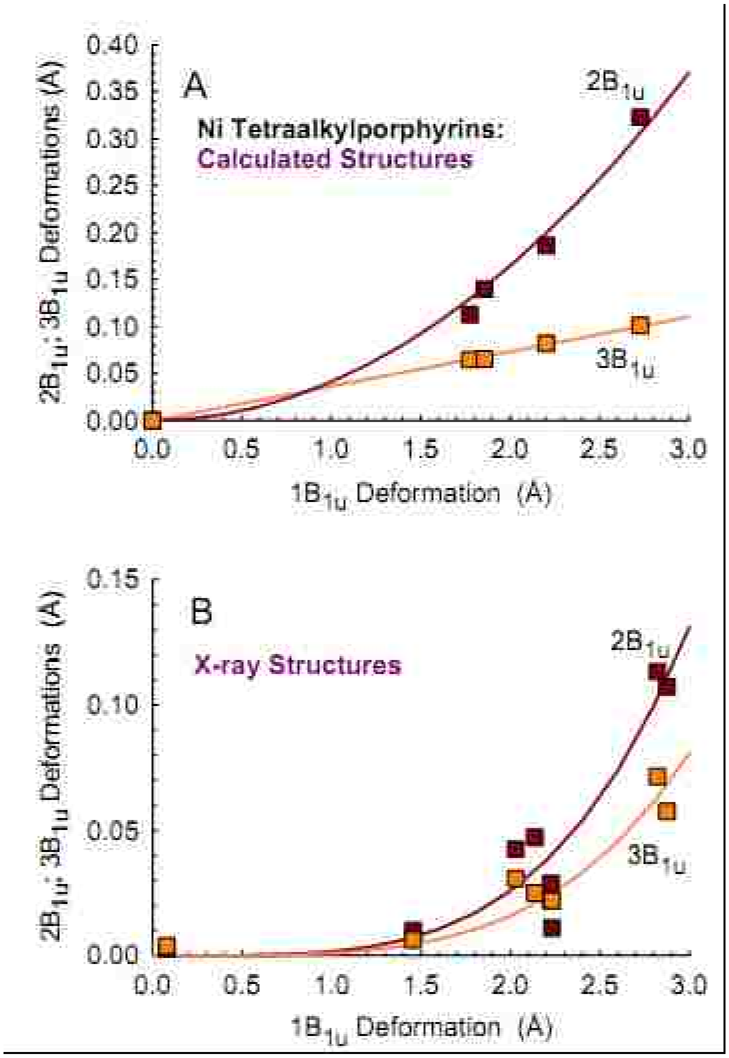

Figure 3.6. Plots showing the amount of $2B_{1u}$ deformation and $3B_{1u}$ deformation versus the amount of $1B_{1u}$ deformation for: (A) the molecular mechanics structures of nickel porphine NiP and the nickel tetraalkylporphyrins NiT(Me)P, NiT(Et)P, NiT(iPr)P, and NiT(tBu)P; and (B) the X-ray structures[55] of several ruffled nickel tetraalkylporphyrins, including NiP, tetragonal-NiOEP, NiT(iPr)P, NiT(cyclohexyl)P, NiTC$_5$TC$_5$P (compound 14, but with meso-pentyl groups), NiT(Bz)OEP, NiT(Bu)OEP, and NiBr8T(CF$_3$)P. The curves are approximated by least-squares fits of homogeneous polynomials: A— 1st and 2nd order; B— 4th order.

3.7.6 Non-Planarity Generated by Physical Means

In order to enable evaluation of the importance of the $2B_{1u}$ and $3B_{1u}$ modes by simulation, one way to generate them into the test structures would be to reverse the NSD procedure; that is, we could add deformations together to produce structures that are composed of specified amounts of these out-of-plane deformations. Such an approach is problematical because out-of-plane deformations and especially ruffling are associated with corresponding in-plane deformations due to radial contraction of the porphyrin core.[19,56] This is a necessary consequence of the virtual invariability of the bond lengths compared to bond angles and torsion angles. For the calculated constrained NiT(Me)P structures, the relationship between the in-plane contraction (along the lowest frequency $1A_{1g}$ deformation) and out-of-plane ruffling ($1B_{1u}$ deformation) is illustrated in Figure A-1. The excellent least squares fit to the theoretical expression (see caption of Figure A-1) shows that the in-plane contraction is simply a geometrical consequence of the ruffling. The in-plane deformations obtained from NSD should not be confused with IPNR. Because of this coupling of in-plane and out-of-plane NSD deformations, the generation of physically meaningful structures using reverse NSD is not generally practicable, although it can be used to study the geometric consequences of the $2B_{1u}$ and $3B_{1u}$ deformations (more on this in Section 3.7.7).

Rather than trying to generate structures from specified normal coordinate displacements, a more meaningful approach is to generate nonplanar porphyrins using various physical mechanisms besides replacing the alkyl substituents to see whether these structures also contain the $2B_{1u}$ and $3B_{1u}$ deformations missing in the internally constrained structures. One physical method used to induce further nonplanar deformations in the macrocycle of NiT(Me)P was forcing it to ruffle by introducing external van der Waals interactions with four extra atoms fixed in the porphyrin mean plane near the meso-methyl groups. After geometry optimization with MM, these fixed “dummy” atoms were then removed and single-point INDO/S calculations carried out. For this protocol, the IPNR due to localized substituent-macrocycle interactions is absent, and this ruffling mechanism may better mimic the steric interactions that cause out-of-plane distortions of tetrapyrroles in external scaffolding. For example, some hemoproteins contain hemes with moderately nonplanar structures that are thought to result primarily from nonbonding interactions with the surrounding protein (e.g., nitrophorins).[57] The energy-minimized NiT(Me)P structure obtained through external steric repulsion (entry 6A in Table 3.4 and Table 3.5) has approximately the same $3B_{1u}$ deformation as the energy-minimized structure of NiT(tBu)P, but it has much less of the $2B_{1u}$ deformation. As expected based on these high-order deformations, the INDO calculation does give a very large Soret red shift (1940 cm^{-1}) for this structure relative to the energy-minimized NiT(Me)P structure. A part of this red shift may result though from the position of the methyl group relative to the macrocycle, since a sizable value (6.4°) is found for δ (see Figure 3.4).

For another physically reasonable model structure, short hydrocarbon chains were attached across the opposing meso positions of NiT(Me)P to force the macrocycle to ruffle. When the chain contained eight methylene groups (compound **19**, entry 6B), the energy-minimized structure had approximately the same amount of $1B_{1u}$ deformation, a little less $2B_{1u}$ deformation, and slightly more $3B_{1u}$ deformation when compared with energy-minimized NiT(tBu)P (Table 3.5). Again, the INDO calculation gives a large red shift (2684 cm^{-1} relative to energy-minimized NiT(Me)P, only 258 cm^{-1} short of energy-minimized NiT(tBu)P). Approximately 5 nm of this 29-nm red shift (compared to entry 5) may result from the 4.8° movement of the meso-methylene groups above the C_α-C_m-C_α plane (angle δ in Figure 3.4). Most of the rest can be attributed to the high-order deformations, illustrating the profound consequences of these deformations.

3.7.7 Geometrical Interpretation of Higher-Order B_{1u} Deformations

The question then arises as to whether we can derive a simple structural interpretation of the effect of the contributions from the high-order B_{1u} modes. To do this, the NSD program was used in reverse to generate a structure with the $2B_{1u}$ and $3B_{1u}$ deformations of NiT(tBu)P and no other out-of-plane deformations. At first glance, this porphyrin structure appears to be almost planar because the high-order deformations are so small; these $2B_{1u}$ and $3B_{1u}$ deformations, as previously mentioned, are about a factor of 10 smaller than the 2-Å deformations depicted in Figure 3.5 that serve to qualitatively illustrate the structural effects). However, closer inspection reveals that the small high-order deformations actually cause significant torsional strain to be introduced into the structure.

As can be seen in Figure 3.5, deformations in the out-of-plane modes change the torsion angles of the skeletal bonds and reduce the overlap of the π p-orbitals of the macrocycle atoms hence the π-conjugation in the ring. This is true for all three B_{1u}

modes, but it is especially true for the $2B_{1u}$ and $3B_{1u}$ modes. We find that the $2B_{1u}$ and $3B_{1u}$ deformations cause a disproportionately larger increase in the twist about the C_α-C_m bonds (N-C_α-C_m-C_α torsion angle) when compared to the effect of the $1B_{1u}$ deformation. Specifically, the N-C_α-C_m-C_α torsion angle is 18° in this structure, a major portion of the 31° torsion angle found in the energy-minimized NiT(tBu)P structure. In other words, although the magnitudes of the $2B_{1u}$ and $3B_{1u}$ deformations are small, it is possible that they translate into significant changes in the N-C_α-C_m-C_α torsion angle to produce the large observed red shift.

This suggests a more direct way to include these deformations in a constrained structure. Thus, taking the structure of NiT(Me)P constrained to 56° (by twisting opposite pyrrole rings) and additionally constraining the N-C_α-C_m-C_α torsion angle to the value found in energy-minimized NiT(tBu)P (31°) yields a structure that incorporates much of the $2B_{1u}$ and $3B_{1u}$ deformations found in the energy-minimized NiT(tBu)P structure. As expected, INDO calculations for this structure again give a very large red shift (1913 cm^{-1}) in the Soret band (entry 7A in Table 3.4 and Table 3.5). It should be noted that the exact mixture of $2B_{1u}$ and $3B_{1u}$ deformations in the doubly-constrained structure does not exactly match that seen for energy-minimized NiT(tBu)P (entry 1B); instead, it is likely that increased $3B_{1u}$ deformation may compensate for the reduced $2B_{1u}$ deformation.

Although this doubly constrained structure accounts for most of the red shift in the absorption bands, still other factors need to be considered. It is necessary to correct for the aforementioned droopy methyl effect before essentially all of the red shift (2428 cm^{-1}) can be accounted for in the calculations (entry 7B in Table 3.4 and Table 3.5); the remainder can be attributed to the difference in electronic effect between methyl and t-butyl substituents.

This finding suggests that the increase in the N-C_α-C_m-C_α torsion angle directly causes the Soret red shift. It appears that an effect of the $2B_{1u}$ and $3B_{1u}$ deformations is simply to increase this torsion angle, already made large by the $1B_{1u}$ ruffling. To test this idea further, a plot of the calculated Soret wavelengths for all of the NiT(Me)P and NiT(tBu)P structures (constrained and unconstrained) versus the N-C_α-C_m-C_α torsion angle was prepared and is shown in Figure 3.7, with the experimental data shown also for comparison. Concomitant with the increase in the torsion angle should be a decrease in the π p-orbital overlap, which is known to display a cosine dependence.[58] The dependence on the torsion angle displayed in Figure 3.7 is well approximated by a cosine function, suggesting that the disruption of the π bonding gives the resulting red shifts. The destabilization of the porphyrin $a_{2u}(\pi)$ orbital is the greatest, closing the gap between the HOMO's and LUMO's.

As was mentioned in Section 3.6 , the absorption redshifts in the nickel tetraalkylporphyrins arise from a narrowing of the HOMO-LUMO energy gap due to greater destabilization of the HOMOs, especially the a_{2u} orbital, than the LUMOs with increased ruffling (Figure 3.3B). Examination of the orbital coefficients in the INDO results for NiP indicates that the a_{2u} HOMO has the most bonding character with respect to the C_α-C_m bond. Hence, it is consistent that an increase in the N-C_α-C_m-C_α torsion angle (twisting the C_α-C_m bond) leads to greater destabilization of the a_{2u} orbital than either the a_{1u} or e_g orbitals, thus narrowing the average gap between the HOMO's and

LUMO's that mix to give the observed Soret and Q transitions and the observed red shift. At higher ruffling, the a_{1u} (and somewhat the e_g) orbitals gain more bonding character with respect to the C_α-C_m bond and are also more acutely destabilized as the torsion angle increases but not to the extent of the a_{2u} orbital (Figure 3.3B). The gap thus decreases further and the red shift curve gets steeper.

Because of the structural relationship between $1B_{1u}$ ruffling and the other high-order B_{1u} deformations, it is likely that a large amount of ruffling will almost always bring along with it proportional contributions from the high-order B_{1u} deformations and thus give a large red shift of the UV-visible bands. Curiously, the mixture of $2B_{1u}$ and $3B_{1u}$ deformations generated by the four different mechanisms to ruffle NiT(Me)P (bulky substituents, intermolecular steric interactions, short straps, and additional torsional constraints) is somewhat different in each case. Typically, the $2B_{1u}$ deformation is more variable than the $1B_{1u}$ and $3B_{1u}$ deformations (Table 3.5 and Figure 3.6). For example, the $2B_{1u}$ deformation for energy-minimized NiT(tBu)P is larger than that for the other two physically meaningful cases considered. An examination of the deformation modes in Figure 3.5 suggests an obvious reason: the $2B_{1u}$ deformation mode moves the *meso* carbons toward one side of the porphyrin plane and the pyrrole β-carbons toward the other side of the porphyrin plane, making this deformation a very effective way to minimize local interaction between the bulky tert-butyl substituent and the pyrrole β-carbons. In contrast, for the $1B_{1u}$ and $3B_{1u}$ deformations, the meso carbons and pyrrole β-carbons move toward the same side of the porphyrin plane, making it difficult to relieve this localized steric interaction. All three B_{1u} modes move the meso carbon atoms (and their substituent) out of the mean plane, making all three deformations geometrically conducive to relieving the strain induced by steric crowding, short straps, or external steric interactions at the meso positions. Only for very bulky substituents such as tert-butyl should a large $2B_{1u}$ deformation be necessary to relieve local substituent steric strain.

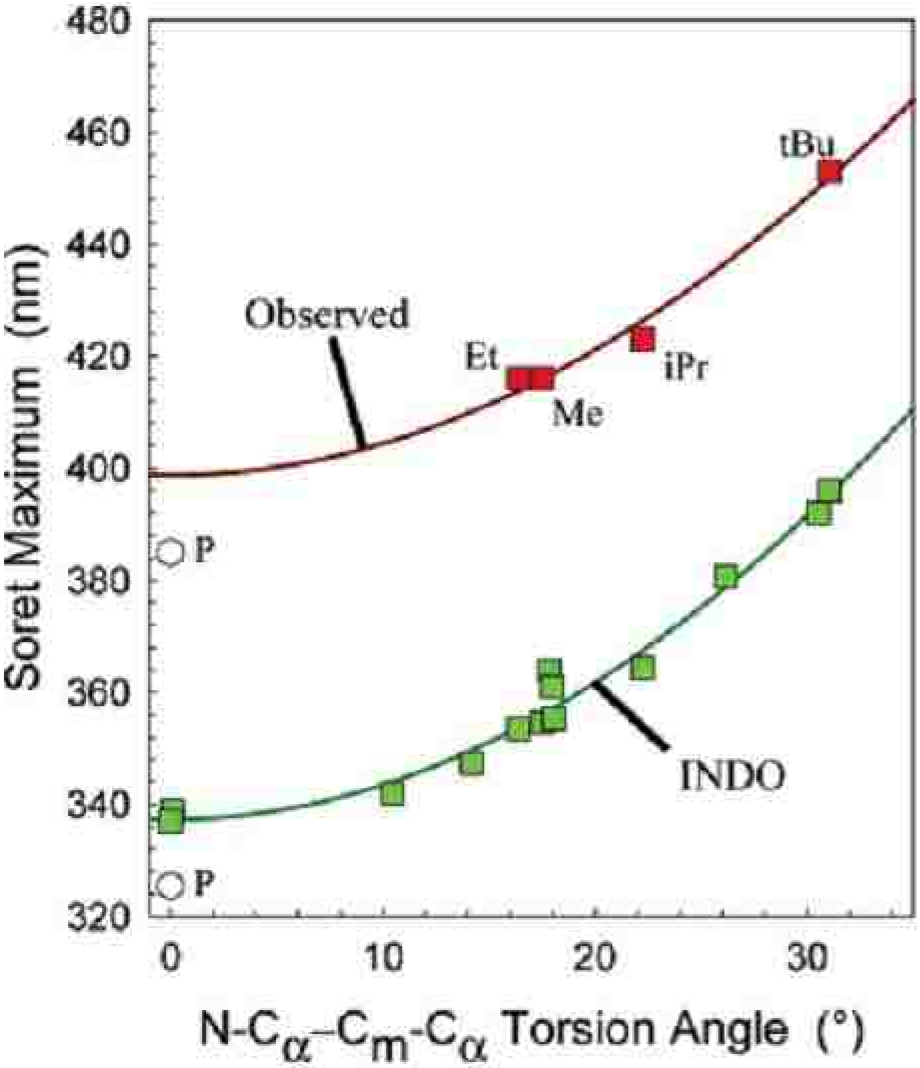

Figure 3.7 . Soret band wavelengths from INDO/S calculations versus the N-C_α-C_m-C_α torsion angles for all calculated NiT(Me)P and NiT(tBu)P molecular mechanics structures, constrained and unconstrained. The porphine points are not included in the least-squares fits because of the electronic effect of the replacement of methyl groups with hydrogens. The curve is approximated by an equation of the form $\lambda = \lambda_0 + a(1 - \cos\theta)$ in which λ_0 and a are varied to obtain the fit. For the calculated data, λ_0 and a are 337.3 and 404.9 nm, respectively. The experimental points for the nickel tetraalkylporphyrins are included for comparison; the fit parameters are 398.7 and 370.7 nm for λ_0 and a, respectively.

3.8 Bridled Chiroporphyrins

The effect of nonplanar deformation on the optical properties of the porphyrin macrocycle was also investigated experimentally and computationally by using the series of bridled nickel chiroporphyrins **12a-g**. In this series, the amount and type of deformation is expected to depend on the length of the straps connecting the adjacent meso positions, but the electronic effect of substituents is expected to be essentially identical. Additionally, IPNR, if not negligible, might even be expected to change with strap length in the opposite direction for the chiroporphyrin series relative to other strapped porphyrin series. An important additional feature of the series of bridled porphyrins is that IPNR, if it is not negligible, should be largest for the short straps because they force the bulky substituents nearer to the mean plane and, consequently, to interact more strongly with the macrocycle atoms than for long straps, which relax these repulsive interactions by out-of-plane deformation. This stronger interaction with the macrocycle for the short straps must take place within a more planar macrocycle, leading to greater IPNR. Thus, if IPNR were important and caused a significant red shift, then we would expect the largest red shift for the short straps and the more planar porphyrin, contrary to the observed trend in the UV-visible data.

The bridled chiroporphyrin series **12a-g** was synthesized[59,60] by our collaborators (group of Dr. Jean-Claude Marchon at CEA-Grenoble, France), who provided the samples for us to examine spectroscopically (UV-vis and Raman) in addition to performing molecular simulations. Although the chiroporphyrins have been synthesized with various core substituents, this chapter will focus on the nickel core for the same reasons as previously mentioned for the alkyl series.

Our collaborators characterized[59,60] some of the compounds by NMR spectroscopy and crystal X-ray diffraction, and of the nickel series, crystal structures were available for **12a** (n = 8) and **12c** (n = 10), obtained from two variants for each compound with orthorhombic or monoclinic crystal lattices. Each variant contained at least two independent molecules in the unit cell. Figure A-2 shows the crystal structure of one molecule of one crystalline form for each of **12a** (M = Ni) and **12c** (M = Ni). It is worth noting here that all of the nickel complexes **12a-g** adopt an αβαβ conformation, i.e. the four cyclopropyl group substituents are alternately displaced toward opposite faces of the macrocycle (αβαβ as shown in Figure A-2) rather than all being on the same side of the macrocycle (αααα). The latter stereochemistry (αααα) has been shown[59-61] to occur for the free base and Zn analogues of **12a**; it is not surprising that the short bridle (n=8) in this compound destabilizes the αβαβ conformer for which the bridle must cross sides of the macrocycle plane. The αααα conformer will become relevant in the next chapter; for the purposes of this study, the fact that the nickel series is overall structurally homologous (αβαβ) enables inter-comparison of the spectroscopic data within the series.

3.8.1 Spectroscopic Analysis of Bridled Chiroporphyrins

UV-vis spectroscopy was performed on the bridled nickel chiroporphyrin series **12a-g** to see how structural changes in the porphyrin accompanying bridle length affect the optical absorption bands. Raman spectroscopy was performed on the same series, as the frequencies of the structure-sensitive marker lines (e.g., ν_2) in the high-frequency region (1340-1640 cm^{-1}) of the resonance Raman spectrum are known to shift to low frequency with increased ruffling.[25,42] Also, our collaborators (Marchon group) performed ^1H NMR spectroscopy on the analogous free base series **12b-g** (M= 2H rather than Ni), as downfield shifts for the core protons, resulting from a combination of a decrease in ring current[62] and an increase in intramolecular H-bonding[63], could be used as markers for non-planarity. Of the free base analogues, **12a** (n=8) was left out because, as mentioned in Section 3.8 , this compound adopts the αααα conformation whereas the rest of the series is αβαβ.

The spectroscopic results are listed in Table 3.8 and plotted in Figure 3.8. The UV-vis study shows a surprising trend for the nickel bridled chiroporphyrin series: as the chain length of the bridle is increased from n=8, the Soret bands red-shift up to a maximum for n=12, then blue-shift slightly with continued chain length increase to n=16. The Raman ν_2 marker mirrors this behavior, and the NMR trend is similar even though the compounds contain a different core substituent (M= 2H rather than Ni).

That the red-shift indeed corresponds to ruffling of the porphyrin is supported by the fact that a similar dependence is observed with the two other spectroscopic measures of ruffling. However, it is surprising that the trends were not linear with bridle length, and the cause of the inflections in all the spectroscopic curves (Figure 3.8) is unclear.

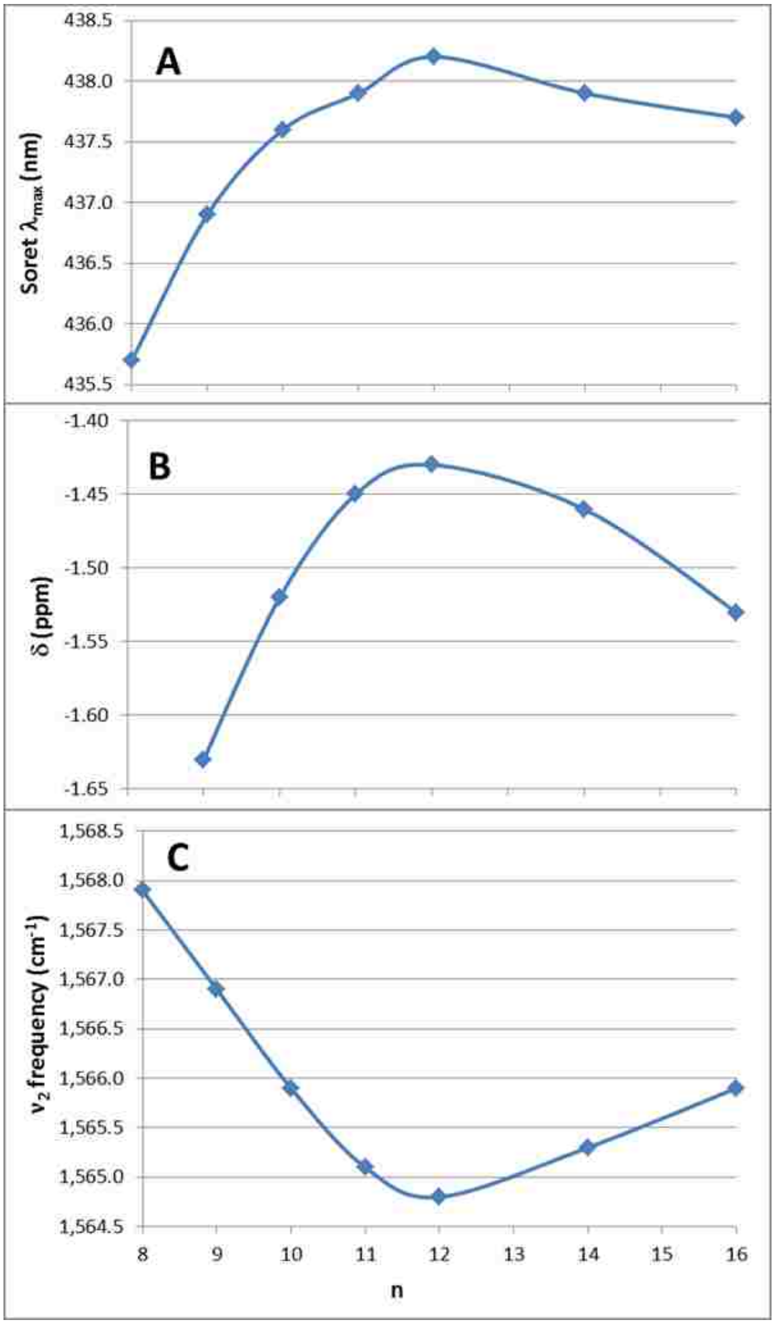

Figure 3.8 Structure-sensitive spectroscopic markers in bridled chiroporphyrins versus length of alkyl chain in bridles. (A) Soret band peak wavelengths of 12a-g (M=Ni) in CS_2; (B) ^{1}H NMR chemical shifts of the NH protons of 12b-g (M=2H) in $CDCl_3$ (data from Marchon group[55]); (C) Resonance Raman ν_2 line frequencies of 12a-g (M=Ni) in CS_2.

Table 3.8 UV-Visible, ^{1}H NMR, and Resonance Raman Spectroscopy Data and Time-averaged Out-of-plane Deformations from Molecular Dynamics Simulations for the Bridled Nickel Chiroporphyrin Series.

Compound	n	UV-vis B(0,0) (nm)	NMR[a] δ NH (ppm)	Raman ν_2 (cm^{-1})	MD d_{total} (Å)	MD d_{ruf} (Å)
12a	8	435.7	n/a[b]	1567.9	2.0035	1.9342
12b	9	436.9	63	1566.9	2.1200	2.0440
12c	10	437.6	100	1565.9	2.1684	2.1108
12d	11	437.9	115	1565.1	2.1760	2.1274
12e	12	438.2	131	1564.8	2.2525	2.2074
12f	14	437.9	115	1565.3	2.2718	2.2229
12g	16	437.7	105	1565.9	2.2700	2.1858

[a] For corresponding free base porphyrin; data from Marchon group[55].
[b] Not available because **12a** (M = 2H) adopts an αααα conformation.

3.8.2 MD Simulations of Bridled Chiroporphyrins

In order to elucidate how the spectroscopic trends discussed in the last section (Figure 3.8) correlate with the non-planar distortions of the porphyrin macrocycle, the structures of the compounds were simulated computationally. It would be difficult to obtain global energy minima for the bridled chiroporphyrins due to the numerous possible conformations of the flexible portions of the bridles. Therefore, rather than performing static molecular mechanics (MM) calculations, time averaged properties from molecular dynamics (MD) simulations were used. The MD procedure averages over many different conformations of the flexible straps, giving a better measure of the solution conformation than a single MM structure that might be trapped in a local minimum. For each compound in the series of bridled nickel chiroporphyrins **12a-g** (n= 8, 9, 10, 11, 12, 14, 16; M= Ni), multiple MD trajectories were obtained. Snapshot structures extracted from the MD trajectories at fixed intervals were analyzed by normal-coordinate structural decomposition (NSD). NSD analysis of the MD snapshot structures was done with a version of the NSD program modified to provide automation for processing multiple related structures. The individual deformations for all snapshot structures from each trajectory were then averaged to determine the average degree of nonplanar deformation, and the resulting deformations are presented in Table 3.8.

For comparison to the MD results, the available X-ray crystal structures were also analyzed by NSD data (Table A-7). It is evident from the crystal structure data that each independent molecule in the crystals exhibits a distinct degree of ruffling, with no apparent trend with the number of methylene groups. This suggests that crystal packing forces are large enough to obscure the porphyrin conformational differences that exist in solution and prevent them from being detected in the X-ray data. Given the flexibility of the straps, it is not surprising that packing forces would be important for these porphyrins. Notwithstanding, the nine structures of the crystalline bridled nickel chiroporphyrins **12a** and **12c** (M = Ni) show ruffling deformations of between 1.664 and 1.983 Å, with most of the nonplanar distortion being localized in the $1B_{1u}$ ruffling mode. The MD calculated average ruffling deformations for **12a** and **12c** (M = Ni) are 1.94 ± 0.02 and 2.10 ± 0.05 Å, respectively, only slightly higher than the range of total distortions observed in the crystal structures. This in some measure validates our calculated structures and the use of MD to determine the deformations.

The higher-order B_{1u} modes also show about the expected time-average deformations. For example, the MD simulations give $2B_{1u}$ and $3B_{1u}$ deformations of 0.194 and 0.091 Å, respectively, for the chiroporphyrin with the 16-carbon straps (**12g**), while the corresponding average $1B_{1u}$ ruffling is 2.186 Å. For comparison, the "raw" (unbridled) secondary alkyl substituted porphyrin studied above, NiT(iPr)P, exhibits similar values (2.203, 0.186, and 0.082 Å). Interestingly, there is also a trend toward larger $2B_{1u}$ deformations (0.229 Å for **12a**) as the straps shorten, signaling a stronger local steric interaction of the cyclopropyl group with the macrocycle; at the same time, the $3B_{1u}$ deformation remains nearly the same at 0.080 Å for **12a**.

3.8.3 Relating Ruffling to Spectroscopic Results for Bridled Chiroporphyrins

Figure 3.9 plots the UV-visible, ^{1}H NMR, and resonance Raman spectral parameters discussed in Section 3.8.1 (Table 3.8) versus the time-averaged ruffling of the nickel chiroporphyrin complexes obtained from MD simulations. The NMR and Raman spectral parameters, known to be affected by ruffling, showed the expected correlations to the simulated deformations, as did the optical absorption bands. The scatter was somewhat greater for the NMR data (Figure 3.9B), perhaps as a result of plotting the NMR resonances for the free-base chiroporphyrin series versus the simulated ruffling for the nickel series. Remarkably, these trends could be observed even though the ruffling varies by only about 15% over the whole series. This range is small compared to the range of distortions investigated in the other series of porphyrins, so the shifts in the absorption spectra were relatively small. The red shift depends approximately linearly on the ruffling for the small range of ruffling values spanned by the series (Figure 3.9A).

Together, the correlation of the Soret peaks to the simulated ruffling and its consistent trending with the two other spectroscopic indicators of ruffling provide further evidence that the absorption red shifts arise from ruffling distortions.

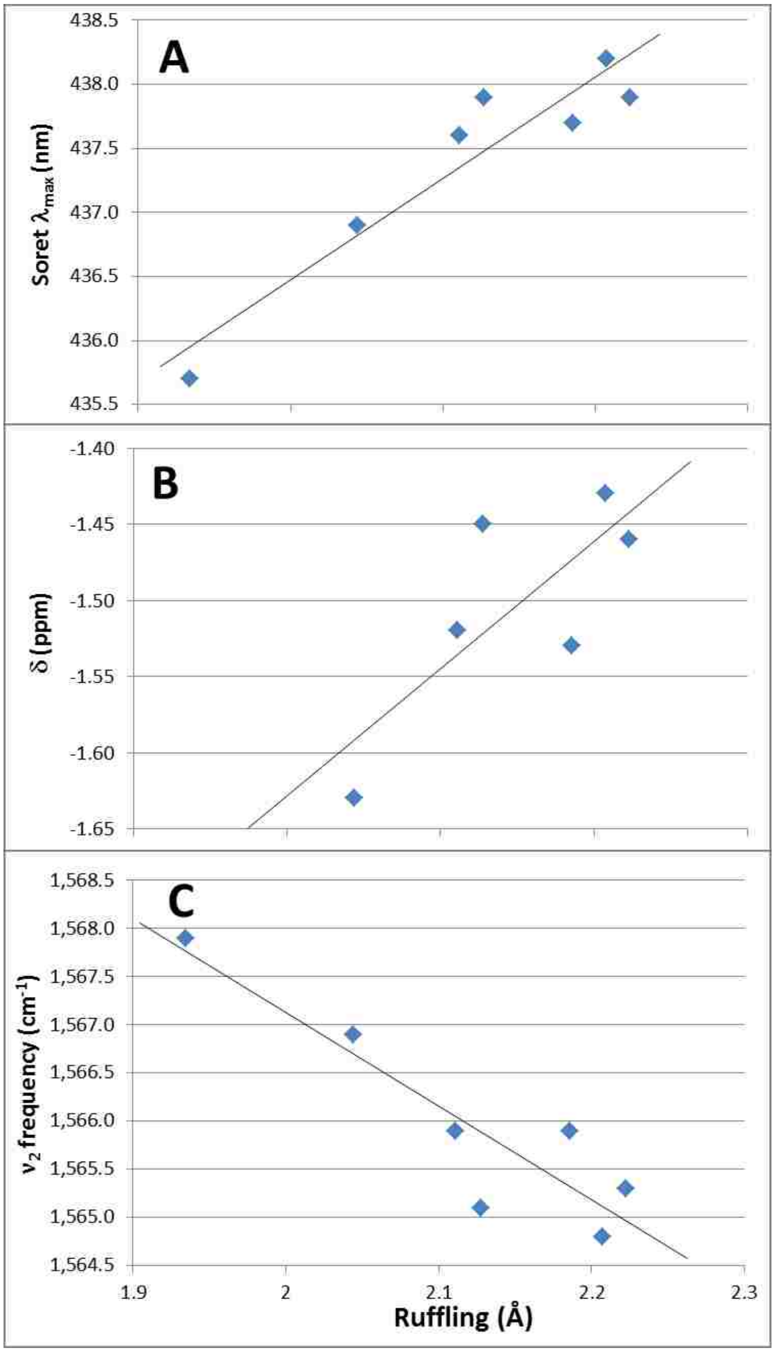

Figure 3.9 Structure-sensitive spectroscopic markers in bridled chiroporphyrins versus time-averaged ruffling deformations from MD simulations for the nickel series. (A) Soret band peak wavelengths of 12a-g (M=Ni) in CS_2; (B) ^{1}H NMR chemical shifts[55] of the NH protons of 12b-g (M=2H) in $CDCl_3$; (C) Resonance Raman ν_2 line frequencies of 12a-g (M=Ni) in CS_2. Lines represent least-squares fits to data.

3.9 Conclusions and Implications

3.9.1 Origins of the Red Shifts in the UV-Visible Bands.

The resolution to the question of whether the large red shifts observed for sterically crowded porphyrins are caused by out-of-plane distortions has ultimately turned out to be somewhat complex, even for the series of tetraalkylporphyrins having conserved substituent patterns, similar substituent electronic effects, and a deformation of only one symmetry-type (B_{1u}). If we take the meaning of ruffling in the loose sense often employed, the answer is clearly yes; the summation of the B_{1u} nonplanar deformations does cause most of the large red-shift seen for MT(tBu)P (M = Ni, Zn, or H_2). If we take the more specific definition of ruffling to mean only the deformation along the lowest-frequency $1B_{1u}$ mode, then technically the answer is no, as this deformation does not produce all of the observed red shift for the tetraalkylporphyrins. A pure $1B_{1u}$ deformation does nonetheless produce an appreciable red shift, especially in the region of large deformation. All three modes apparently cause red shifts of varying amounts in the tetraalkylporphyrins cooperatively, and these will contribute with other factors (electronic, substituent orientation, etc...) to the observed shifts.

Perhaps the important point is that all three B_{1u} deformations are usually jointly manifested in physical structures (unlike in those artificially constrained), so that when the lowest energy mode, which is greatest in magnitude, is seen, the presence of the other two can be anticipated. In the case of the bridled nickel chiroporphyrins, the amount of ruffling distortion was actually reduced, causing blueshifts, if the chains were too short;

this is in contrast with most other strapped porphyrins for which shorter chains cause increased nonplanar deformation and result in red-shifted absorption bands (e.g., compound **19**, entry 6B in Table 3.4 and Table 3.5). Thus regardless of the mechanism used to induce nonplanar distortion in strapped porphyrins, the more nonplanar porphyrins consistently give a red shift, and this red shift can usually be detected even when the change in deformation is small as it is for the bridled porphyrins.

In regard to the recent studies attributing the redshifts to IPNR,[36,37] we found that the Soret band shifts are apparently not very sensitive to IPNR. Our findings indicate that the failure to reproduce the large red shifts in structures generated by using torsional constraints across the macrocycle is in reality an artifact of the procedure used to constrain the macrocycle. Ruffling the porphyrin macrocycle in this manner simply does not generate the high-order $2B_{1u}$ and $3B_{1u}$ deformations that are a natural consequence of a strained porphyrin system. This artifact of the constraint method has led to an underestimation of the importance of nonplanarity and a mistaken belief that the missing Soret red shift is the result of IPNR.[36] Other methods of inducing the ruffling such as constraining the z-displacements of the meso carbons[37] to their values in energy-minimized NiT(tBu)P give slightly more of the high-order B_{1u} deformations and correspondingly larger red shifts but still considerably underestimate the red shifts. These recent studies by Ghosh and DiMagno, while reaching the wrong conclusions, nevertheless have ultimately led to a more complete understanding of the various contributions to the band shifts. It is clear from the foregoing discussion that delineating electronic and structural effects on the optical spectra of nonplanar porphyrins can be complicated even for the tetraalkylporphyrins which have well-controlled conformational and electronic properties. It is important not only to choose appropriate model systems but also to be aware of possible systematic errors and artifacts in the calculations.

It is also likely that some of the confusion surrounding the origin of the red shift is related to the nonlinear relationship between the Soret band red shift and ruffling (Figure 3.3A). Because the nonplanarity-induced red shift may be small (as is the energy cost for this amount of deformation) when the change in nonplanarity occurs in the flat region below about 1.5 Å of ruffling, model compounds which differ in macrocyclic distortion within this region give such small band shifts that it is easy to lose the effect of nonplanarity within the variations due to substituent effects and other influences on the spectra. For example, simply replacing the four meso hydrogen atoms with methyl groups consistently causes a 15-20 nm red shift (Table 3.6), irrespective of the degree of ruffling or the metal in the core. This effect is far larger than the red-shift expected for a slight or moderate change in ruffling of the porphyrin in the flat region of the curve in Figure 3.3A.

3.9.2 Application of the Spectra-Structure Correlations

An important practical question is whether the ruffling/ Soret red-shift correlation might be usefully employed in reverse as a tool to obtain structural information about porphyrin cofactors in proteins, for biological understanding as well as guidance for biomimetics. While it appears this correlation can be a helpful, facile technique, it should of course be used with cautiousness. It is worth noting that spectral parameters used for structural correlations are oftentimes not directly tied to the causal structural parameters but instead to larger structural changes that can be easily measured and that change systematically with the causal parameter. An illustrative example is the well-known negative correlation between some Raman line frequencies and the porphyrin core size[16,64] in which case it is thought that the actual cause of the frequency shift is the small change in the C_α-C_m bond length rather than the core size directly; the core size is simply a large structural change that can be accurately measured and which just happens to correlate with the C_α-C_m bond length and consequently the Raman frequency shifts. A somewhat similar situation apparently exists for the correlation between the Soret red shift and ruffling of the porphyrin macrocycle. The structural parameter that we can easily measure is the deformation in the lowest-frequency $1B_{1u}$ mode (i.e., ruffling) which only accounts by itself for a part of the redshift. The two high-frequency B_{1u} modes also have a large influence on the red shift, but their deformations are typically so small that to measure them requires highly accurate crystal structures and NSD analysis. Therefore, just as in the case of the Raman core-size correlation, we must rely on a separate fortuitous relationship that may exist, as shown in Figure 3.6, between the ruffling that we can measure ($1B_{1u}$) and the prevailing $2B_{1u}$ and $3B_{1u}$ deformations. The relationships were shown in both X-ray crystal and MM calculated structures for physically meaningful distortion mechanisms, certainly for distortions caused by substituent crowding, strap-induced strain, and external steric perturbations that cause ruffling (Table 3.5). There might also be unforeseen physical circumstances for which relationships between the first-order and high-order modes do not exist, so the red-shift correlation with nonplanar distortion would lose accuracy. Hence, the use of the UV-visible band red shifts as a measure of porphyrin nonplanarity in protein systems necessitates great caution and should be done in conjunction with other spectroscopic measures when possible. Further attention is of course due to avoid confounding substituent-induced effects on the UV-visible spectra, including electron withdrawal/donation, hyperconjugation, and local substituent distortion.

The spectra-structure correlation can also be used, together with other substituent electronic effects, to design desired optical properties into porphyrins for various applications such as solar energy conversion, organic light emitting diodes, photocatalysis, and photodynamic therapy, all of which require fine-tuning of the optical properties of the chromophores. Although this work has focused on the absorption band shifts, it is highly likely that other physical and chemical properties will also be influenced by the high-order mode deformations discussed (and perhaps others as well). Independent of the absorption band redshift issue, we have demonstrated a combined NSD-MM-INDO computational framework that provides an effective methodology for quantifying macrocycle deformations and evaluating their effects on the electronic spectra of porphyrins, a technique that will prove applicable to the evaluation of other structural correlations.

CHAPTER 4: AFFECTING BINDING OF AXIAL LIGANDS TO PORPHYRINS WITH NON-PLANAR DEFORMATIONS

4.1 Introduction

The versatility of porphyrins was illustrated in Chapter 1 by the fact that there are twelve sites on the periphery on which to add substituents of various properties while maintaining key properties (aromatic character) of the macrocycle. For metalloporphyrins, there is the added possibility of additional axial ligands at the metal core, depending on the metal and its valence electron shell. In this chapter, we investigate a novel method for initiating a large scale alteration of the structure and shape of a porphyrin macrocycle and its attached peripheral architecture triggered by an axial ligation event (or a photo-excitation event), which brings about a change in the electronic structure of the metal in the porphyrin core. The structural change at the core is most effectively amplified to the periphery when the *type* of deformation is altered.

When the metal ion incorporated in the porphyrin is nickel(II), uptake of an axial ligand (or photon absorption) results in alteration of the *d*-electronic configuration of the nickel(II) atom as an electron is promoted from the bonding orbital to the antibonding orbital, inducing a structural change at the metal, most significantly resulting in a higher equilibrium Ni-$N_{pyrrole}$ bond distance. Nickel(II) was chosen as the core metal in particular because the change in the equilibrium Ni-$N_{pyrrole}$ bond distance for its contracted (low-spin) and expanded (high-spin) electronic states is relatively large (>0.2

Å) and, as will be discussed shortly, is in a suitable range. Further, the metal electronic state can be reversibly switched by uptake/release of an axial ligand at the metal (or absorption/emission of a photon by the porphyrin macrocycle, or a combination of photoexcitation and ligation events).[65,66]

The tendency of low-spin nickel(II) ions to cause nonplanarity of the porphyrin macrocycle has been widely documented in the literature,[56,67] with ruffled or saddled conformations generally favored due to the short equilibrium Ni-$N_{pyrrole}$ bond distance. Although the expansion at the core is small in absolute terms (~0.2 Å) when high-spin nickel is formed upon axial ligation (or π–π^* photo-excitation), it is not readily accommodated purely by in-plane distortion of the porphyrin due to the strong bonds within the macrocycle. Instead, accommodation of nickel ion expansion relies on changes in the soft out-of-plane deformations, as the expanded core is more easily accommodated by other modes of non-planarity such as doming. Put another way, the net result of the nickel(II) electronic change is to switch the metal core from a state in which it is smaller than the unstrained porphyrin core size, causing a core-contracted ruffled or saddled conformation, to a state in which the nickel ion is larger than the unstrained porphyrin core, favoring a core-expanded planar conformation or a nonplanar conformation in which large metal-nitrogen distance are favored such as the domed conformation.[68]

In this chapter, we investigate how axial ligation relates to porphyrin non-planarity and how this relationship may be applied. Molecular simulation, UV-visible absorption spectroscopy, resonance Raman spectroscopy, and normal-coordinate structural decomposition analysis are used to elucidate the effect of nonplanarity of nickel porphyrins on their affinity to bind axial ligands. Conversely, since ligand binding is a driving force for switching the porphyrin conformation in molecular devices based on nickel-porphyrin actuators, the effect of the ligation on the structure of the porphyrin is also determined. Finally, we examine how the comparatively small structural change arising at the nickel ion (~0.2 Å change in the Ni-N bond distance) can be amplified via nonplanar porphyrin deformations into large structural differences at the periphery of the porphyrin ring, and even greater motions of the ring substituents. An example of the application of this 'triggered' switch might be used to modulate and control the shape of the nickel porphyrin is discussed in regard to a bridled porphyrin that possesses straps that allow it to function in molecular devices such as nanotweezers.

4.2 Background

Although the relationship between axial ligation and non-planarity has not been systematically studied, previous anecdotal evidence has suggested that peripherally crowded and very nonplanar nickel porphyrins (*e.g.,* NiDPP and NiOETPP, see Figure B-3) tend not to bind axial ligands under conditions where nominally planar porphyrins with similar substituent electronic effects (*e.g.,* NiOEP and NiTPP, see Figure B-3) do bind ligands.[69-71] Axial ligand binding has been observed in very nonplanar porphyrins but only when electron-withdrawing substituents are present as *e.g.*, for NiOETNP[72] and $NiBr_4(CN)_4TPP$ (see Figure B-3).[73]

In the following sections, examples of axial ligands in naturally occurring porphyrins will be presented and the possibility of a biomimetic switch triggered by an axial ligation event.

4.2.1 Biological Axial Ligation Induced Conformational Change in Hemoglobin

An inspiring biological paragon is the axial binding of an oxygen molecule to the heme (iron porphyrin) at the heart of the hemoglobin protein in blood that transports oxygen from the lungs to the cells of the body. The structural changes that propagate through the grand tetrameric hemoglobin protein upon binding of a tiny oxygen molecule are graphically illustrated at the following web-link: Hemoglobin_Oxy/Deoxy_States.

The notion that a ligand's local impact on the core metal is translated to large structural changes in the macrocycle itself and on its periphery and surroundings illustrates how the interplay between axial ligation and porphyrin non-planarity may be harnessed for a variety of applications such as molecular sensing and chemically-controlled switches. In addition to the possibility of inducing changes in structural conformation via ligation, it may also be possible to influence the binding and dissociation of an axial ligand to a porphyrin via the external environment of the porphyrin, resulting in further applications in controlled enzymatic bioprocessing, targeted drug delivery systems, and separation/recovery systems.

4.2.2 Bridled Chiroporphyrins and their Conformers

In the previous chapter (Section 3.8), it was indicated that the bridled porphyrin complex BCP-8 adopts two different conformations (αβαβ or αααα) depending whether the core metal is nickel or zinc.[59-61] An ability to reversibly switch between the two conformers (αααα/αβαβ) might potentially lead to development of chemically actuated porphyrin-based molecular mechanical devices (*e.g.,* nanotweezers). Metal exchange reactions (Zn/ Ni) may be one way to switch BCP8. However, metallation and demetallation of porphyrin macrocyles is typically a low rate process; a metal ion is both slowly inserted into the cavity of porphyrin and slowly removed in the reverse process.[1]

Another possible means of activating a conformational switch in BCP8 that will be investigated in this chapter is the use of an axial ligation process (or, alternatively, a photoexcitation process) to enlarge a nickel(II) atom at the porphyrin's core. Addition of axial ligands (or photoexcitation) would transform the Ni atom to a d,d excited state ("high spin") from its "low spin" state. Low spin Ni(II) has an electronic configuration that favors relatively short equilibrium Ni-N bond distances, resulting in a tendency for the porphyrin macrocycle to adopt a nonplanar conformation (*e.g.*, a ruffled structure).[24] In high-spin nickel(II) porphyrins, the equilibrium Ni-N bond distance because of the presence of an electron in the anti-bonding orbital. The equilibrium length of the Ni-$N_{pyrrole}$ bond for high-spin nickel ion has been determined in a previous study[74] to be 2.07 Å (~0.2 Å elongation); this value was obtained by varying the length parameter while calculating the energy-optimized structure of nickel(II) tetra(N-methyl-pyridinium) porphyrin bis-imidazole until the calculated structure best matched the crystal structure. Interestingly, this bond length for high-spin nickel is the same as that used in the force field for zinc(II),[75] leading us to believe that if NiBCP-8 will bind axial ligands, it may adopt a similar conformation to ZnBCP-8.

4.3 Experimental

Given the limited number of studies of the relationship between tetrapyrrole nonplanarity and axial ligand affinity, we decided to systematically study the relationship between tetrapyrrole conformation and axial ligand affinity using a series of nickel porphyrins with increasingly nonplanar macrocycles generated by the more bulky *meso* alkyl substituents. Initially, the low-spin 4-coordinate forms of the nickel(II) tetraalkylporphyrins are simulated using molecular mechanics (MM) calculations to examine the conformational landscape. The nonplanar distortions in the MM structures, as well as those in similar X-ray crystal structures reported in the literature, are quantified using normal-coordinate structural decomposition (NSD). UV-visible absorption and resonance Raman (RR) spectroscopy are employed to characterize the nickel(II) tetraalkylporphyrins in both non-coordinating solvents (dichloromethane, carbon disulfide, benzene) and strongly coordinating (pyrrolidine, piperidine) solvents to determine the effect of nonplanarity on axial ligand affinity. Conversely, the effect of axial ligation on the porphyrin conformation is then computationally investigated. Finally, a prototypical nanotweezer is investigated as an example of the application of axial ligation in designing a switchable molecular device.

4.3.1 Molecular Mechanics Calculations.

MM calculations were carried out using Cerius^2 software from Accelrys (San Diego) on a Silicon Graphics Octane workstation. They were performed using the force field developed[20] and refined[68] by Shelnutt and coworkers. The force field is based on DREIDING II, modified to include force constants and equilibrium values for bond lengths, bond angles, torsion angles, and improper torsion (umbrella) angles of the porphyrin macrocycle, as well as parameters describing the van der Waals and electrostatic interactions for the porphyrin macrocycle.[20] The force field has been used extensively to calculate the structures of porphyrins and to investigate some dynamic processes such as axial ligand rotation[76,77] and substituent rotation.[78,79]

For the high-spin and axially-ligated nickel complexes, an equilibrium Ni-$N_{pyrrole}$ bond length of 2.07 Å was used in the calculations. This value was obtained by varying the equilibrium Ni-$N_{pyrrole}$ bond length in the energy-optimized structure of nickel(II) tetra(N-methyl-pyridinium)porphyrin bis-imidazole until the calculated structure best matched the crystal structure.[80] The force constant for the Ni-N_{ligand} bond was taken to be the same as for the low-spin Ni-$N_{pyrrole}$ bond. Note that the Ni-$N_{pyrrole}$ bond length of 2.07 Å is the same as that used for zinc(II).[67] The $N_{pyrrole}$-Ni-N_{ligand} angle was modeled using default parameters, with a θ-harmonic potential, a minimum at 90° and a force constant of 100. The van der Waals parameters for high-spin and axially ligated nickel have little effect on the structure and were approximated using the value for zinc(II) in the DREIDING II force field.[81] The torsion angle force constant for rotation about the Ni-

N_{ligand} bond was set to zero. For consistency with earlier studies, a dielectric constant of 2.64 (for carbon disulfide) was used in the calculations.

4.3.2 Normal-Coordinate Structural Decomposition.

Normal-coordinate structural decomposition (NSD)[82] was used to analyze the out-of-plane (and in-plane) deformations present in the porphyrin crystallographic and MM structures. The NSD method characterizes the porphyrin conformation in terms of equivalent displacements along the normal coordinates of the D_{4h}-symmetric porphyrin macrocycle. Typically, the largest static distortions of the porphyrin macrocycle occur along the softest normal modes, so that the greatest contributors to the nonplanar distortion are the lowest-frequency normal coordinates of each out-of-plane symmetry type (B_{1u}, B_{2u}, A_{2u}, E_g, and A_{1u}). These deformations correspond to the symmetric distortions commonly observed in crystal structures and are named ruffling (*ruf*), saddling (*sad*), doming (*dom*), waving (*wav(x,y)*), and propellering (*pro*) (see Figure 1.2 for illustrations of the *ruf*, *sad*, *dom* and *wav* deformations). Mixed together, they give asymmetric macrocyclic distortions of various types, and (vectorially) adding the projections of the total distortion along only these six normal coordinates typically simulates the actual out-of-plane distortion reasonably accurately. In the present study, only the deformations for these lowest-frequency normal modes are discussed. (Positive and negative deformations also have meaning, but for these symmetrically substituted porphyrins the signs of the deformations are dependent on the way the molecule is oriented for the NSD analysis and so they have been omitted in the Tables in the text.)

Although the contributions to the distortion from the high frequency modes are small, they may have important consequences for the optical spectra and other properties.

4.3.3 UV-Visible Absorption Spectroscopy.

UV-visible spectra were obtained using a HP 8452A diode array spectrophotometer (Colorado Springs, CO) and a 5-mm path length quartz cell. The absorption spectra were measured in dichloromethane, benzene, pyrrolidine, or mixtures of benzene and pyrrolidine. The peak positions were obtained by curve-fitting the absorption spectra with Gaussian lines using the program PeakFit (SSPS, Richmond, CA).

4.3.4 Resonance Raman Spectroscopy.

Resonance Raman (RR) spectra of porphyrin solutions were obtained using a partitioned quartz cell and a dual-channel spectrometer[83] or a CCD spectrometer[84] described previously. The scattered light was collected at 90° to the directions of propagation and polarization of the exciting laser beam. The partitioned cylindrical Raman cell was rotated at 50 Hz to avoid local heating and to probe alternately the sample and reference solutions. The typical conditions were 50-60 mw of laser power, 5-cm^{-1} spectral slit width, 8-10 scans with 0.3-cm^{-1} step increments, and 0.5-s integration times on individual scans for the dual-channel spectrometer. The spectra from the dual-channel spectrometer were corrected for the nonlinear response of the spectrometer and PMT detector. For the spectra obtained with the CCD spectrometer, low power (<20 mW) was used with a 3x3mm cross section quartz cell at room temperature. The 413.1-nm line of a Coherent INNOVA krypton ion laser (Santa Clara, CA) was used as the excitation source, and NiTPP in neat benzene was employed as the reference solution for the Raman line frequencies. For the CCD spectrometer, the spectra were obtained in 10 minutes or less. Polarized spectra were measured by passing the scattered light through a Polaroid sheet oriented parallel or perpendicular to the polarization direction of the incident beam, followed by a polarization scrambler in front of the spectrometer entrance slit.

4.3.5 Materials

NiTPP was obtained from Porphyrin Products (Logan, UT) and used without further purification. NiT(Me)P, NiT(Et)P, NiT(Pr)P, NiT(Pe)P, NiT(iPr)P, NiT(cH)P, and NiT(tBu)P were synthesized in our group,[85] as was NiT(cPr)P.[61] Benzene, piperidine, pyrrolidine, and 2,3-dichloro-5,6-dicyano-1,4-benzoquinone (DDQ) were of the highest purity available from Aldrich (St. Louis) and were used as received.

4.4 Structures of the Nickel Tetraalkylporphyrins

In order to investigate the effects of non-planar deformations on ligation, we first examine, before their ligated counterparts, the structures of the *unligated* (low-spin, 4-coordinate) nickel tetraalkyl porphyrin series via MM simulations and perform NSD on the energy-optimized structures to quantify the deformations. We also examine the accessibility of different conformations as will be pertinent to the discussion of switchable molecular devices.

The nickel tetraalkylporphyrins used in the present study (see Figure 4.1) provide a series of compounds with similar substituent electronic effects but with varying degrees of ruffling due to differences in the steric bulk of the substituents. This provides a practical way to investigate the effects of porphyrin macrocycle nonplanarity on axial ligand affinity without significant interference from substituent electronic effects. The tetraalkyl porphyrin series can be divided into four classes according to whether the alkyl substituent is a methyl group or a primary, secondary, or tertiary alkyl group.

[redacted]

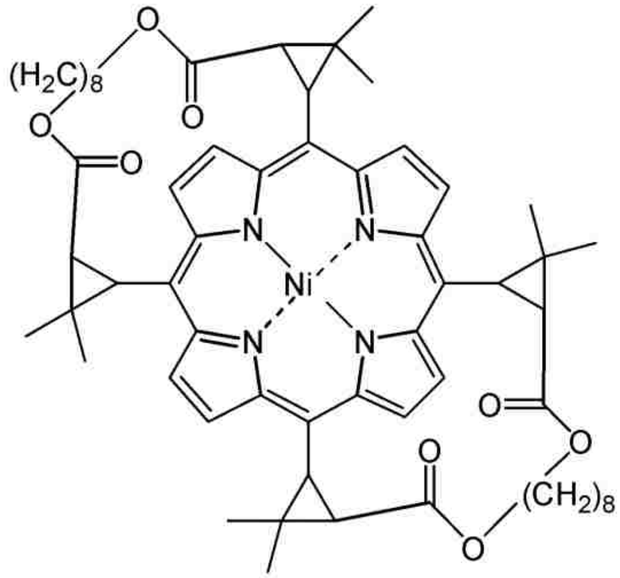

NiBCP-8

Figure 4.1 Structures of the nickel tetraalkylporphyrins and bridled chiroporphyrin discussed in this chapter.

The MM calculations show that the porphyrins in the series typically have four distinct stable conformers resulting from different positions of the peripheral alkyl substituents relative to the porphyrin mean plane (αβαβ, αααβ, αααα, and ααββ, with α and β indicating that the first substituent carbon atom is displaced above or below the mean plane, respectively). Some of the porphyrins (NiT(Et)P, NiT(Pr)P, and NiT(Pe)P) also possess additional secondary conformers resulting from variations in the orientation of the second carbon of the alkyl substituent. These secondary conformers have nearly the same calculated energies and macrocycle distortions (Table B-1 to Table B-3). The relative energies of the energy-minimized structures for each of the alkyl group orientations (αβαβ, αααβ, αααα, and ααββ) of the low-spin 4-coordinate nickel(II) complexes are shown in Table 4.1, and full details of the calculated energies are given in Table B-1.

The MM calculations find the structures with the lowest calculated energy have an αβαβ substituent orientation (Table 4.1) and a ruffled conformation of the porphyrin macrocycle (Table 4.2). The next higher energy conformer is predicted to be greater than 6 kcal-mol^{-1} above the αβαβ conformer (Table 4.1), suggesting that these other conformers are inaccessible at ambient temperatures. This is understandable because the αβαβ substituent orientation induces ruffling, which most effectively relieves the peripheral steric repulsions and also contracts the porphyrin core to provide a short and favorable Ni-N bond distance. A more pronounced difference in the energies of the αβαβ conformer and the others is observed for the bulkier substituents.

For comparison to the calculated structures, we examined some published crystal structures available for many of the compounds in the series as well as similar compounds. Selected structural parameters for these compounds are given in Table 4.4 and NSD analyses are provided in Table 4.5. In agreement with the lowest-energy calculated (MM) structures, most crystal structures show an αβαβ substituent orientation and a ruffled conformation of the porphyrin macrocycle. The crystal structures do contain small amounts of other distortions that most likely arise from crystal packing forces, especially packing forces that dictate special substituent orientations.

The structures of NiT(Pr)P and NiT(Pe)P demonstrate the great influence of crystal packing forces in determining the porphyrin conformation in some crystals. As the NSD analyses (Table 4.5) of the structures show, NiT(Pr)P is almost planar (d_{obs} = 0.173 Å, d_{ruf} = 0.001 Å) whereas the similar porphyrin NiT(Pe)P is ruffled (d_{ruf} = 1.6 Å). Interestingly, the NSD analyses show that the almost planar crystal structures of NiT(Pr)P and NiT(Me)P actually contain waving deformations that, although small, correspond to a considerable amount of deformation energy.[85,86] The structures of NiT(Me)P and NiT(Pr)P also show a long metal-nitrogen distance (Table 4.4) which is not optimal for coordination to low-spin nickel(II). These results suggest that the structures seen for NiT(Pr)P and NiT(Me)P are the result of favorable crystal packing interactions for non-optimum macrocycle conformations. This implies that the planar conformation is energetically accessible. Similar crystal packing influences result in both ruffled and planar crystalline forms of the reference compound NiOEP.

The conformational heterogeneity and influence of crystal packing forces apparent for the porphyrins with primary alkyl substituents are not seen for the porphyrins which have the bulkier secondary alkyl substituents (cPr, iPr, cH, 1-Et-Pr). All four crystal structures are very ruffled (d_{obs} 2.07-2.26 Å), have short Ni-N distances (1.888-1.902 Å), large ruffling angles (43.7-49.0°) and large π-overlap angles (12.1-13.8°) (Table 4.4 and Table 4.5). Only a limited amount of structural data was available for the tertiary alkyl-substituted porphyrin NiT(tBu)P, but the short Ni-N distance indicates that it is more nonplanar than the nickel porphyrins with secondary alkyl substituents.

For the calculated (MM) lowest-energy structures, the NSD results (Table 4.2) indicate that the degree of ruffling generally increases with the steric bulkiness of the peripheral alkyl substituent and varies between approximately 1.8 and 2.7 Å. The minimum energy αβαβ ruffled structures calculated for NiT(Me)P and the porphyrins with primary alkyl substituents ($\boldsymbol{d_{ruf}}$ 1.8-1.9 Å) are similar to the conformations seen crystallographically for NiT(Pe)P and NiT(2-Me-Pr)P ($\boldsymbol{d_{ruf}}$ 1.6-1.9 Å, Table 4.5). This confirms that the nearly planar crystal structures of NiT(Pr)P and NiT(Me)P (Table 4.5) may be the result of more favorable crystal packing interactions for the planar geometry. Overall, the MM calculations suggest that degree of ruffling increases in the series Et ~ Pr ~ Pe < Me ~ cPr < iPr ~ cH < tBu. The predictions that NiT(Me)P is more nonplanar than the other porphyrins with primary alkyl groups and that NiT(cPr)P is less nonplanar than the other porphyrins with secondary alkyl substituents are further supported by the spectroscopic studies below.

Table 4.3 presents selected structural parameters from the MM calculations, and additional structural parameters are given in Table B-3. The MM calculations are in good agreement with the crystal structures (Table 4.4), except in the cases where crystal packing forces are dominant as mentioned above. For example, the Ni-N distances in the porphyrins with secondary alkyl substituents are in the ranges of 1.881-1.904 Å (calculated) and 1.888-1.902 Å (crystal) and the C_α-N-N-C_α ruffling angles are 38.3-46.8° (calculated) and 43.7-46.2° (crystal); the N-C_α-C_m-C_α (π-overlap) torsion angle, however, is systematically overestimated. The Ni-N distance, a measure of the contraction of the porphyrin core, decreases as the porphyrin becomes more ruffled. The C_α-N-N-C_α torsion angle (sometimes called the “ruffling” angle), measuring the extent to which the planes of opposing pyrrole rings are twisted by ruffling of the porphyrin ring, increases as the amount of deformation increases. The N-C_α-C_m-C_α torsion angle, as shown in the last chapter, characterizes the degree of π-overlap between the pyrrole rings and correlates well with spectroscopic markers of porphyrin nonplanarity (red shifting of UV/visible absorption bands).

Table 4.1. Energies (in kcal-mol^{-1}) of stable conformers for different alkyl group orientations of the 4-coordinate low-spin nickel tetraalkylporphyrins relative to the lowest energy αβαβ conformers.

Porphyrin	*αβαβ*	*ααββ*	*αααβ*	*αααα*
NiT(Me)P	0	7.93	a	8.14
Primary alkyl groups				
NiT(Et)P	0	6.15	a	6.15
NiT(Pr)P	0	6.35	a	6.36
NiT(Pe)P	0	6.25	a	6.24
Secondary alkyl groups				
NiT(cPr)P	0	7.99	4.44	8.02
NiT(iPr)P	0	13.30	a	13.75
NiT(cH)P	0	14.17	a	14.85
Tertiary alkyl groups				
NiT(tBu)P	0	21.90	11.87	19.54

[a] No stable conformation was obtained.

Table 4.2. Out-of-plane displacements (in Å) for calculated αβαβ conformers of the 4-coordinate low-spin nickel tetraalkylporphyrins from normal-coordinate structural decomposition.

Porphyrin	***Total Distortion***		***B_{2u}***[c]	***B_{1u}***
	d_{obs}[a]	d_{calc}[b]	d_{sad}	d_{ruf}
NiT(Me)P	1.892	1.885	0.000	1.885
NiT(Et)P	1.812	1.808	0.000	1.808
NiT(Pr)P	1.799	1.795	0.000	1.795
NiT(Pe)P	1.797	1.793	0.000	1.793
NiT(cPr)P	1.857	1.850	0.000	1.850
NiT(iPr)P	2.245	2.236	0.099	2.233
NiT(cH)P	2.281	2.271	-0.102	2.269
NiT(tBu)P	2.764	2.743	0.000	2.743
NiTPP	1.482	1.479	0.005	1.479

[a] Total out-of-plane deformation calculated using all 21 out-of-plane modes.

[b] Total out-of-plane deformation calculated using the 6 lowest-energy out-of-plane modes.

[c] Deformation in the lowest-frequency mode of each symmetry type. The $E_g(x)$, $E_g(y)$, A_{1u}, and A_{2u} contributions are 0.000 and are not shown.

Table 4.3. Selected structural parameters for 4-coordinate low-spin nickel tetraalkylporphyrin molecular mechanics structures (αβαβ conformation).

Porphyrin	*Ni-N (Å)*	*C_α-N-N-C_α (°)* *(Ruffling angle)*	*N-C_α-C_m-C_α (°)* *(π-overlap angle)*
NiT(Me)P	1.902	39.1	17.9
	Primary alkyl groups		
NiT(Et)P	1.908	37.4	16.2
NiT(Pr)P	1.908	37.1	16
NiT(Pe)P	1.908	37.1	16.0
	Secondary alkyl groups		
NiT(cPr)P	1.904	38.3	17.9
NiT(iPr)P	1.883	46.1	22.3
NiT(cH)P	1.881	46.8	22.7
	Tertiary alkyl groups		
NiT(tBu)P	1.845	56.6	31.2
	Reference Compounds		
NiTPP	1.924	30.7	12.7

Table 4.4. Selected structural parameters from 4-coordinate low-spin nickel tetraalkylporphyrin X-ray crystal structures.

Porphyrin	*Ni-N (Å)*	*C_α-N-N-C_α (°) (Ruffling angle)*	*N-C_α-C_m-C_α (°) (π-overlap angle)*
NiT(Me)P (TCLNIB01)[76]	1.953	0.9	3.6
Primary alkyl groups			
NiT(Pe)P[a] [61]	1.922	34.1	8.0
NiT(Pe)P[b] [61]	1.925	33.2	8.6
NiT(Pr)P [61]	1.963	1.0	1.9
NiT(2-Me-Pr)P[c] (DOWCAT)[87]	1.908	40.3	10.3
Secondary alkyl groups			
NiT(cPr)P [61]	1.902	44.6	12.1
NiT(iPr)P (HETDAL)[88]	1.896	43.7	12.6
NiT(cH)P (ZULMOI)[86]	1.888	46.2	13.8
NiT(1-Et-Pr) (DOWDUO)[87]	1.889	49.0	13.2
Tertiary alkyl groups			
NiT(tBu)P[89]	1.869	n/a	n/a
Reference compounds			
NiP	1.951	1.6	0.8
NiTPP	1.931	27.3	7.5
NiOEP triclinic A	1.958	1.4	0.7
NiOEP triclinic B	1.952	0.8	2.1
NiOEP tetragonal	1.930	31.9	7.8

[a] Data is taken from the structure of NiT(Pe)P crystallized from dichloromethane by slow diffusion of methanol. Structural parameters are for one of four molecules with similar macrocycle conformations (molecule analyzed contains atom Ni4 and has the least disorder of the pentyl groups).

[b] Data is taken from the structure of NiT(Pe)P crystallized by slow evaporation of a solution in piperidine.

[c] Data is for one of two molecules with similar macrocycle conformations (molecule analyzed contains Ni1).

Table 4.5. Out-of-plane displacements (in Å) for the crystal structures of the 4-coordinate low-spin nickel tetraalkylporphyrins from normal-coordinate structural decomposition.

Porphyrin	***Total Distortion***		B_{2u}[c]	B_{1u}	A_{2u}	E_g(x)	E_g(y)	A_{1u}
	d_{obs}[a]	d_{calc}[b]	d_{sad}	d_{ruf}	d_{dom}	$d_{wav(x)}$	$d_{wav(y)}$	d_{pro}
NiT(Me)P[76]	0.296	0.273	0.000	0.000	0.001	0.268	0.050	0.000
NiT(Pe)P[d] [61]	1.644	1.643	0.462	1.572	0.106	0.055	0.041	0.013
NiT(Pe)P[e] [61]	1.657	1.656	0.572	1.552	0.067	0.056	0.040	0.007
NiT(Pr)P [61]	0.173	0.164	0.000	0.001	0.000	0.164	0.017	0.000
NiT(2-Me-Pr)[f] [87]	1.900	1.898	0.342	1.859	0.039	0.125	0.114	0.016
NiT(cPr)P [61]	2.073	2.072	0.000	2.069	0.095	0.020	0.020	0.000
NiT(iPr)P [88]	2.085	2.084	0.458	2.029	0.025	0.082	0.096	0.025
NiT(cH)P [86]	2.143	2.141	0.143	2.137	0.003	0.002	0.002	0.006
NiT(1-Et-Pr)P [87]	2.257	2.256	0.000	2.254	0.000	0.000	0.091	0.003
Reference Compounds								
NiTPP	1.295	1.292	0.256	1.266	0.000	0.000	0.000	0.001
NiOEP tetragonal	1.461	1.461	0.116	1.456	0.000	0.000	0.000	0.000
NiOEP triclinic A	0.087	0.078	0.000	0.000	0.000	0.072	0.031	0.000
NiOEP triclinic B	0.144	0.135	0.000	0.000	0.000	0.066	0.117	0.000
NiP	0.094	0.087	0.013	0.079	0.006	0.033	0.003	0.004

[a] Total out-of-plane deformation calculated using all 21 out-of-plane modes.

[b] Total out-of-plane deformation calculated using the 6 lowest-energy out-of-plane modes.

[c] Deformation in the lowest-frequency mode of each symmetry type.

[d] Data is taken from the structure of NiT(Pe)P crystallized from dichloromethane by slow diffusion of methanol. Structural parameters are for one of four molecules with similar macrocycle conformations (molecule analyzed contains atom Ni4 and has the least disorder of the pentyl groups).

[e] Data is taken from the structure of NiT(Pe)P crystallized by slow evaporation of a solution in piperidine.

[f] Data is for one of two molecules with similar macrocycle conformations (molecule analyzed contains Ni1).

4.5 Spectroscopic Studies of Axial Ligation to Nickel Tetraalkylporphyrins

UV-vis (absorption) and Raman (vibrational) spectroscopies were used to examine the relation of the noted structural trends in the nickel tetraalkylporphyrin series to their affinity towards binding axial ligands.

4.5.1 UV-visible Absorption Spectroscopy

Previous spectroscopic studies of NiTPP have shown that shifts in the absorption spectra accompany axial coordination,[80,90-94] so UV-visible absorption spectra of the nickel tetraalkylporphyrin series with varying degrees of ruffling were taken in both non-coordinating and coordinating solvents, with spectral shifts between the two indicative of the occurrence of axial ligation.

The UV-visible absorption spectra of the nickel tetraalkylporphyrins in the non-coordinating solvent dichloromethane are shown in Figure 4.2. The spectra are similar to those observed previously in CS_2,[85] except for blue shifts of about 10 nm for the B and Q_0 bands and 5 nm for the Q_v band. The latter solvent shifts are likely the result of the differences in the dipole moments of CH_2Cl_2 (dielectric constant of 9.08) and CS_2 (2.64). The B and Q bands of the $\pi-\pi^*$ transitions of the porphyrin ring progressively red shift and broaden as the substituent group becomes more bulky. This red shift, as discussed in the last chapter, is mostly attributed to nonplanar distortions of the porphyrin macrocycle.

In accord, the new spectrum of NiT(cPr)P shows bands approximately at the positions expected on the basis of its degree of ruffling and π overlap angle, providing further confidence in this conclusion. (Note that the compounds NiCPOEt and NiBCP-8 are presented here with the tetraalkyls but will be discussed later in Section 4.8)

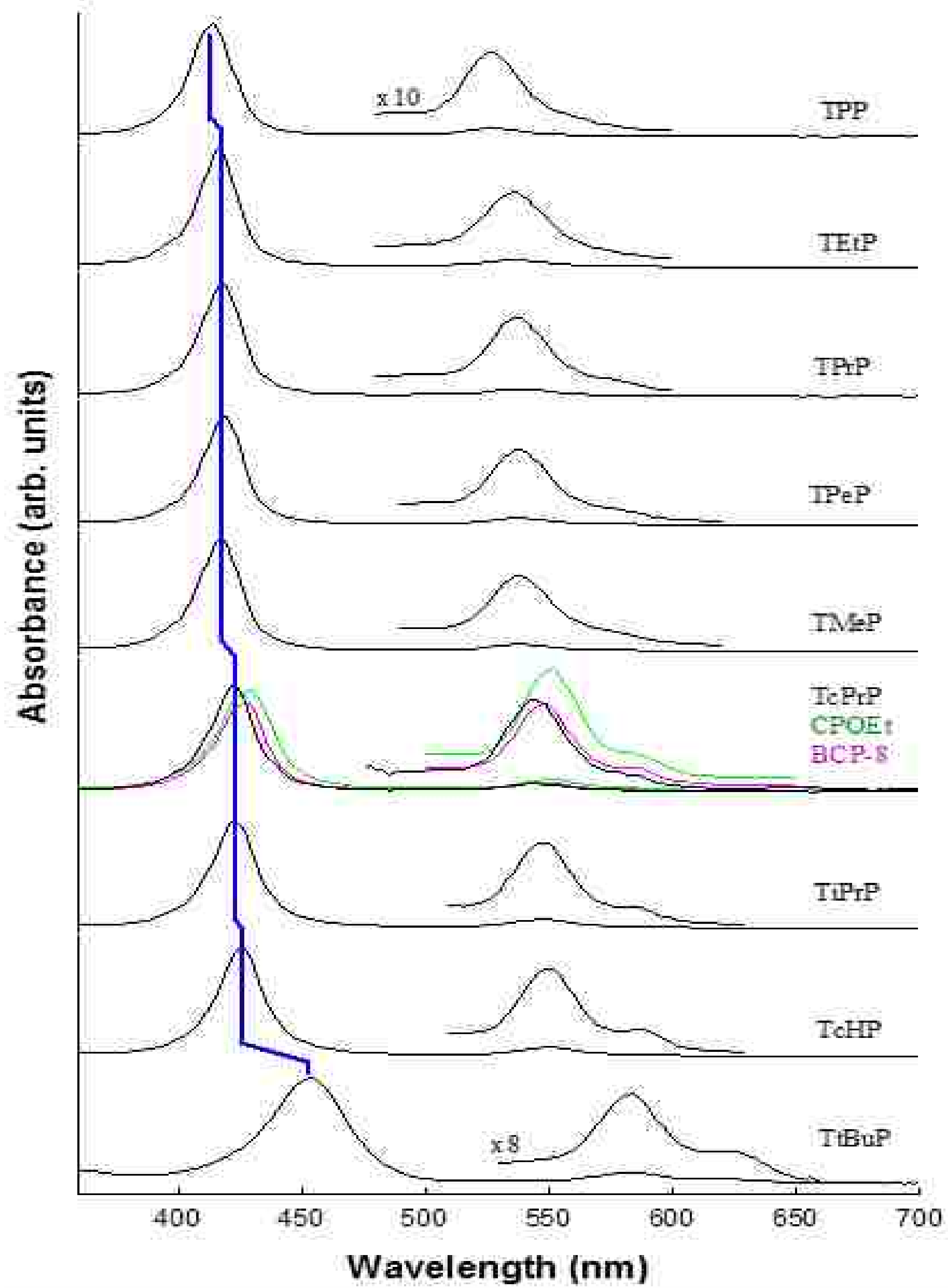

Figure 4.2. UV-visible absorption spectra for the nickel tetraalkylporphyrins in the non-coordinating solvent dichloromethane.

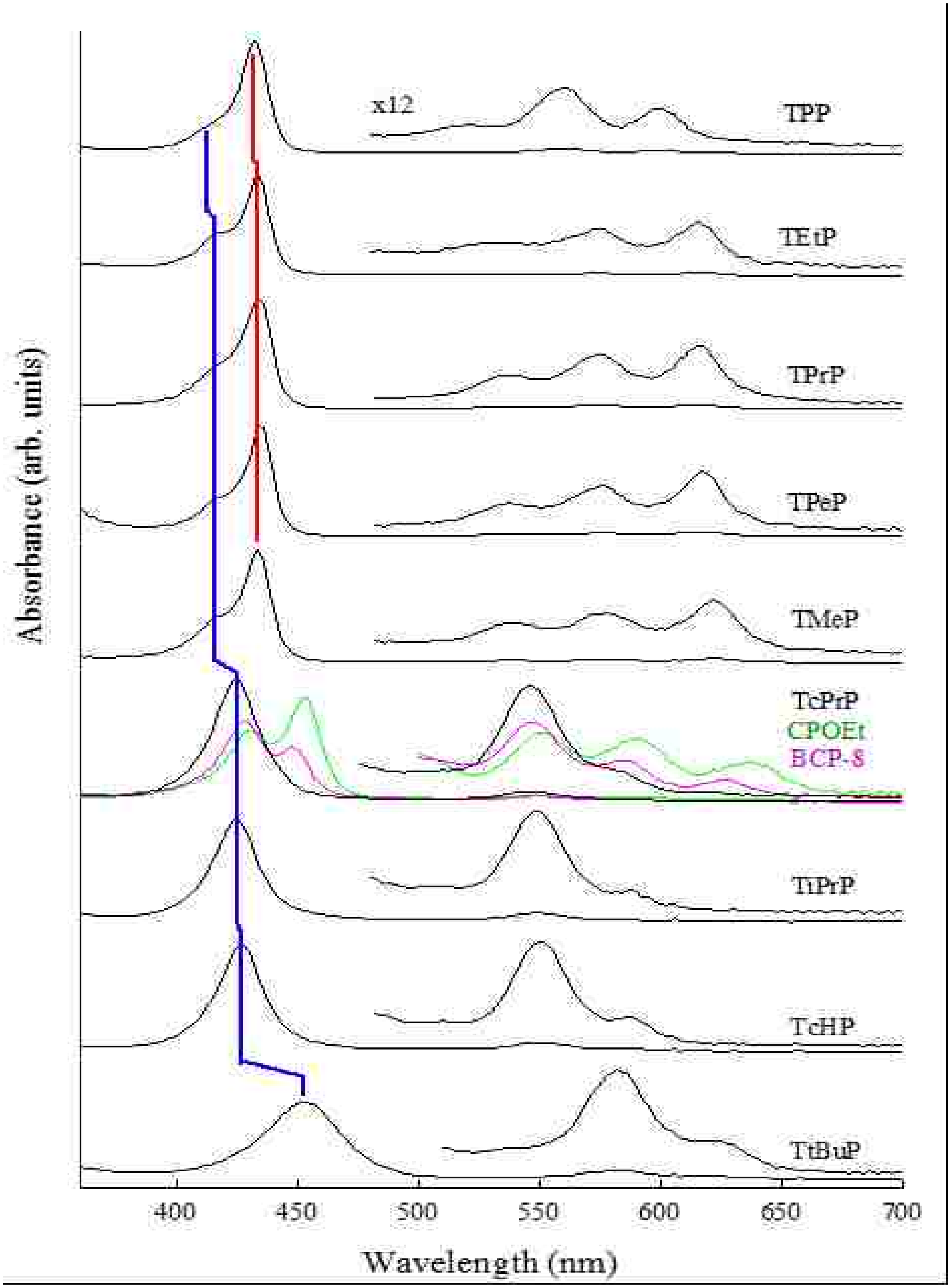

Figure 4.3. UV-visible absorption spectra for the nickel tetraalkylporphyrins in the strongly coordinating solvent pyrrolidine. Soret bands for the unligated forms are marked with a blue line; those for the ligated forms with a red line. Q band region magnified for clarity.

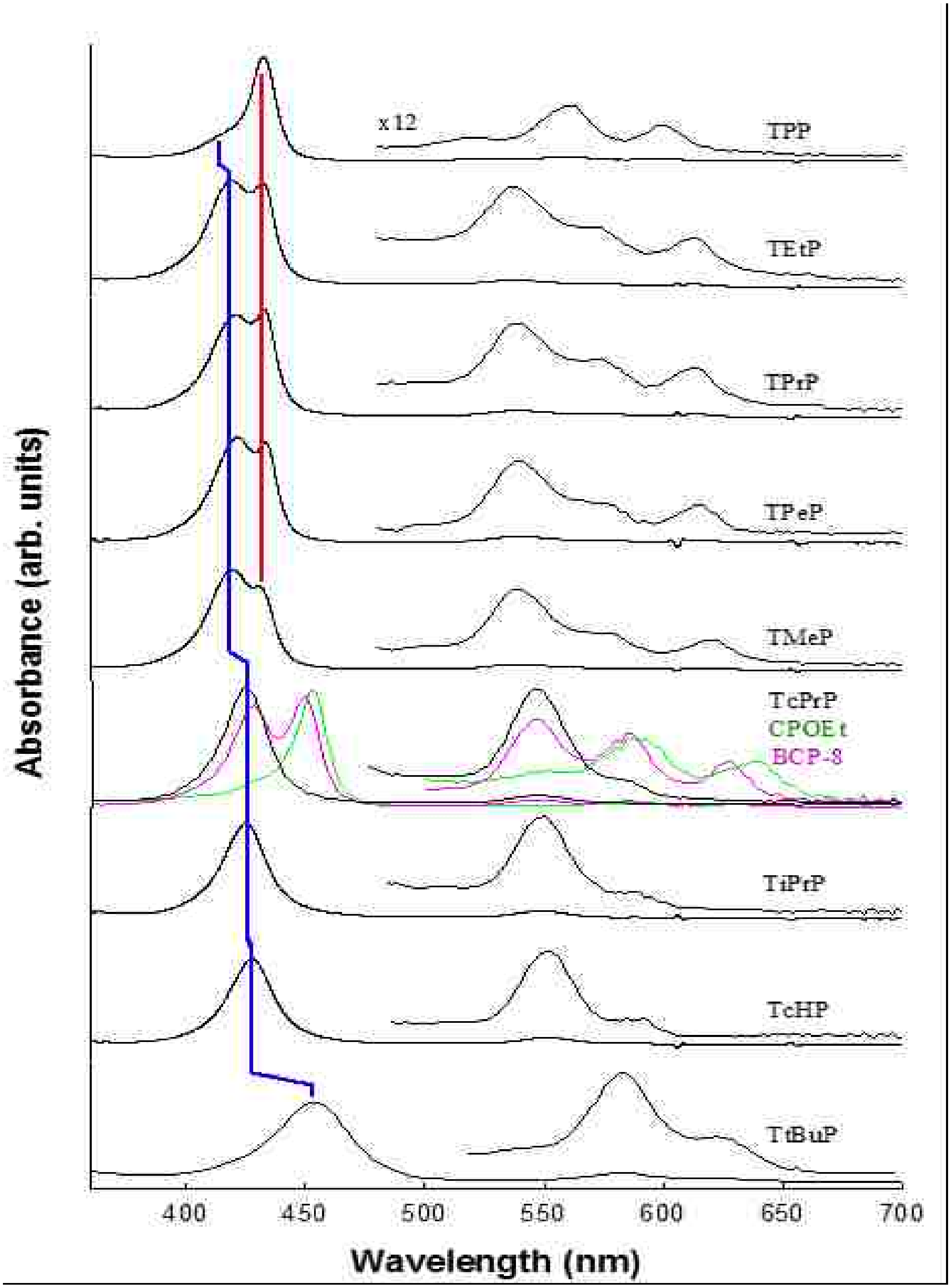

Figure 4.4. UV-visible absorption spectra for the nickel tetraalkylporphyrins in the strongly coordinating solvent piperidine. Soret bands for the unligated forms are marked with a blue line; those for the ligated forms with a red line. Q band region magnified for clarity.

Table 4.6. Absorption Maxima (nm) for the nickel tetraalkylporphyrins in dichloromethane or pyrrolidine.

Porphyrin	**B** **CH_2Cl_2**	**B** **Pyr**	**Δ**	**Q_v** **CH_2Cl_2**	**Q_v** **Pyr**	**Δ**	**Q_o** **CH_2Cl_2**	**Q_o** **Pyr**	**Δ**
NiTPP	413.8	433.8	20.0	526.6	561.5	34.9	563	602.5	51.7
NiT(Et)P	416.7	433.6	16.9	536.0	574.4	38.4	573	615.1	51.6
NiT(Pr)P	417.6	433.9	16.3	537.6	574.5	36.9	574	615.8	48.9
NiT(Pe)P	418.4	434.8	16.4	538.0	575.6	37.6	578	616.9	49.3
NiT(Me)P	417.2	433.7	16.5	537.8	578.0	40.2	575	622.1	58.2
NiT(cPr)P	423.1	440.1*	17.0	544.3	586.1*	41.8	581.7	621.9*	40.2
NiT(iPr)P	424.4	424.6	0.2	549.6	549.3	0.3	588.0	588.6	0.6
NiT(cH)P	425.4	427.1	1.7	550.3	551.6	1.3	586.7	588.3	1.6
NiT(tBu)P	452.9	453.1	0.2	583.3	581.8	1.5	624.2	621.5	2.7

* Absorption maxima for the axially ligated species measured in azetidine.

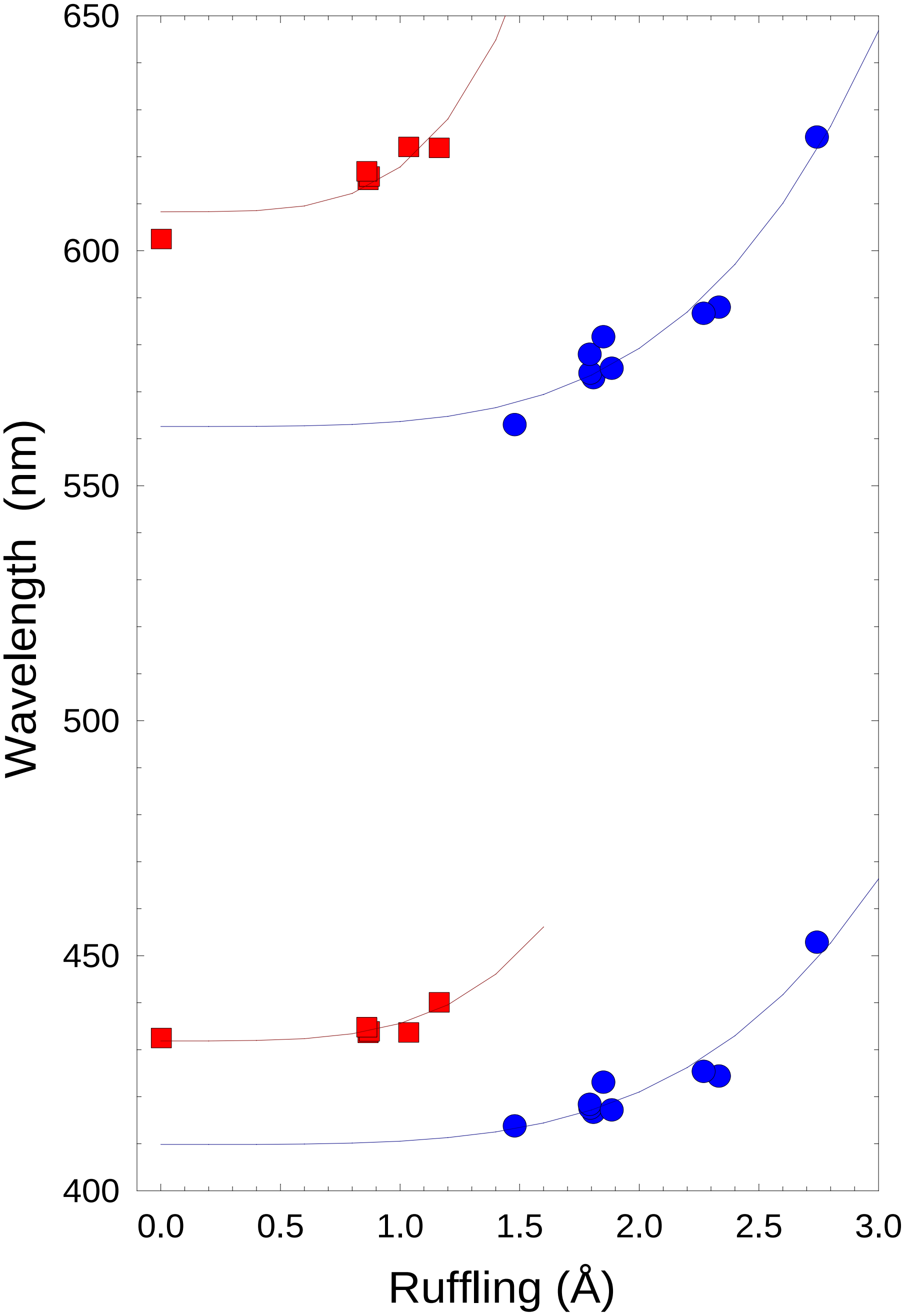

Figure 4.5. Observed 4-coordinate (blue) and 6-coordinate (red) absorption maxima (nm) for nickel tetraalkylporphyrins and their pyrrolidine complexes *versus* ruffling of the corresponding calculated structures. Curve fits are with a homogeneous quartic equation. The azetidine complex is substituted for NiT(cPr)P, and the reference NiTPP complexes are also included. The data is listed in Table 4.6.

Figure 4.3 & Figure 4.4 show the absorption spectra obtained in the strongly coordinating solvents pyrrolidine and piperidine, respectively, and the absorption maxima therein are listed in Table 4.6 and plotted versus the simulated ruffling (taken from Table 4.2) in Figure 4.5. For the less distorted porphyrins with methyl or primary alkyl substituents, there is an approximately 15-nm red shift of the B band for the pyrrolidine complexes compared to the B band of the 4-coordinate species (Figure 4.3). A red shift is also observed for the Q_v band (~ 40 nm) and the Q_0 band (~ 50-60 nm). Similarly, in piperidine the Soret bands for both the 4-coordinate and 6-coordinate species are observed for several of the less nonplanar tetraalkylporphyrins (Figure 4.4). For the more highly ruffled complexes with secondary alkyl (NiT(cPr)P, NiT(iPr)P, NiT(cH)P) or tertiary alkyl (NiT(tBu)P) groups, the absorption spectra in pyrrolidine or piperidine are nearly the same as those seen in dichloromethane indicating that the complexes remain 4-coordinate. This data suggests that flatter porphyrin macrocycles favor ligand binding while more ruffled macrocycles hinder it.

In addition to the presence or absence of the ligated species, we examined the relation of non-planarity to the ratio of the ligated to unligated forms for the primary alkyls where the two forms co-existed. Based on the height ratios of the (fitted) peaks for the ligated to unligated species, the proportion of the ligated species in piperidine (Figure 4.4) decreases in the order NiT(Et)P (0.70) ~ NiT(Pr)P (0.72) ~ NiT(Pe)P (0.67) > NiT(Me)P (0.48). The finding of lower proportion of the ligated species for methyl than for the other primary alkyls fits well with the notion that nonplanarity lowers ligand affinity, as the MM calculations (Table 4.2) show d_{ruf} ~ 1.9 Å for NiT(Me)P compared to

d_{ruf} ~ 1.8 Å for NiT(Et)P, NiT(Pr)P and NiT(Pe)P, further confirming that the non-planar deformation in the 4-coordinate low-spin state inhibits binding. Also, among the secondary alkyls, the fact that NiT(cPr) (d_{ruf} ~ 1.9 Å) adds axial ligands in azetidine (Figure B-1) whereas NiT(iPr)P or NiT(cH)P (d_{ruf} ~ 2.2-2.3 Å) do not likewise agrees with the less distorted structure calculated by MM for NiT(cPr)P.

It is worth noting that a red shift is consistently seen upon axial ligation even though the switch to the larger high-spin nickel is expected to flatten the macrocycle and therefore, according to purely conformational aspects as described in the last chapter, produce a blue shift in the optical spectra. In actuality, this blue shift is probably small because the ruffling changes here occur in the flatter part of the curve, so the much larger red-shift arising from the electronic change at the nickel ion associated with axial ligation is the dominant effect.

4.5.2 Resonance Raman Spectroscopy

In addition to studying the relationship between ligation and structure using the optical spectra that probe the electronic structure of the porphyrins, Resonance Raman spectroscopy, which probes the vibrational states, may also be utilized as the Raman core-size and oxidation-state marker lines ν_2, ν_3, ν_4, ν_{10}, and ν_{28} are good structural and ligation state indicators.[20,68,83,85,95-99] For example, Soret-excited resonance Raman spectra of the nickel tetraalkylporphyrins in the non-coordinating solvent CS_2 show a decrease in the frequencies of the structure-sensitive lines ν_2, ν_3, ν_4, and ν_{28} with an increase in nonplanarity caused by bulky *meso* substituents.[85] A similar decrease in these marker line frequencies with increasing magnitude of nonplanarity has been noted in other series of porphyrins,[20] confirming the establishment of a correlation between frequency and nonplanarity in porphyrins.[100]

Figure 4.6 shows Resonance Raman spectra of the nickel tetraalkylporphyrin series in both the coordinating solvent pyrrolidine and the non-coordinating solvent dichloromethane in the high-frequency region (1300-1700 cm^{-1}). This region contains the well-known structure-sensitive lines, including the oxidation-state marker line ν_4 and the core-size marker lines ν_2 and ν_3.[20,82,101] Assignment of the ν_2 and ν_4 lines was aided by analyzing the spectra during titrations to different pyrrolidine concentrations (performed by group member Dr. Y. Song) as shown in Figure B-2; ν_3 unfortunately could not be assigned because it is weak and overlies a strong broad line from the pyrrolidine solvent in the ligated form.

The approximate positions of some unligated porphyrin vibrational peaks are indicated by the blue lines in Figure 4.6 and Figure B-2. The structure-sensitive lines ν_2 and ν_4 downshift in coordinating pyrrolidine solvent by up to ~25 cm^{-1} relative to those of the corresponding spectra in dichloromethane, corresponding to the large red shift in the UV-vis absorption bands. The large downshifts in these core-size marker lines are indicative of axial coordination, which induces an expansion of the porphyrin core.[18,90,98,99,102] For the highly nonplanar Ni tetraalkylporphyrins, the Raman spectra of the pyrrolidine complexes are almost the same as those seen in dichloromethane. This confirms that these porphyrins do not form observable amounts of axially ligated species, in agreement with the findings from the UV-visible spectroscopy experiments. On the other hand, for the less distorted methyl and primary alkyl substituted tetraalkylporphyrins, the lines for the ligated species (indicated by the * symbol) dominate the Raman spectra whereas the corresponding absorption spectra indicate a more balanced equilibrium between ligated and unligated species. This could be due to the spectrum of the ligated species being stronger as a result of enhanced resonance of its transition with the laser excitation at 413.1 nm.

In a previous paper by our group, it was shown that distinct ν_4 lines could be observed not only for 4- and 6-coordinate forms of NiTPP, but also for the 5-coordinate (mono-ligated) form, with the 5-coordinate ν_4 located at an intermediate frequency between the 4- and 6-coordinate values.[80] In Figure 4.6 and Figure B-2, only two ν_4 lines are observed, one of which is the 4-coordinate form, such that only one ligated species is formed, either 5- or 6-coordinate. Whilst the absorption and Raman spectra show that axial ligation goes almost to completion for the methyl and primary alkyl porphyrins in pyrrolidine, it is not conclusively determined by this spectroscopic data whether the ligated species is 5- or 6-coordinate. In titration experiments performed by a group member Dr. Y. Song,[61] an intermediate UV-vis peak was detected representative of a 5-coordinate species. In the nickel tetraalkylporphyrins that bind pyrrolidine, the dominant ligated species is the 6-coordinate complex by far (maximum concentration of 5-coordinate species less than 1% for NiT(Me)P), though the 5-coordinate complex was easier to detect in the reference compound NiTPP (~10%). The scarcity of the 5-coordinate species is consistent with the manifestation of a single ligated form in the resonance Raman spectra. The cause of the scarcity of the mono-ligated form will be considered in the computational studies below.

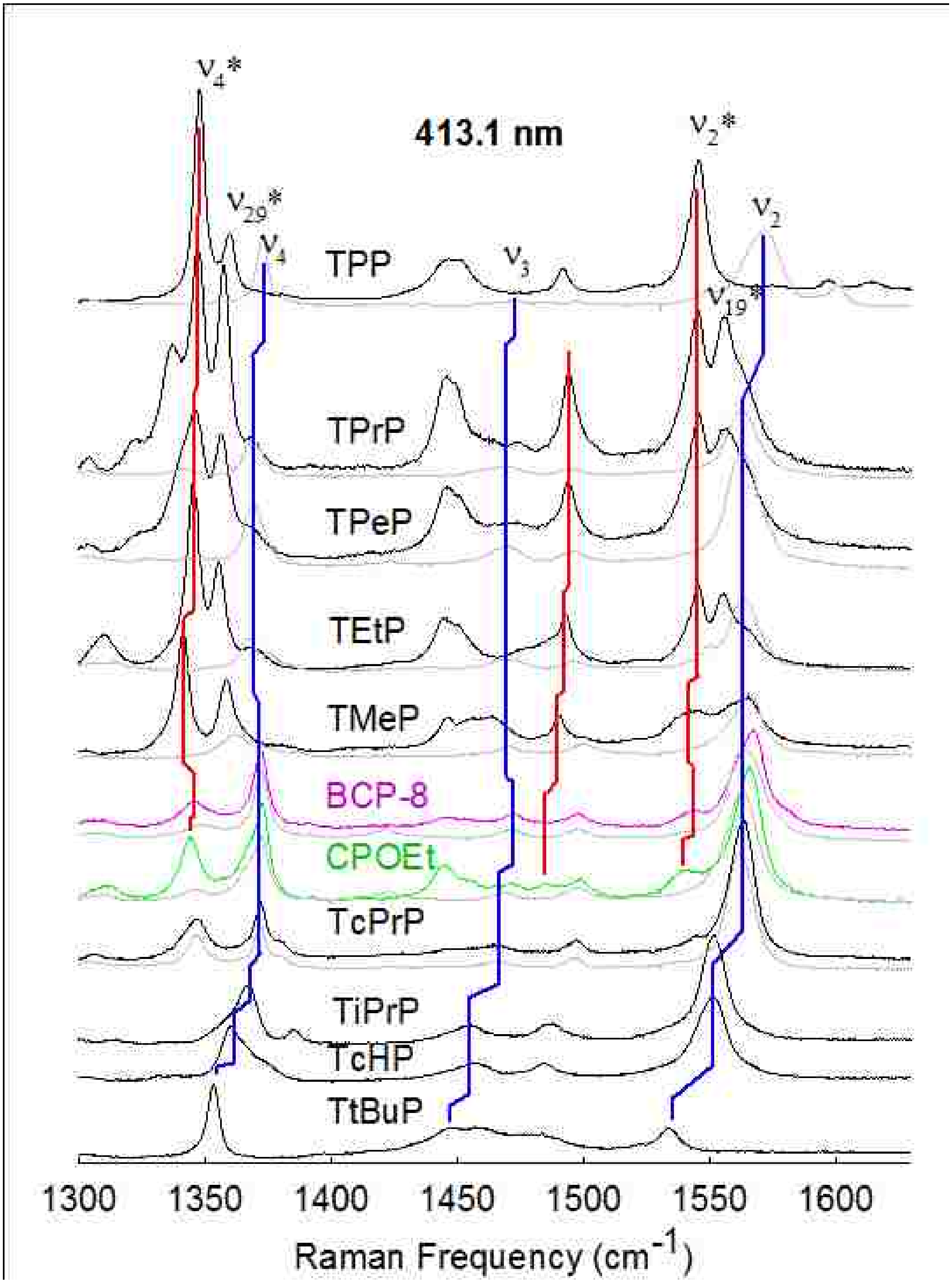

Figure 4.6. Resonance Raman spectra of the nickel tetraalkylporphyrins in pyrrolidine at 413.1 nm excitation (* indicates axially ligated form). Spectra obtained in dichloromethane are shown with gray lines.

4.6 Computational Studies of Axial Ligation to Nickel Tetraalkylporphyrins

Having examined axial ligation to the nickel tetraalkylporphyrins spectroscopically in conjunction with calculations of their unligated forms, molecular simulations of the ligated forms are now used to investigate the factors contributing to the observed trends.

4.6.1 Conformational Energetics of the Axially Ligated Complexes

MM calculations were performed on the nickel tetraalkylporphyrin series with pyrrolidine axial ligands bonded to the metal core, having either a single ligand (mono-ligated, 5-coordinate) or two on opposite faces (bis-ligated, 6-coordinate). Furthermore, the molecules were also simulated in the high spin 4-coordinate form; that is to say, without axial ligands but with the nickel atom in its enlarged “high spin” state. Such a state represents a molecule whose nickel atom is converted to high spin by photo-excitation of an electron rather than chemically, allowing another avenue for switchable molecular devices. Besides the possibility of photo-excitation, this state is useful in the theoretical sense to distinguish structural changes induced by enlargement of the core metal ion from those induced by steric interactions with a particular axial ligand.

As was done for the unligated (low spin 4-coordinate) porphyrins, here energies were calculated for the structural conformers resulting from different positions of the peripheral alkyl substituents relative to the porphyrin mean plane: αβαβ, ααββ, αααβ, and αααα, where α and β indicate that the first substituent carbon atom is displaced above or below the mean plane, respectively. Probing the conformers is not only important for finding the global minimum energy, but may also be useful for molecular devices as mentioned in the introduction. Examining the conformational energy landscape in the various “stages” of ligation informs us of the barriers that must be surmounted in order to trigger a conformational switch in such devices.

Full details of the calculated energies for the high-spin 4-coordinate complexes (representing the photoexcited state), high-spin 5-coordinate (mono-pyrrolidine) complexes, and high-spin 6-coordinate (bis-pyrrolidine) complexes of the nickel tetraalkylporphyrins are provided in Table B-4, Table B-5, and Table B-6, respectively, and the results for the 4- and 6-coordinate forms are summarized in Table 4.7. The calculations indicate that the αβαβ ruffled structure is still the lowest energy conformation, but the energy differences between the conformations are now smaller. For example, for low-spin 4-coordinate NiTMP (Table 4.1), the conformer next lowest in energy is 7.93 kcal-mol^{-1} above αβαβ, whilst for high-spin 4-coordinate NiTMP (Table 4.7) the difference is only 0.83 kcal-mol^{-1}. This suggests that additional macrocycle conformations are accessible in solution at room temperature for the high-spin ligated complexes. This can be understood by considering the relationship between conformation and core size; the αβαβ ruffled conformation produces a small core size, whereas larger core sizes are obtained from the out-of-plane deformations produced with other substituent orientations.[68] The latter are more compatible with the larger high-spin nickel ion of the axial ligand complexes. Hence, the switch to high-spin nickel alters the conformational energy landscape by destabilizing the ruffled conformation and stabilizing the other conformations.

It is important to bear in mind that these MM energies are conformational energies and omit the electronic energy of ligand binding and the entropic contributions to the free energy, thus they address only the conformational aspects of the energetics of complexation. Predictions based on these energies assume that other contributions are equal for a particular axial ligand.

Table 4.7. Energies (in kcal-mol^{-1}) for different alkyl group orientations of the high-spin nickel tetraalkylporphyrins relative to the lowest energy αβαβ conformer.

Porphyrin	*αβαβ*	*ααββ*	*αααβ*	*αααα*
NiT(Me)P 4-coordinate (d-d excited state)	0	1.30	0.83	1.18
6-coordinate (bis-pyrrolidine)	0[a]	1.48[b]	1.11[b]	1.38[b]
Primary alkyl groups				
NiT(Et)P 4-coordinate	0	1.18	0.74	1.07
6-coordinate	0[a]	0.51[b]	0.34[b]	0.52[b]
NiT(Pr)P 4-coordinate	0	1.30	0.83	1.18
6-coordinate	0[a]	0.57[b]	0.40[b]	0.59[b]
NiT(Pe)P 4-coordinate	0	1.27	0.80	1.14
6-coordinate	0[a]	0.54[b]	0.48[b]	0.56[b]
Secondary alkyl groups				
NiT(cPr)P 4-coordinate	0	2.44	1.50	1.70
6-coordinate	0[a]	2.51	1.79[a]	2.09[b]
NiT(iPr)P 4-coordinate	0	4.83	[d]	4.08
6-coordinate	0[a]	6.81[c]	[d]	4.27[b]
NiT(cH)P 4-coordinate	0	5.36	[d]	4.48
6-coordinate	0[a]	4.67[b]	[d]	5.06[b]
Tertiary alkyl groups				
NiT(tBu)P 4-coordinate	0	8.80	3.32	2.03
6-coordinate	0[a]	8.01[a]	2.62[a]	3.66[b]

[a] With the N-H bonds of the ligands sitting between the $\text{Ni-N}_{\text{pyrrole}}$ bonds and the mean planes of the axial ligands perpendicular to each other.

[b] With the N-H bonds of the ligands sitting along the $\text{Ni-N}_{\text{pyrrole}}$ bonds and the mean planes of the axial ligands perpendicular to each other.

[c] With the N-H bonds of the ligands sitting along the $\text{Ni-N}_{\text{pyrrole}}$ bonds and the mean planes of the axial ligands parallel to each other.

[d] No stable conformation observed.

4.6.2 Structures of the Axially Ligated Complexes

As was done for the unligated (4-coordinate) porphyrin series, published X-ray crystal structures for ligated molecules were analyzed by NSD and are presented for comparison with the following computational results. Table 4.8 summarizes some available crystal data for 6-coordinate complexes along with the corresponding 4-coordinate analogs. Axial ligation and the associated switch to high-spin nickel(II) significantly increases the Ni-$N_{pyrrole}$ distance (by about 0.12 Å or 6 %). The replacement of the small low-spin nickel atom with the much larger high-spin nickel atom flattens the nonplanar porphyrin macrocycles; for example, the crystal structure of NiTPP is moderately ruffled[103] but becomes nearly planar upon complexation with nitrogenous base ligands such as piperidine or 1-methyl-imidazole.[80,104] Sterically crowded nickel tetrabromo-tetracyano-tetraphenylporphyrin ($NiBr_4(CN)_4TPP$, Figure B-3) is very saddled but flattens upon ligation with pyridine[73] as does nickel octaethyl-tetranitroporphyrin (NiOETNP).[72]

Table 4.8. NSD analyses comparing the X-ray crystal structures[61] of low-spin 4-coordinate nickel porphyrins and their high-spin 6-coordinate complexes (displacements in Å).

Porphyrin	*Ni-N_{pyr} (Å)*	*Total Distortion*		B_{2u}[c]	B_{1u}	A_{2u}	E_g(x)	E_g(y)	A_{1u}
		d_{obs}[a]	d_{calc}[b]	d_{sad}	d_{ruf}	d_{dom}	$d_{wav(x)}$	$d_{wav(y)}$	d_{pro}
NiTPP	1.931	1.295	1.292	0.256	1.266	0.000	0.000	0.000	0.001
NiTPP (pip)$_2$	2.043	0.341	0.259	0.000	0.000	0.000	0.144	0.215	0.000
NiTPP (1-Me-Im)$_2$	2.052	0.362	0.314	0.000	0.000	0.000	0.118	0.292	0.000
NiBr$_4$(CN)$_4$TPP	1.919	3.080	3.077	3.068	0.205	0.090	0.050	0.017	0.034
NiBr$_4$(CN)$_4$TPP (py)$_2$	2.056	1.951	1.937	1.867	0.489	0.000	0.073	0.142	0.034
NiOETNP (molec 1)	1.917	3.313	3.310	3.250	0.632	0.011	0.091	0.048	0.041
NiOETNP (molec 2)	1.921	3.010	3.009	2.877	0.874	0.064	0.042	0.055	0.077
NiOETNP (py)$_2$	2.049	2.483	2.460	2.306	0.844	0.052	0.124	0.054	0.058

[a] Total out-of-plane deformation calculated using all 21 out-of-plane modes.

[b] Total out-of-plane deformation calculated using the 6 lowest-energy out-of-plane modes.

[c] Deformation in the lowest-frequency mode of each symmetry type.

Table 4.9. NSD analyses of the calculated lowest energy αβαβ conformers of the high-spin nickel tetraalkylporphyrins (displacements in Å).

Porphyrin	Total Distortion		B_{2u}[c]	B_{1u}	A_{2u}	$E_g(x)$	$E_g(y)$
	d_{obs}[a]	d_{calc}[b]	d_{sad}	d_{ruf}	d_{dom}	$d_{wav(x)}$	$d_{wav(y)}$
NiT(Me)P 4-coord.	1.093	1.085	0.000	1.085	0.000	0.000	0.000
6-coord.[d]	1.045	1.036	0.000	1.036	0.000	0.016	0.000
NiT(Et)P 4-coord.	0.921	0.915	0.000	0.915	0.000	0.000	0.000
6-coord.[d]	0.873	0.867	0.024	0.866	0.000	0.000	0.013
NiT(Pr)P 4-coord.	0.918	0.912	0.000	0.912	0.000	0.000	0.000
6-coord.[d]	0.879	0.873	0.042	0.872	0.000	0.002	0.013
NiT(Pe)P 4-coord.	0.929	0.923	0.000	0.923	0.000	0.000	0.000
6-coord.[d]	0.867	0.861	0.011	0.861	0.000	0.000	-0.012
NiT(cPr)P 4-coord.	1.168	1.158	0.000	1.158	0.000	0.000	0.001
6-coord.[d]	1.176	1.164	0.000	1.164	0.000	0.000	0.016
NiT(iPr)P 4-coord.	1.590	1.576	0.117	1.572	0.000	0.000	0.000
6-coord.[d]	1.512	1.495	0.007	1.495	0.000	0.007	0.023
NiT(cH)P 4-coord.	1.655	1.640	0.083	1.638	0.000	0.000	0.000
6-coord.[d]	1.585	1.567	0.033	1.567	0.001	0.021	0.022
NiT(tBu)P 4-coord.	2.281	2.250	0.000	2.250	0.000	0.000	0.000
6-coord.[d]	1.869	1.824	0.135	1.819	0.001	0.021	0.022
NiTPP 4-coord.	0.018	0.018	0.000	0.018	0.000	0.000	0.000
6-coord.[d]	0.401	0.400	0.055	0.396	0.000	0.003	0.017

[a] Total out-of-plane deformation (in Å) calculated using all 21 out-of-plane modes.

[b] Total out-of-plane deformation (in Å) calculated using the 6 lowest-energy out-of-plane modes.

[c] Deformation in the lowest-frequency mode of each symmetry type (the A_{1u} mode is generally insignificant and is not shown).

[d] With the N-H bonds of the ligands sitting between the Ni-$N_{pyrrole}$ bonds (45°) and the mean planes of the axial ligands perpendicular to each other.

From the MM calculations, the lowest energy αβαβ 4-coordinate high-spin and 6-coordinate high-spin structures are analyzed by NSD and the results are summarized in Table 4.9, with a complete listing in Table B-7 to Table B-9. Selected structural parameters are presented in Table B-10 to Table B-12. The Ni-$N_{pyrrole}$ distances for the high-spin 4-coordinate complexes (1.966-2.028 Å) are markedly longer than those seen for the low-spin complexes (1.845-1.908 Å) and increase a little further upon ligation to form the 6-coordinate complex (1.982-2.031 Å). Concomitant with this increase in the Ni-$N_{pyrrole}$ distance there is a decrease in macrocycle ruffling, with d_{ruf} going from 1.79-2.74 Å (4-coordinate low-spin) to 0.91-2.25 Å (4-coordinate high-spin) to 0.86-1.82 Å (6-coordinate high-spin). Small amounts of the other nonplanar deformation modes are also seen in the axially ligated complexes (Table 4.9) most likely due to the asymmetry of the axial ligands and/or the asymmetry induced by the orientations of the ligands. The similarity in the structures of the bis-ligated (6-coordinate) and high-spin 4-coordinate high-spin complexes suggests that direct interaction between the axial ligand and the substituent groups is a minor effect, with the possible exception of the *tert*-butyl substituents.

As illustrated in Figure 4.7, the percentage decrease in ruffling upon switching from low- to high-spin 4-coordinate nickel varies markedly with the alkyl substituent: for methyl and primary alkyl substituents 42-49%; for secondary alkyl groups 28-30%; and for the tert-butyl group 18%. The smaller changes apparent for the bulkier alkyl groups are consistent with the approximately quadratic dependence of the energy required to deform the porphyrin macrocycle,[82] reminiscent of the non-linear dependence of electronic transition energies on the ruffling deformations (Figure 4.5). For the porphyrins with methyl or primary alkyl substituents, which are less ruffled, the energy that is required to cause a large change in nonplanar deformation (arising from the change in the equilibrium Ni-N bond distance for low and high spin Ni) is small because the structures are on the shallow portion of the potential energy surface. In contrast, the porphyrins with secondary and tertiary substituents are located on the steeper portion of the potential energy curve and thus smaller amounts of flattening can be induced by the switch to high-spin Ni.

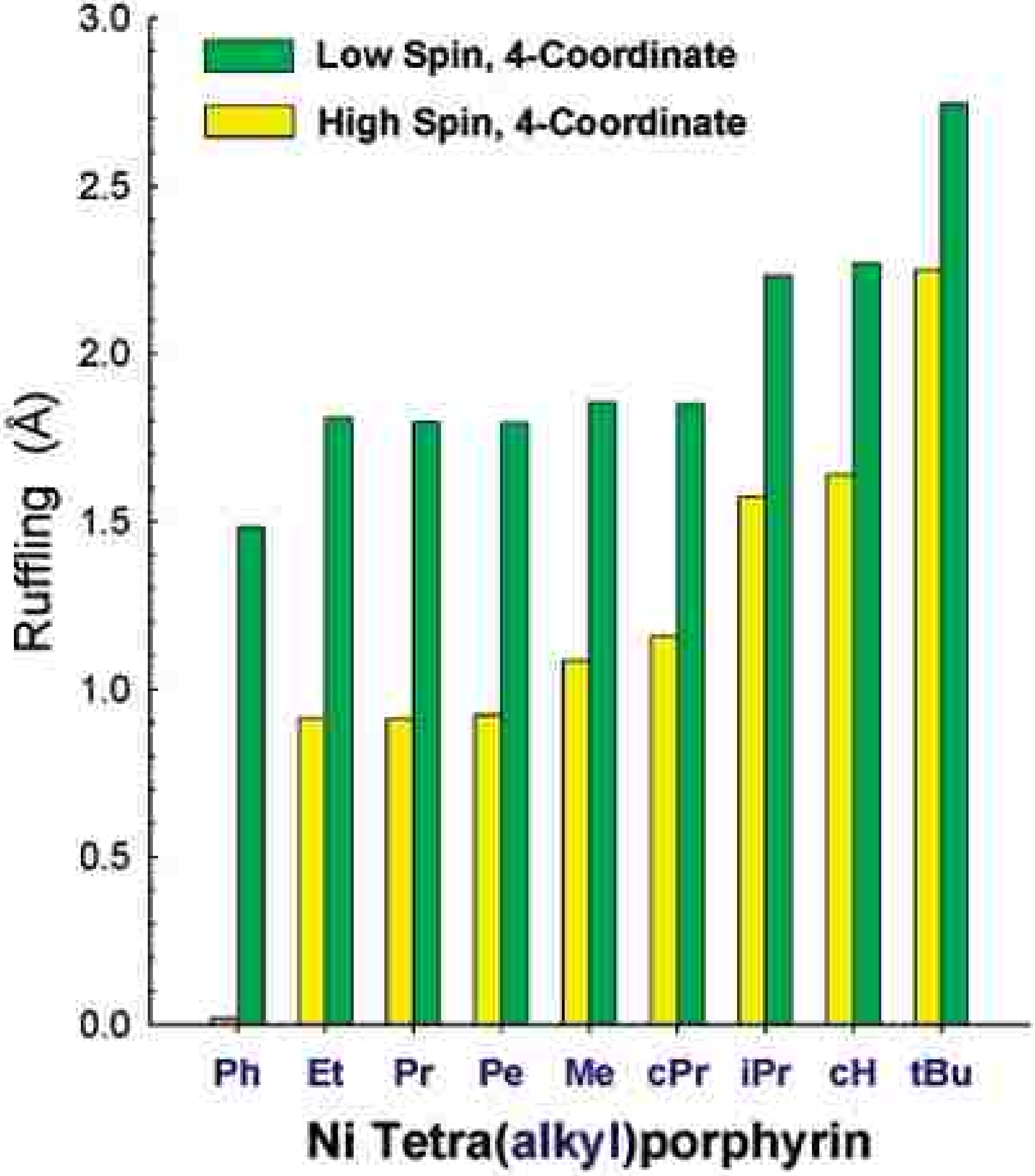

Figure 4.7. Ruffling deformations (in Å) for the nickel tetraalkylporphyrins from the NSD analysis of the low-spin (green) and high-spin (yellow) four-coordinate MM structures.

4.6.3 Conformational Contributions to Ligand Binding Energies

The finding of a significant decrease in axial ligand affinity with an increase in the size of the alkyl substituent and the degree of macrocycle nonplanarity can be viewed in terms of two energy components. One is a "conformational effect" related to the nonplanar conformation of the low-spin complex and the energy associated with changing the conformation of the macrocycle to accommodate the larger high-spin nickel(II) ion. An analogous energy penalty would be present for any porphyrin constrained into a nonplanar conformation, *i.e.,* for a porphyrin constrained into a nonplanar conformation by a protein matrix or other external scaffold there would also be a related energy associated with changing the porphyrin conformation. The other is a "steric effect" due to interactions between the ligand and the substituents on the porphyrin ring or the surface of the porphyrin ring (these interactions might in theory also be attractive). The analogous situation in a protein system would be crowding around the active site of the enzyme which controls the access of substrate molecules. This raises the question of the extent to which inhibition of ligand binding in the nickel tetraalkylporphyrins is related to a conformational effect versus a steric effect in the tetraalkylporphyrins.

The correlation between ligand binding affinity and nonplanarity seen in the optical studies of NiT(Me)P vs. NiT(Et)P, NiT(Pr)P and NiT(Pe)P or, alternatively, NiT(cPr) vs. NiT(iPr)P and NiT(cH)P, suggests that the dominant effect on axial ligand binding is conformational rather than steric (with the possible exception of NiT(tBu)P), as was confirmed by the MM calculations. The energies obtained from the MM calculations were used to estimate the conformational part of the ligand binding energies. Approximate binding energies for the addition of pyrrolidine were calculated by subtracting the energy of the pyrrolidine ligand(s) and the lowest-energy 4-coordinate conformer from the energies of the 5- or 6-coordinate pyrrolidine complexes (Table 4.10 and Figure 4.8). These binding energies are only the structural contribution to the binding free energy, omitting entropic and electronic enthalpic contributions associated with ligand binding. In particular, the entropic component associated with bringing together two or three molecules at room temperature is not included in the calculations and will likely shift the calculated binding energies to more positive (less favorable) values. Nonetheless, the entropic contributions (and to some extent the electronic) are likely similar across the range of compounds studied, thus the MM calculations provide a reasonable estimate of the trend in energetic preference of these distorted porphyrins for binding axial ligands. The MM calculations (Figure 4.8) correctly reproduce the trends seen in the spectroscopic studies (Figure 4.3, Figure 4.4, and Figure 4.6). Negative binding energies are typically obtained for the methyl and primary alkyl substituted porphyrins and the reference compound NiTPP; the binding energies become more positive for the porphyrins containing secondary alkyl substituents and more so for tertiary, such that the binding energy calculated for NiT(tBu)P is large and ligand binding is strongly disfavored.

The MM calculations underscore the fact that the major effect causing the observed decrease in ligand binding affinity is the switch from low- to high-spin 4-coordinate nickel (see Table 4.10). The energy increase from low- to high-spin 4-coordinate nickel is small (0.56 kcal-mol^{-1}) for NiT(Me)P but large (13.56 kcal-mol^{-1}) for

NiT(tBu)P. This energy is associated with the inability of the porphyrin to flatten and the core to expand to accommodate the large Ni-N bond of high-spin Ni for the more ruffled porphyrins. As observed above, for the bulkier substituents, the macrocycle cannot flatten enough to allow the core to expand sufficiently to accept the larger Ni ion (Figure 4.7). The energy increases associated with the addition of pyrrolidine ligands are similar for both porphyrins: -3.03 kcal-mol^{-1} (5-coordinate) and -2.10 kcal-mol^{-1} (6-coordinate) for NiT(Me)P, compared to -4.38 and -2.40 kcal-mol^{-1} for NiT(tBu)P, respectively (see Table 4.10).

Table 4.10. Calculated binding energies and energy differences for nickel tetraalkylporphyrin complexes (kcal mol^{-1})

Porphyrin	d_{ruf} (LS, 4-c)	$\Delta E^{5}_{binding}$ [a] αβαβ	$\Delta E^{6}_{binding}$ [b] αβαβ	Spin-state change[c]	1st Ligation[d]	2nd Ligation[e]
NiTPP	1.479	-9.47	-12.33	-5.32	-4.15	-2.86
NiT(Et)P	1.808	-4.80	-7.64	-0.94	-3.86	-2.84
NiT(Pr)P	1.795	-4.81	-7.75	-0.84	-3.97	-2.94
NiT(Pe)P	1.793	-5.10	-6.95	-0.92	-4.18	-1.85
NiT(cPr)P	1.850	-4.04	-7.58	0.59	-4.63	-3.54
NiT(Me)P	1.885	-2.47	-4.57	0.56	-3.03	-2.10
NiT(iPr)P	2.233	+0.08	-3.24	4.53	-3.92	-3.32
NiT(cH)P	2.269	+0.38	-3.20	5.19	-4.81	-3.58
NiT(tBu)P	2.743	+9.18	+6.78	13.56	-4.38	-2.40

[a] $\Delta E^{5}_{binding} = E^{\alpha\beta\alpha\beta}_{5c} - (E^{\alpha\beta\alpha\beta}_{4cls} + E_{pyrrolidine})$.

[b] $\Delta E^{6}_{binding} = E^{\alpha\beta\alpha\beta}_{6c} - (E^{\alpha\beta\alpha\beta}_{4cls} + 2xE_{pyrrolidine})$.

[c] $E^{\alpha\beta\alpha\beta}_{4chs} - E^{\alpha\beta\alpha\beta}_{4cls}$.

[d] $E^{\alpha\beta\alpha\beta}_{5c} - (E^{\alpha\beta\alpha\beta}_{4chs} + E_{pyrrolidine})$.

[e] $E^{\alpha\beta\alpha\beta}_{6c} - (E^{\alpha\beta\alpha\beta}_{5c} + E_{pyrrolidine})$. ($E_{pyrrolidine}$ = 9.97 kcal/mol).

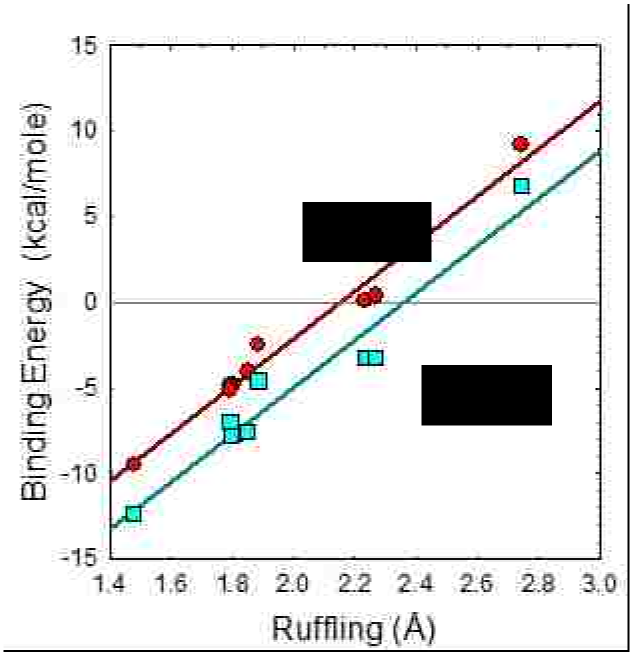

[redacted]

[redacted]

Figure 4.8. Calculated conformational binding energies for nickel tetraalkylporphyrins for the 5-coordinate ($\Delta E^{5}_{binding}$) and 6-coordinate ($\Delta E^{6}_{binding}$) complexes with pyrrolidine *versus* ruffling of the 4-coordinate low-spin form. $\Delta E^{5}_{binding} = E^{\alpha\beta\alpha\beta}_{5c} - (E^{\alpha\beta\alpha\beta}_{4c,ls} + E_{pyrrolidine})$; $\Delta E^{6}_{binding} = E^{\alpha\beta\alpha\beta}_{6c} - (E^{\alpha\beta\alpha\beta}_{4c,ls} + 2 \times E_{pyrrolidine})$.

4.7 Implications and Potential Uses of the Ligation-induced Structural Changes

All together, molecular simulations, Resonance Raman and UV-visible spectroscopy, X-ray crystal structures, and normal-coordinate structural decomposition analysis indicate that the axial ligand affinity within the series of nickel tetraalkylporphyrins depends strongly on the degree of macrocycle ruffling, which is in turn determined by the bulkiness of the *meso* substituents. Specifically, the ligand affinity decreases markedly as the alkyl group becomes larger and the amount of ruffling in the 4-coordinate form increases. MM calculations show that this decrease in ligand affinity is related to how readily the substituents permit the ring to flatten to accommodate the high-spin nickel ion and not to direct steric inhibition of ligand binding by the substituents.

Spectroscopic titration studies[61] have shown that the decrease in axial ligand affinity occurs primarily because of a large decrease in the binding affinity for the first ligand which induces the nickel spin-state change and flattening of the porphyrin ring. The decrease in the first axial ligand binding affinity compared to NiTPP is large (10^{-2} to 10^{-3}) even for porphyrins with methyl or primary alkyl substituents. When binding the second axial ligand, only a small portion of the energy of ligand binding goes into additional small structural changes so that the net binding energy is much higher, giving binding constants for the methyl or primary alkyl substituted porphyrins that are similar to those seen for Ni porphyrins for which nearly planar conformers are accessible at room temperature (*e.g.*, NiTPP and NiOEP). In contrast, for very bulky substituents such as *tert*-butyl, accessing high-spin nickel is energetically prohibitive and this effectively inhibits axial ligation.

Expansion of the nickel ion, either by axial ligation or by formation of the photoexcited Ni (*d,d*) state, causes a significant change in the relative energies of the porphyrin conformations (αβαβ, ααββ, αααβ and αααα); while an αβαβ (ruffled) conformer is strongly favored for the low-spin 4-coordinate species, the MM calculations indicate a narrowing of the energy differences between the conformers when the nickel ion is expanded. This finding is consistent with a previous experimental study[70] on the Ni *d-d* excited state of NiT(tBu)P with time-resolved absorption spectroscopy, which indicated a transient switch from the αβαβ ground-state conformation in the ground state to a different conformer in the excited high-spin state (unligated) complex; the conformer in the excited (d,d) state is most likely αααβ or αααα, as these favor a large core.

4.8 Design of a Switchable Molecular Device: NanoTweezer

In this section, the insights gained from the structural and spectroscopic studies of axial ligation and spin-state change in the nickel tetraalkylporphyrins are applied to the use of nickel porphyrins as mechanical molecular devices. The significant conformational change resulting from the expansion or contraction of the nickel ion was investigated in the bridled chiroporphyrin NiBCP-8 (see Figure 4.1) in order to overcome the limitations of simple tetraalkylporphyrins. The nickel complex NiBCP-8, as mentioned in the previous chapter (Section 3.8), adopts an αβαβ conformation (the four cyclopropyl group substituents are alternately displaced toward opposite faces of the macrocycle, i.e., the same ruffled conformation seen for the tetraalkylporphyrins) whereas the analogous complex with the much larger zinc(II) core (ZnBCP-8) adopts αααα stereochemistry instead (all four substituents on the same side of a nearly planar macrocycle, such that the straps fold together).[59-61] Given that high-spin nickel(II) is also a large ion-- it is the same size as Zn(II) in our force field[67]--, it is reasonable to suppose that high-spin NiBCP-8 would behave like the zinc(II) complex. A novel prototype nanotweezer could thus be designed where large-scale structural changes are induced by switching the state of the core nickel ion from low spin to high spin; in other words, addition of axial ligands or absorption of a photon will actuate and close the NiBCP-8 nanotweezers as illustrated in Figure 4.9.

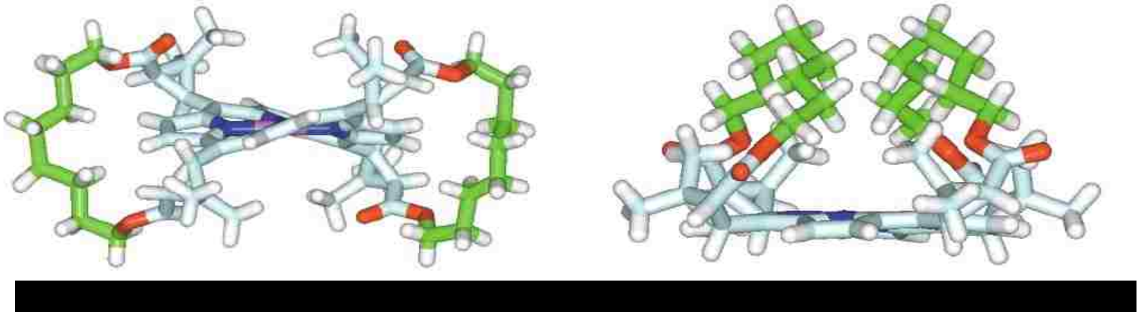

Figure 4.9 The open (left) and closed (right) forms of a prototype nanotweezer based on the bridled chiroporphyrin BCP-8. The structures were generated using published crystallographic data[105] for the low-spin nickel(II) complex (left) and the zinc(II) complex (right) of BCP-8.

The NiBCP-8 system was studied computationally and spectroscopically in a manner similar to the tetraalkyl series, and compared to that series in its propensity to bind ligands, particularly its "parent" alkyl, NiT(cPr)P. Since the substituents of the chiroporphyrin are not simple alkyls, an additional intermediate compound (NiT(cOEt)P) was also examined that has similar substituents to NiBCP-8 except, rather than methylene bridles connecting the substituents, the chains are truncated to ethyls. This compound can help to distinguish the substituent electronic effects from the conformational and steric effects imposed by the bridles. In the studies above on the tetraalkyl series, the dominant effect on axial ligand binding was found to be conformational rather than steric; sterics are likely to play a greater role for NiBCP-8 that the tetraalkylporphyrins, though, due to the long straps surrounding the ligation site. For the MM calculations, the high spin 4-coordinate form (without axial ligands but with the nickel atom in its enlarged “high spin” state) was simulated in addition to the unligated (low spin 4-coordinate) and ligated (6-coordinate) forms. Besides helping to distinguish structural changes induced by enlargement of the core metal ion from those induced by steric interactions with axial ligands, this state represents a molecule whose nickel atom is enlarged to high spin by photo-excitation of an electron rather than chemically, allowing another avenue for switchable molecular devices.

Molecular mechanics calculations were performed on NiBCP-8 and NiT(cOEt)P in their low spin, high spin 4-coordinate, and high spin 6-coordinate (bis-pyrrolidine) states, and for each the αβαβ and αααα conformers were compared. Ligand binding energies were calculated (as in Section 4.6.3) and were found to be negative (i.e., favoring binding) for both compounds, regardless of the conformer adopted for the ligated species. The relative energies of the αβαβ and αααα conformers are shown in Table 4.11 for these two compounds, together with the reference tetraalkyl compound NiT(cPr)P. The calculations fail to predict the preferred conformer for low spin NiBCP-8, favoring the αααα conformer over αβαβ, albeit only by a slight difference (-1.78 kcal/mol) so that a higher level calculation might produce better results. The calculations do, however, indicate that the αααα form is relatively much more stabilized for the high spin Ni (-10.01 kcal/mol) compared to low spin Ni (-1.78 kcal/mol). The steric impact of ligands on switching from αβαβ to αααα conformer was evaluated by comparing the high spin 4-coordinate and 6-coordinate forms; we find that, whereas the difference in steric interaction between the pyrrolidine ligands and substituents is minimal for NiT(cPr)P and NiT(cOEt)P (~ 1 kcal/mol), the interaction is much greater (~ 6 kcal/mol) with the bridles of NiBCP-8 in the αααα ("closed") conformer.

Table 4.11 Relative MM Energies (kcal/mol) of αααα and αβαβ Conformers of NiBCP8 and reference compounds.

Porphyrin	ΔE (αααα – αβαβ)		
	Low Spin 4-coord	High Spin 4-coord	High Spin 6-coord (bis-pyrrolidine)
NiT(cPr)P	8.02	1.70	2.45
NiT(cOEt)P	12.73	2.45	3.23
NiBCP-8	-1.78	-10.01	-4.27

The ruffling deformation calculated for NiBCP8 (obtained from averaging snapshot structures from multiple MD trajectories; see Section 3.8.2) was 1.93 Å (Table 3.8). This ranks it slightly higher than NiT(Me)P (d_{ruf} = 1.89 Å) which does bind axial ligands and lower than NiT(iPr)P (d_{ruf} = 2.23 Å) which doesn't (see Figure 4.3 for pyrrolidine & Figure 4.4 for piperidine). The values for both NiT(cOEt)P (d_{ruf} = 2.03 Å) and NiT(cPr)P (d_{ruf} = 1.85 Å) were not much different than NiBCP8. The UV-vis spectroscopic results for these compounds, together with the tetraalkyl series, are shown in Figure 4.2 (non-binding solvent dichloromethane), Figure 4.3 (binding solvent pyrrolidine), and Figure 4.4 (binding solvent piperidine).

The nickel bridled chiroporphyrin exhibits anomalously red-shifted UV-visible absorption bands for their calculated rufflings both for the four-coordinate species and the ligated species. In addition, the affinities for axial ligands indicated by the relative intensities of the two Soret bands in the spectra of NiBCP-8 and NiCPOEt in pyrrolidine (Figure 4.3) suggest that the chiroporphyrins lie between the methyl and isopropyl porphyrins. It is also noted that the presence of the bridles has a significant negative influence on the affinity. For piperidine (Figure 4.4), the relative amounts of four- and six-coordinate forms suggest again that the bridled chiroporphyrin should be between the methyl and isopropyl porphyrins on this basis. However, the affinity of the chiroporphyrin without the straps is actually close to NiTPP, which is fully six-coordinated in piperidine. The larger piperidine ligand is also favored by the chiroporphyrins, exhibiting considerably more of the six-coordinate form compared to pyrrolidine. The opposite coordination behavior is noted for these two ligands for the other nickel tetraalkylporphyrins, i.e., the affinity for piperidine is less than for pyrrolidine.

The resonance Raman spectra of the nickel chiroporphyrins also place these porphyrins near tetramethylporphyrin in terms of the frequencies of the structure-sensitive marker lines (Figure 4.6). For example, the frequencies of the four-coordinate ν_4 line of both chiroporphyrins are at almost the same and near the frequency of NiTMeP. Close examination shows that the marker line frequencies for the bridled porphyrin are slightly higher than for the chiroporphyrin without straps, consistent with a small decrease in nonplanarity noted in the last chapter. The resonance Raman spectra also corroborate the enhanced affinity for both chiroporphyrins for piperidine compared to pyrrolidine, and suggest that the ligand affinities of the chiroporphyrins places them between tetra(methyl)porphyrin, which binds pyrrolidine strongly, and tetra(isopropyl)porphyrin, which does not significantly bind pyrrolidine.

Besides the anomalous ligand affinities of the chiroporphyrin compared to the tetraalkylporphyrins in terms of the nonplanar distortion of the porphyrin macrocycle, the magnitude of the shifts in the UV-visible absorption and resonance Raman bands are also anomalous, implying a likely switch in conformer. In collusion with the x-ray crystal data for the chiroporphyrins, we conclude that the bridled chiroporphyrin undergoes a change from a ruffled four-coordinate conformer to a domed axially ligated conformer, thus forming a chemically activated molecular nanotweezers.

4.9 Conclusions & Implications

The spectroscopic studies, both UV-vis and Raman, showed that affinity of the nickel tetraalkyl porphyrins to axial ligands decreases with the bulk of the alkyl substituents. The MM calculations (Figure 4.8) correctly reproduce the trends seen in the spectroscopic studies (Figure 4.3, Figure 4.4, and Figure 4.6). Negative binding energies are typically obtained for the methyl and primary alkyl substituted porphyrins and the reference compound NiTPP; the binding energies become more positive for the porphyrins containing secondary alkyl substituents and more so for tertiary, such that the binding energy calculated for NiT(tBu)P is large and ligand binding is strongly disfavored.

The MM calculations underscore the fact that the major effect causing the observed decrease in ligand binding affinity is the switch from low- to high-spin 4-coordinate nickel. The energy increase from low- to high-spin 4-coordinate nickel is small (0.56 kcal-mol^{-1}) for NiT(Me)P but large (13.56 kcal-mol^{-1}) for NiT(tBu)P; this energy is associated with the inability of the porphyrin to flatten and the core to expand to accommodate the large Ni-N bond of high-spin Ni for the more ruffled porphyrins. For the bulkier substituents, the macrocycle cannot flatten enough to allow the core to expand sufficiently to accept the larger Ni ion.

The computational and spectroscopic studies of the NiBCP-8 system illustrated the utility of axial ligation as a mechanism for producing switchable molecular device. The study show that there is a tradeoff between providing the large distortion and large barriers to interconversion between conformers, which are desirable for an effective molecular machine, and insuring the ability to switch the machine between conformers by using axial ligation or a photoinduced excitation to actuate the nanodevice. The promising results suggest that molecular mechanics may aid in designing such nanodevices.

The relationship between porphyrin distortion and axial ligand affinity may also have implications in biology for enzymes such as methyl-coenzyme M reductase and, more generally, for the many hemoproteins and photosynthetic proteins which have their hemes and photosynthetic pigments in moderately nonplanar conformations maintained by the surrounding protein.[100,106,107] Nonplanar deformations are known to alter many biologically relevant properties such as redox potentials, electron transfer rates, photophysical processes.[89,100,108] The present study indicates that nonplanar deformations, in this case maintained by the *meso* alkyl substituents rather than by a protein matrix, also have an impact on axial ligation. Specifically, holding the tetrapyrrole macrocycle in a moderately nonplanar geometry provides a mechanism for adjusting the ligand affinity and, in particular, modulating the relative affinities of the fifth and sixth ligands. Although the nickel porphyrin studies are not directly applicable to axial ligation by iron porphyrins, they do suggest specific structural mechanisms that may influence the more complex electronic interactions involved in axial ligand binding to heme. In fact, it would not be surprising to find that nonplanar deformations also influence the axial coordination behavior of heme, especially given that investigations of strapped porphyrins[60,109] imply that nonplanar heme distortion might provide a mechanism for differentiating CO and O_2 binding, and a change in ruffling of the heme has been suggested as a mechanism for regulating NO affinity and reactivity in nitrophorins (NO-transport proteins).[110]

CHAPTER 5: INVESTIGATION OF PORPHYRINIC MOLECULAR ROTORS

5.1 Introduction

Advanced molecular rotors will likely be vital components in the machinery of nanotechnology. In a molecular rotor, one part of a molecule (or a whole molecule) rotates against the other part or against a rigid body such as a solid surface. While this definition could be applied to simple systems such as the two methyl groups in ethane, what is of technological interest is molecular rotors that can produce useful work, or molecular motors. These may be used, for example, to propel nanofluidics or form geared systems. Unidirectional rotation is often considered a prerequisite for a molecular motor.[111] Molecular rotors may be designed with a small potential energy barrier for rotation such that rotation occurs naturally above a certain temperature, or they may be designed so as to driven by an external force such as an electric field.

Porphyrins are an ideal platform for molecular rotors for several reasons. First, their unique electronic and chemical properties potentially allow several driving and switching mechanisms for rotation (photochemical, chemical, thermal). Second, along with the versatility provided by the multiple substituent positions, many synthetic techniques exist to tailor the molecules and fine-tune their structures and properties. Furthermore, in addition to having multiple sites for tethering or self-assembly onto surfaces, porphyrins can also form supra-molecular arrays or self-assemble into various nano-structures.[31] Although up to now most molecular rotors by far have been studied in solution,[111] rotors or rotor arrays mounted on surfaces or inside solids are of particular interest for future applications in nanoscience and nanotechnology.

To this end, this chapter examines the aryl rotational behavior in porphyrins and its relation to nonplanar distortions of the macrocycle. The shape of aryl groups is well suited for rotor applications such as nanopropellers or nanogears, and the choice or aryl affords further versatility in steric hindrance and electronic effects.

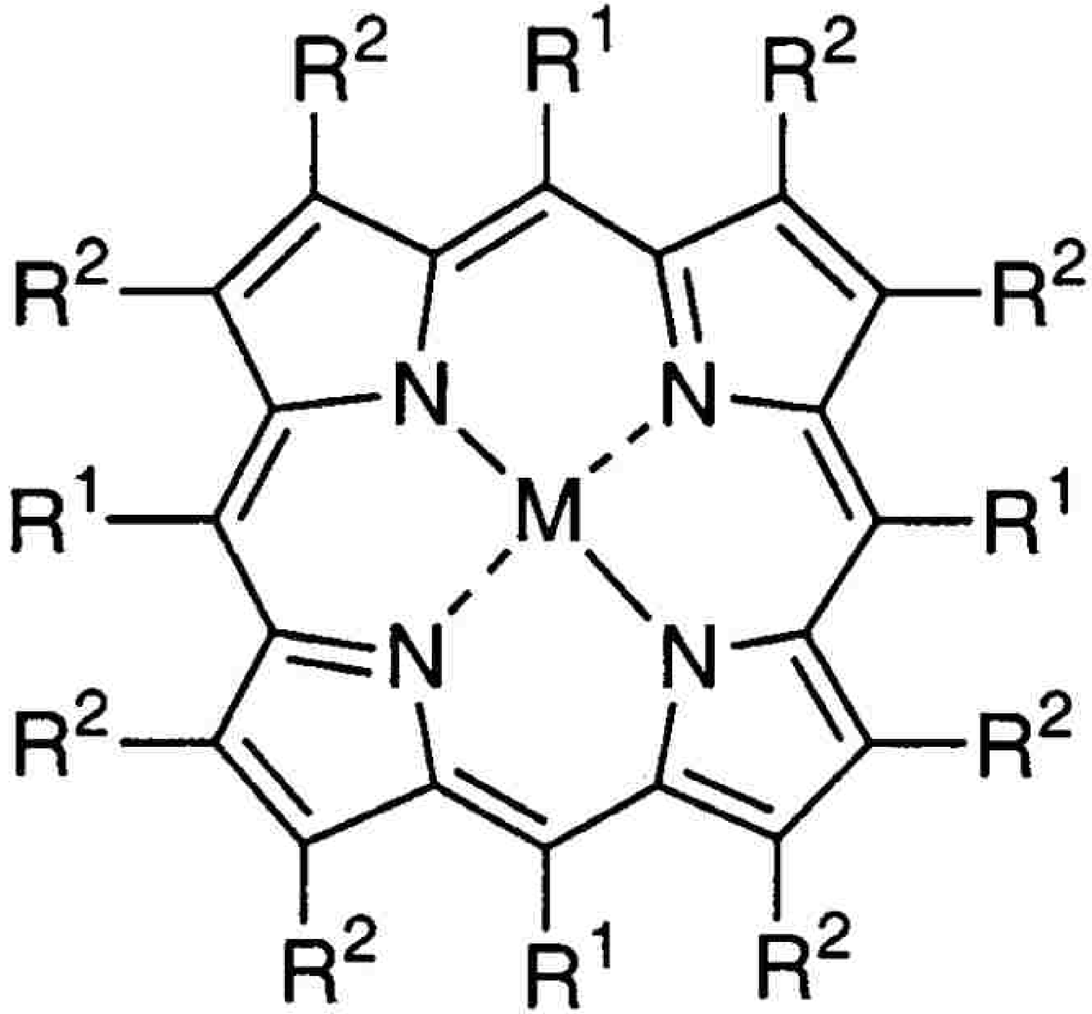

[redacted]				
1	TArP	Ar	H	[redacted]
[redacted]				
3	OArP	H	Ar	
[redacted]				

[redacted]

5.2 Background

5.2.1 Unusual Aryl Rotational Barriers in Porphyrins

Dodecaphenylporphyrin (DPP, **2a**) and related dodecaarylporphyrins (DArPs) are peripherally crowded and very nonplanar porphyrins that have been widely studied recently because of their unusual structural and spectroscopic properties.[112-130] In experiments by members of our group and collaborators[79] on aryl-porphyrin rotational barriers in peripherally crowded porphyrins, some perplexing results were obtained, as will be presented in this section. Molecular simulations will be drawn on in this chapter to attempt to rationalize the experimental results.

Variable temperature (VT) ^{1}H NMR spectroscopy is a technique that was used to experimentally determine the rotational barriers of aryl-porphyrins.[79,131-136] In order for rotation to be detected in such experiments, it is necessary to generate asymmetry in the target complex, in this case accomplished by the use of asymmetrical aryl substituents.[132-134,136] The 3-methoxyphenyl group was chosen as the standard substituent because it could be readily introduced onto the porphyrin macrocycle using existing synthetic methodologies.[129,137] 3-thienyl and 2-methoxy phenyl substituents were also used in some cases to vary the steric hindrance to rotation; 3-thienyl to lower the aryl-porphyrin rotational barrier, and 2-methoxy to increase it. This variation was also useful for assigning the aryl-porphyrin rotation process unambiguously, as some of the porphyrins studied are known to display additional dynamic processes such as NH tautomerism and macrocyclic inversion.[79]

As the rotational barriers are expected to differ between aryl substituents on the porphyrin *meso* positions and those on β positions, the study examined two different groups of porphyrins synthesized with the asymmetrical aryl substituent on the desired respective positions (hydrogen atoms or phenyl substituents occupied the remaining positions; see Figure 5.1). The first group, which was used to probe rotational barriers of *meso* aryl groups in porphyrin systems, consists of the uncrowded tetraarylporphyrins (TArPs; **1**) and the highly substituted and very nonplanar tetraaryl-octaphenylporphyrins (TArOPPs; **2**). The second group, used to investigate the barriers for the rotation of β aryl groups, consists of the relatively uncrowded octaarylporphyrins (OArPs; **3**) and the crowded octaaryl-tetraphenylporphyrins (OArTPPs; **4**). Different core substituents were used to present a variety of non-planar deformations. The effect of core metal size on aryl rotation was investigated using complexes with a small metal (M = Ni) and a large metal (M = Zn). The effect of protonation was examined using the free base porphyrin (M = 2H) and the porphyrin dication (M = $4H^{2+}$).

Activation energies ($\Delta G^{\ddagger}_{ROT}$) for rotation of the *meso* 3-methoxyphenyl groups in porphyrins **1b** and **2b** are provided in Table 5.1, along with the corresponding data for β 3-methoxyphenyl groups in porphyrins **3b** and **4b**. The activation energies are surprisingly similar among the porphyrins investigated given the significant structural differences present. Most of the barriers fall between 40 and 70 kJ mol^{-1}, with the exception of **2b** (M = $4H^{2+}$) where the barrier is much higher. For TArP **1b,** a smaller metal (Ni vs. Zn) is seen to decrease $\Delta G^{\ddagger}_{ROT}$ by 13 kJ mol^{-1}; a related decrease (12 kJ mol^{-1}) is also seen for TArOPP **2b** (M = Ni vs. Zn). On protonation of TArP **1b** from the free base to the dication (M = $4H^{2+}$ vs. M = 2H), the barriers were found to be experimentally indistinguishable, yet the barriers differed by 26 kJ mol^{-1} on protonation of TArOPP **2b.**

In comparing *meso* aryl rotational barriers between the uncrowded aryls of TArP **1b** and the crowded aryls of TArOPP **2b** (Table 5.1), the NMR results show a large increase for **2b** vs. **1b** for M = $4H^{2+}$ (44 kJ mol^{-1}) as might be expected with such a great difference in peripheral crowding. Surprisingly, however, the increase in the rotational barrier of **2b** vs. **1b** is small for M = Ni (6 kJ mol^{-1}) or for M = Zn (5 kJ mol^{-1}).

In comparison of β aryl rotation in the OArTPPs **4b** to *meso* aryl rotation in the likewise crowded TArOPPs **2b**, it is noteworthy that the rotational barriers were very close for M = Ni, yet differ greatly (49 kJ mol^{-1}) for M = $4H^{2+}$. For the β aryl rotation, it was not possible however to fully compare the crowded OArTPP **4b** to the uncrowded OArPs **3b** because of difficulties in obtaining accurate measurements of the rotational barriers in the OArPs (Table 5.1). For this reason, the emphasis in this chapter will be on the *meso* aryl rotation.

The errors in the NMR measurements are fairly large (up to 5 kJ mol^{-1}),[79] yet despite these limitations, the NMR results for the *meso* aryl-substituted porphyrins **1b** and **2b** do show that different core substituents lead to different rotational barriers as well as different changes in barrier on going from **1b** to **2b**. This is most clearly illustrated by the barriers for porphyrins **2b** (M = Ni) and **2b** (M = $4H^{2+}$), where the difference in $\Delta G^{\ddagger}$-$_{ROT}$ (36 kJ mol^{-1}) is clearly too large to be explained by experimental errors or differences in $\Delta S^{\ddagger}$ (which previous studies of aryl rotation in TArPs have suggested is small[138]). The core-dependent NMR results raise some interesting questions regarding the impact that nonplanar deformations of the porphyrin macrocycle may have on aryl-porphyrin rotational barriers. This chapter aims to rationalize these results using x-ray crystal structures and molecular simulations.

Table 5.1 Activation Energies ($\Delta G^{\ddagger}_{ROT}$; kJ mol^{-1}) for 3-Methoxyphenyl Rotation Obtained from VT ^{1}H NMR Studies.[79]

Porphyrin	M = Zn	M = Ni	M = 2H	M = $4H^{2+}$
	meso 3-Methoxyphenyl Rotation			
TArP **1b**	62±2	49±3	45±5	47±2
TArOPP **2b**	67±3	55±2	65±3	91±3
	β 3-Methoxyphenyl Rotation			
OArP **3b**	[a]	[a]	[a]	≥31±3
OArTPP **4b**	52±2	54±3	≥46±2	42 ±2

[a] $\Delta G^{\ddagger}$ could not be determined with any degree of accuracy.

5.2.2 X-ray Crystallographic Structures of Aryl Porphyrins

The diverse results of the NMR rotation studies among the crowded and uncrowded aryl systems suggest that structural differences, particularly out-of-plane distortions of the macrocycle arising from both peripheral and the core substituents, may be important in lowering the activation energy for aryl-porphyrin rotation. Indeed, in previous studies[131,132,138] of the aryl rotational barriers in uncrowded TArPs, nonplanar deformations were used to explain the differences in activation energies. The earlier interpretations[131,132,138] were based in large part on the X-ray crystal structures of TPP, where the ruffling apparent for the nickel complexes but not for the zinc complexes was used to explain the lower rotational barrier in TArP **1f** (M = Ni) versus **1f** (M = Zn).[138] It was suggested that the ruffling deformation and concomitant out-of-plane movement of the *meso* aryl groups in the nickel complexes facilitated aryl-porphyrin rotation by relieving interactions between the aryl group and the porphyrin macrocycle.[131,138] Nonplanar deformation (saddling) was also invoked to explain the lower barriers in the dications versus the free bases of porphyrins **1f** and **1d**; in this case, however, the *meso* aryl remains in plane while the neighboring porphyrin β carbons move out of plane to relieve steric interaction. [132,138]

In this section, published x-ray crystal structures available for the pertinent aryl porphyrins are studied with the aim of seeing whether it is possible to rationalize the aryl-porphyrin rotational barriers in DArPs in a similar manner to that previously applied to TArPs. The relationship between the peripheral and core substituents present for the TArPs, OArPs, and DArPs (TArOPPs/OArTPPs), and the conformation of the porphyrin macrocycle is investigated, with particular emphasis placed on determining the conformations of the TArOPPs with different cores and comparing them to those seen for the TArPs. The compounds examined in this section are not identical to those for which the rotational barriers were observed in the last section. This is because the compounds used in the NMR studies have asymmetrical aryl substituents to allow rotation to be detected, whereas most of the porphyrins examined by X-ray crystallography have phenyl substituents or symmetrical aryl substituents to avoid the problems presented by the porphyrin crystallizing with multiple orientations of the aryl substituents (atropisomers). The effect on the structure of adding or changing a substituent (e.g. adding a methoxyl group at the meta position of the phenyl ring) is expected to be small in the systems we are studying, as affirmed by the MM calculations discussed later, so it will not alter the conclusions reached. Crystal packing forces, however, may have a significant impact on some x-ray structures.

Table 5.2 summarizes the nonplanar deformations for the TArPs, OArPs, DArPs (TArOPPs/OArTPPs) as determined using Normal-coordinate Structural Decomposition (NSD) of the crystal structures. Also, from select X-ray structures, some interatomic distances (non-bonded) representative of the steric crowding of the aryl substituents at the porphyrin periphery are presented in Table 5.3.

Table 5.2 NSD Analysis of the Out-of-plane Deformations for the uncrowded TPP Complexes and the crowded DArP (TArOPP and OArTPP) Complexes.

Porphyrin	CCDC Refcode	d_{obs}[1]	d_{sad} (B_{2u})[2]	d_{ruf} (B_{1u})	d_{dom} (A_{2u})	$d_{wav(x)}$ ($E_{g(x)}$)	$d_{wav(y)}$ ($E_{g(Y)}$)	d_{pro} (A_{1u})
ZnTPP (monoclinic)	ZZZTAY03	0.175	0.000	0.000	0.000	-0.158	0.018	0.000
ZnTPP (triclinic)	ZZZTAY02	0.297	0.000	0.000	0.000	-0.194	0.136	0.000
NiTPP	ZZZUUC01	1.295	-0.256	-1.266	0.000	0.000	0.000	-0.001
H_2TPP	TPHPOR01	0.333	0.000	0.000	0.000	0.114	0.232	0.000
H_2TPP [benzyl alcohol]	JIVRAH	0.046	0.000	0.000	0.000	0.009	0.011	0.000
H_2TPP [m-xylene]	SEMNIH	0.065	0.000	0.000	0.000	0.003	0.039	0.000
H_2TPP [p-xylene]	SEMNUT	0.233	0.000	0.000	0.000	0.057	0.197	0.000
H_2TPP	TPHPOR10	1.082	0.183	1.055	0.000	0.000	0.000	0.000
H_4TPP^{2+} $(HSO_4)_2$	LEXSIQ	2.520	2.434	0.000	0.045	0.000	0.031	0.000
H_4TPP^{2+} $(CF_3CO_{2,})_4$ (UO_2)	CAXHAK	2.670	2.586	0.169	0.025	0.000	0.068	0.022
H_4TPP^{2+} $(ClO_4)_2$ $[C_6H_6]$	RUHQEQ	2.743	2.662	0.000	0.181	0.053	0.108	0.014
H_4TPP^{2+} $(ClO_4)_2$ $[CH_3OH]$	YEVJAN	3.042	2.964	0.007	0.021	0.069	0.040	0.024
H_4TPP^{2+} $(Cl)(FeCl_4)$	TPPFEC	3.272	3.114	0.754	0.000	0.000	0.000	0.000
Zn^{II} DPP #1	ZAWRES	2.896	-2.882	0.000	-0.084	0.000	0.000	0.000
Zn^{II} DPP #2	XAWSAP	3.074	3.059	0.000	0.000	0.000	0.000	0.000
Ni^{II} DPP #1	TEZXIF	2.4405	-0.060	-2.439	0.000	0.000	0.000	0.000
Ni^{II} DPP #2	XAWROC	3.550	-3.098	-1.707	-0.156	0.000	0.000	-0.083
Ni^{II} DPP #3	XAWRUI	2.717	0.917	-2.555	0.051	-0.027	0.009	-0.028
Ni^{II} DPP #4	XAWSET	2.522	0.827	-2.377	0.058	0.004	-0.040	-0.014
4c (M = Ni) Molecule 1	[79]	3.282	-2.770	-1.751	0.002	-0.004	0.062	0.019
4c (M = Ni) Molecule 2	[79]	2.826	1.247	-2.530	-0.079	0.000	0.000	0.078
H_2DPP #1	LADGAY	3.032	2.963	0.000	0.499	-0.098	0.000	0.000
H_2DPP #2	XAWRIW	3.922	3.835	0.000	-0.173	-0.184	0.000	0.000
4e (M = $4H^{2+}$) $(Picrate)_2$	[79]	3.858	3.769	0.420	-0.016	-0.049	0.221	0.031

[1] Total out-of-plane deformation (Å).

[2] Deformation in the lowest frequency mode of each symmetry type (Å).

Table 5.3 Non-bonded Interactions (Å) at the Periphery of the Aryl-Substituted Porphyrins.

Porphyrin	CCDC Refcode	Conf	C_{ipso}(*meso*), C (β)	C_{ipso}(*meso*), C_{ipso} (β)	C_{ipso} (β), C_{ipso} (β)'	C (*meso*), C_{ipso} (β)
ZnTPP (monoclinic)	ZZZTAY03	Planar	2.92	N/A	N/A	N/A
NiTPP	ZZZUUC01	Ruffled	2.92	N/A	N/A	N/A
H_2TPP	SEMNIH	Planar	2.91	N/A	N/A	N/A
H_4TPP^{2+} $(ClO_4)_2$	YEVJAN	Saddled	3.04	N/A	N/A	N/A
Ni^{II} DPP #1	TEZXIF	Ruffled	3.01	3.00	2.95	3.26
Zn^{II} DPP #1	ZAWRES	Saddled	3.01	3.02	3.06	3.25
H_2DPP #1	LADGAY	Saddled	3.03	3.04	3.13	3.21
4e (M = $4H^{2+}$) $(Picrate)_2$	[79]	Saddled	3.10	3.12	3.16	3.20

We consider first the published data for the uncrowded TArP parent system tetraphenylporphyrin (TPP, **1a**) and the uncrowded OArP parent system octaphenylporphyrin (OPP, **3a**). No structural data is available for OPP,[139] but TPP has been extensively investigated and crystal structures have been reported for the zinc complex (ZnTPP), the nickel complex (NiTPP), the free base porphyrin (H_2TPP), and the dication (H_4TPP^{2+}). Table 5.2 lists the total out-of-plane deformation (d_{obs}) calculated using all the out-of-plane modes, as well as the contributions from the lowest frequency mode of each symmetry type (e.g. d_{sad} which corresponds to the lowest energy B_{2u} 'saddling' mode). These low frequency modes typically encompass most of the nonplanar deformation.[82] Here, the ruffling (*ruf*) and saddling (*sad*) distortions in particular constitute the majority of the nonplanar deformation observed in each structure with smaller contributions from the doming (*dom*), waving (*wav*) and propellering (*pro*) modes (This is not surprising as ruffling and saddling are the softest out-of-plane modes and therefore produce the largest out-of-plane distortions[82]). The following discussion is thus restricted to the relevant *ruf* and *sad* deformation modes, which conveniently correspond to out-of-plane displacements along the axes of substitution for the porphyrins investigated in our study, as ruffling will move the *meso* aryl substituents out-of-plane whereas saddling will move the β aryl substituents out-of-plane (see Figure 1.2). The crystallographic studies show that ZnTPP is essentially planar (d_{obs} 0.2-0.3 Å), NiTPP is slightly ruffled (d_{ruf} 1.3 Å), H_2TPP is typically planar (although a slightly ruffled structure has been reported), and H_4TPP^{2+} is strongly saddled irrespective of the anion present (d_{sad} 2.5-3.3 Å). The structural changes seen for TPP as a function of M (core substituent) are typical for porphyrins.[67] Generally, small metals which require short metal-nitrogen distances favor ruffling because this distortion mode produces the smallest core.[68] In contrast, protonation favors saddling because this deformation reduces the crowding between the protons in the core, whereas ruffling would result in strong contraction of the core[68] will significantly increase repulsive interactions between the four inner hydrogens.

All of the DArPs' NSD analyses (Table 5.2) exhibit highly distorted macrocycles due to the need to minimize steric repulsions between the peripheral phenyl substituents. Dodecaphenylporphyrin (DPP, **2a**), the parent DArP from which the TArOPPs (**2**) and OArTPPs (**4**) are derived, has been the subject of several crystallographic investigations.[121,125,140] For H_2DPP (**2a**, M=2H), the two crystal structures reported[121,140] show primarily saddle distortion of the porphyrin macrocycle, although one structure (CCDC refcode XAWRIW) is significantly more nonplanar (d_{obs} 3.9 vs. 3.0 Å), and the other (LADGAY) has a significant doming component. For ZnDPP (**2a**, M=Zn), the two crystal structures reported[140] show quite similar amounts of nonplanar deformation (d_{obs} approximately 3 Å) that is predominantly of the saddle type. For NiDPP (**2a**, M=Ni), no fewer than four X-ray structures have been reported[125,140] amongst which the macrocycle can adopt structures with ruffle and/or saddle deformations: one structure (TEZXIF) is ruffled, two (XAWUI and XAWSET) are mainly ruffled with some saddle deformation, and one (XAWROC) is saddled with a significant amount of ruffle deformation. This indicates that the macrocycle is conformationally flexible with this metal at the core. The increased preference of the nickel complex for a ruffled conformation as compared to the zinc complex is expected given the known tendency of nickel to favor short metal-nitrogen distances and the greater core contraction that occurs with ruffle versus saddle deformation.[68]

The greater conformational flexibility of the nickel complexes was also seen in other DArPs (Table 5.2). In the crystal structure[79] of the OArTPP **4** (M = Ni), the macrocycle adopts two different conformations in the asymmetric unit (besides the 3-thienyl groups being rotationally disordered over two positions as expected). Both conformations are very nonplanar (d_{obs} = 3.3 and 2.8 Å) and contain mixtures of saddle and ruffle deformations, with one conformation having principally saddle deformation and the second having mainly ruffle deformation.

Although crystallographic data has not been reported for the DPP dication (H_4DPP^{2+}), crystals were reported for the dication of OArTPP **4e** (M = $4H^{2+}$, picrate counter ions), which has 4-fluorophenyl groups at the β positions of the porphyrin rather than phenyls. The presence of a fluoro group at the para position of the phenyl ring likely has minimal impact on the observed structure. OArTPP **4e** (M = $4H^{2+}$) $(pic)_2$ displays a very nonplanar conformation (d_{obs} 3.9 Å), predominantly saddle (3.8 Å) with a small amount of ruffle (0.4 Å). Overall, the structure is consistent with the tendency of both peripheral crowding and protonation to increase nonplanarity of the porphyrin macrocycle; it is more nonplanar than the less crowded H_4TPP^{2+} and than at least one form of H_2DPP (Table 5.2).

The structural data for the DArPs in summary shows that a *sad* conformation is favored by the macrocycle when M = Zn, 2H or $4H^{2+}$, but both the *sad* and/or the *ruf* conformations can be accessed when Ni^{II}, a small metal, is present. The ability of the Ni^{II} complexes to access the *ruf* conformation is presumably the result of the *ruf* conformation being better able to provide the short metal-nitrogen distance favored by Ni^{II}. Overall, the structural changes seen for the DArPs as a function of the core substituent M are similar to those for the TArPs: switching to a smaller metal (Ni vs. Zn) increases the tendency of the macrocycle to ruffle, whereas protonation increases the amount of saddle deformation (at least compared to one H_2DPP structure).

The crystal structure geometries are next examined from the viewpoint of the steric crowding around the phenyl/ aryl rotors. In an earlier report,[138] as mentioned above, it was suggested that the lower aryl-porphyrin rotation barriers for nickel versus zinc in TArPs were the result of a relieving of steric interactions between the aryl group and the porphyrin macrocycle as a result of out-of-plane movement of the *meso* aryl groups concomitant with ruffling in the nickel complexes. Curiously, an analysis of the close contacts at the porphyrin periphery (Table 5.3) for ruffled NiTPP and planar ZnTPP shows that the distance between the *ipso* carbons of the *meso* phenyl rings and the β pyrrole carbons are similar (2.92 Å). This makes it difficult to understand the decrease in rotational barrier purely on the basis of the static distortions seen in the crystal structures, and suggests that the nickel complex deforms more during the rotation process than is apparent in the X-ray structure (i.e., the deformability of the macrocycle is important).

The trends in the close contacts for the *meso* aryl substituents in the DArPs parallel those seen for the TArPs, though the distances are slightly greater in the DArPs (Table 5.3). The C_{ipso}(*meso*)-C_{β} distances are about the same (3.02±0.01 Å) for *ruf* NiDPP, *sad* ZnDPP and H_2DPP (CCDC refcode LADGAY) but approximately 0.1 Å greater for OArTPP **4e** (M = $4H^{2+}$) $(pic)_2$. A similar pattern is seen for the distance between C_{ipso}(*meso*) and C_{ipso} (β); again longer in the dication. Based purely on these findings, it would seem reasonable to expect the dication to have the lowest aryl-porphyrin rotational barrier, yet the NMR results (Section 5.2.1) show that this is not the case, and the barrier in the dication of TArOPP **2b** is actually much higher than in the nickel complex (102 kJ mol^{-1} versus 58 kJ mol^{-1}).

Finally, it is worth noting that the fact that some of the structures above exhibited multiple conformations when crystallized, for example OArTPP **4c** (M = Ni) with one principally saddle structure and a second having mainly ruffle deformation (Table 5.2). This is probably due to the fact that the energy required to deform the macrocycle is small for small amounts of deformation, i.e. there is a fairly shallow potential energy surface.[60] This is particularly true for porphyrins with small metals such as nickel, where it is known, for example, that NiOEP exists in both planar and nonplanar conformations in the solid state and also in solution.[141,142] In such cases there is a trade-off between the structural requirements of the metal (short metal-nitrogen distance, which favors ruffling) and the porphyrin ring (maximizing π-overlap, which favors a planar macrocycle). Given the fine balance between these two forces, the crystallization conditions and crystal packing forces become important in determining the observed conformation. Furthermore, any of the crystal structures with other cores may also be somewhat affected by crystal packing forces and so might not well represent the solution structure. This underscores the need for caution when interpreting the spectroscopic properties of porphyrins using the static picture obtained from X-ray crystallographic studies.

5.3 Experimental

5.3.1 Molecular Mechanics Calculations and Normal-coordinate Structural Decomposition.

MM calculations have been previously applied (using the Shelnutt force field) to investigate some dynamic processes including axial ligand rotation.[80,143] MM calculations were carried out using Cerius2 software (Accelrys Inc., San Diego) and the Shelnutt metalloporphyrin force-field. The force-field was originally parameterized for nickel porphyrins[20] and subsequently extended to other transition metals including zinc,[67] so it could be readily applied to the metal complexes (Ni and Zn) used in our study. To calculate the structures of the free base porphyrins and porphyrin dications, hydrogen-bonded H atoms were used to represent the inner hydrogen atoms. Counter ions were not included in the calculations and the default charge scheme was employed. The calculations were performed with a dielectric constant of 2.64 (for CS_2); this dielectric constant was used for consistency with earlier studies, and also reasonably approximates the nonpolar solvents used in the NMR studies (e.g. CD_2Cl_2 or $C_6D_5CD_3$).

The Normal-coordinate Structural Decomposition (NSD) program used to analyze the nonplanar deformations present in the crystal structures has been fully described in the literature[82] and a browser based version is available for general use at http://jasheln.unm.edu.

5.4 Molecular Simulations.

Molecular mechanics (MM) calculations were employed to try to gain insights into the aryl rotation processes in crowded and uncrowded porphyrins and their relation to the structural preferences of the porphyrin macrocycle. This study focused on the rotation of *meso* aryl substituents as the movements of the porphyrin’s four *meso* positions are more easily defined than those of the eight β positions which, besides movement in and out of plane, are subject to twist in the pyrrole rings. Furthermore, the effect of crowding of peripheral groups is better isolated when comparing the DArPs to the *meso* TArPs than to the β OArPs.

Molecular mechanics calculations were hence performed on the TArPs **1b** and TArOPPs **2b,** which were investigated in detail in the NMR studies, with a variety of cores. The global minimum energy structures were first calculated and compared to the x-ray crystal structures. Then, to calculate the aryl-porphyrin rotational barriers, the aryl group was rotated using a 'dihedral drive' procedure, with the porphyrin macrocycle being allowed to relax fully at each step of the drive.

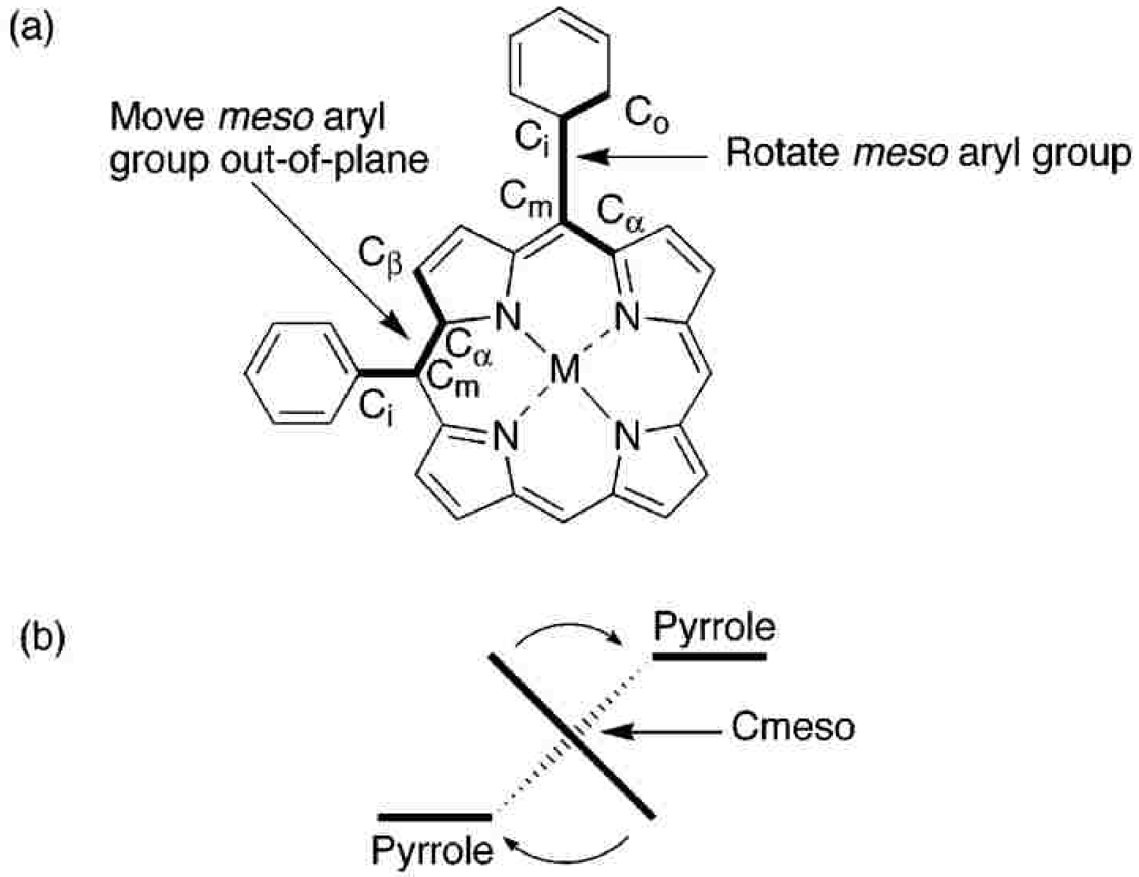

Figure 5.2 Diagrams showing (a) the torsion angles used in the molecular mechanics calculations of the *meso* aryl rotational barriers, and (b) the definition of clockwise rotation of a *meso* aryl group in a saddle deformed porphyrin.

5.4.1 Simulated Structures and Rotational Barriers in TArPs

The global minimum energy structure of TArP **1b** (M = Ni) was found to be modestly ruffled, **1b** (M = Zn) approximately planar, **1b** (M = 2H) slightly saddled, and **1b** (M = $4H^{2+}$) strongly saddled. These results are in general agreement with the crystallographic data for TPP derivatives (Table 5.2).

Using the energy minimized αβαβ structure as a starting point, the rotational barriers were then calculated using a 'dihedral drive'. The C_{α}-C_{m}-C_{i}-C_{o} torsion angle shown in Figure 5.2a was used to drive the *meso* aryl group, which was rotated in 10° increments with smaller changes around the energy maximum while the rest of the porphyrin structure was allowed to relax fully at each of the steps. The rotations were performed in both clockwise and counterclockwise directions (as defined in Figure 5.2b); the rotational sense was only found to be important for the saddle structures.

The rotational barriers ($\Delta E^{\ddagger}_{ROT}$) determined from MM calculations for TArP **1b** with various cores are as follows: Ni 50 kJ mol^{-1}, Zn 80 kJ mol^{-1}, 2H 59 kJ mol^{-1}, and $4H^{2+}$ 51 kJ mol^{-1}. For TArP **1b** (M = Ni), the lowest barrier (50 kJ mol^{-1}) was obtained by rotating the aryl group about the minimum energy *ruf* structure, i.e. rotation occurred when the aryl group was out of the least-squares plane of the porphyrin macrocycle. In contrast, for TArP **1b** (M = $4H^{2+}$) the lowest barrier (51 kJ mol^{-1}) was obtained by rotating the aryl group about the minimum energy *sad* structure, which corresponds to rotation in the plane of the porphyrin macrocycle.

The out-of-plane rotation pathway was also investigated for **1b** (M = $4H^{2+}$). The out-of-plane pathway was approximated by constraining the aryl substituent to move out-of-plane using two C_β-C_α-C_m-C_i torsion angles as shown in Figure 5.2a. The C_α-C_m-C_i-C_o and C_β-C_α-C_m-C_i torsion angles were then varied independently to determine the lowest energy pathway. An optimized C_β-C_α-C_m-C_i torsion angle of 50° was found to produce only a slightly higher (62 kJ mol^{-1}) barrier for out-of-plane rotation than for in-plane rotation (51 kJ mol^{-1}). In the case of **1b** (M = Zn), rotating the aryl group in-plane about the minimum energy structure produced a higher barrier (88 kJ mol^{-1}) than that obtained by constraining the C_β-C_α-C_m-C_i torsion angles to force the aryl substituent to rotate out-of-plane (80 kJ mol^{-1}). A similar effect was observed for the free base porphyrin **1b** (M = 2H), although in this case the difference between the in-plane (118 kJ mol^{-1}) and out-of-plane (59 kJ mol^{-1}) pathways was much larger. The optimized C_β-C_α-C_m-C_i torsion angles for **1b** (M = Zn) and **1b** (M = 2H) (50-55°) were found to similar to that seen for **1b** (M = $4H^{2+}$) (50°).

Overall, the MM calculations correctly predict the structures and, in agreement with the trends in the experimental rotational barriers for the TArPs **1b** (Table 5.1), show a lower barrier for the nickel complex versus the zinc complex (50 vs. 80 kJ mol^{-1}) and also for the dication versus the free base porphyrin (51 vs. 59 kJ mol^{-1}). The MM predictions were most accurate for the nickel (for which the force field was originally parameterized) and dication complexes.

5.4.1.1 Effect of Addition of 3-methoxy Group to Phenyl Ring

The NMR rotational barrier experiments, as mentioned previously, required an asymmetric aryl substituent (particularly 3-methoxy phenyl) while crystal x-ray structural data was generally available for the bare phenyl substituent, hence calling into question comparisons between the structural and dynamic data. In order to ensure that the substituent in question does not greatly alter the structure of the molecule, molecular mechanics calculations were performed on TPP (**1a**) and TArP **1b** using a full range of core substituents (M = Ni, Zn, 2H or $4H^{2+}$). Global minimum energy structures were found to be similar for both porphyrins, regardless of core substituents. It should be noted that the different substituents might have structural impact via crystal packing in solids, but this is not relevant to the aryl substituent rotors in solution or interface.

Aryl rotational barriers were also calculated for TPP (**1a**) and TArP **1b** using a straightforward 'dihedral drive' procedure, and on comparison it was found that the methoxyl group had no effect. Of course, in these tetra-aryl porphyrins the *meso* aryl substituents are uncrowded and we do not expect the effect to hold for the rotational barriers in dodeca-aryl porphyrin whence the methoxy group will likely hinder rotation. This is supported by the experimental differences in rotational barriers of TArOPPs **2b** and **2c** as the aryl substituent varies from 3-methoxy to 3-thienyl groups.[79] Nevertheless, even in highly substituted porphyrins the methoxyl group would not point towards neighboring phenyl groups and is unlikely to affect the static picture for comparison to x-ray crystal data, so only the asymmetric compounds used in the NMR studies will be simulated for direct comparison of rotational barriers.

The *relative* orientation of the methoxyl groups (the atropisomer) was also found to have a negligible effect on the energy minimized structure and on the calculated rotational barrier, so the αβαβ atropisomer (i.e. alternating up and down methoxyl groups) was used as a starting conformation in all of the calculations.

Table 5.4 Barriers for *meso* 3-Methoxyphenyl Rotation ($\Delta E^{\ddagger}_{ROT}$; kJ mol^{-1}) in TArOPPs and TArPs Obtained from Molecular Mechanics Calculations, with NMR experimental values for comparison.

Porphyrin	M = Ni		M = $4H^{2+}$	
	MM	NMR[79]	MM	NMR[79]
TArOPP **2b**	58	55±2	102	91±3
TArP **1b**	50	49±3	51	47±2
Difference (**2b – 1b**)	8	6	51	44

5.4.2 Simulated Structures and Rotational Barriers in DArPs

MM calculations were then performed for the dodeca-substituted TArOPP **2b**, which is related to TArP **1b** by the addition of phenyl rings to all eight of the unsubstituted pyrrole positions, and is the DArP form used in the NMR studies. Calculations were carried out for TArOPP **2b** with two core substituents: M = $4H^{2+}$, which is expected to be the least conformationally flexible system because the protons in the core will strongly favor a *sad* structure, and M = Ni, which based on the X-ray data is expected to be the most conformationally flexible system and to adopt *sad* and/or *ruf* structures. The calculated rotational barriers were also the most accurate relative to experimental values for these two core substituents in the case of the TArPs (see Section 5.4.1).

The calculated global minimum energy structure of TArOPP dication **2b** (M = $4H^{2+}$) was found to be strongly saddle distorted in agreement with the related crystal structure of OArTPP dication **4e** (M = $4H^{2+}$) (Table 5.2). The nickel complex **2b** (M = Ni) was also found to have a *sad* conformation as the global minimum energy structure, although the *ruf* conformation was also obtained as a stable local minimum only 15 kJ mol^{-1} higher in energy than the *sad* conformation. The finding of *sad* and *ruf* conformations of similar energies for the nickel complex of **2b** is consistent with the crystallographic data discussed in Section 5.2.2 , which showed both *sad* and *ruf* conformations for NiDPP and mixed *sad*/*ruf* conformations for OArTPP **4c** (M = Ni) (Table 5.2).[125,140] A stable ruffled conformation could not be obtained, on the other hand, for the dication of **2b** (M = $4H^{2+}$).

The aryl-porphyrin rotational barriers were simulated using the same 'dihedral drive' procedure described in the previous section for the TArPs, using the same convention for rotational direction (Figure 5.2b). The results are presented in Table 5.4, together with those calculated for the complementary TArPs (Section 5.4.1) and the experimental (NMR) results (Section 5.2.1). The MM calculations showed increases in $\Delta E^{\ddagger}_{ROT}$ with the addition of eight phenyl rings to TArP **1b** to produce TArOPP **2b** for the two core substituents investigated (M = Ni or $4H^{2+}$). The MM calculations of these porphyrins yield rotational barriers that agree fairly well with those obtained from the NMR studies (Section 5.2.1): **2b** (M = Ni) 58 (exp. 55±2), **2b** (M = $4H^{2+}$) 102 (exp. 91±3); **1b** (M = Ni) 50 (exp. 49±3), **1b** (M = $4H^{2+}$) 51 (exp. 47±2) kJ mol^{-1}.

For the nickel complex of TArOPP **2b**, the lowest barrier for rotation of the 3-methoxyphenyl group was found when the macrocycle was ruffled and the *meso* aryl group moved farther out of the porphyrin plane; the calculated barrier (58 kJ mol^{-1}) was only marginally higher than that obtained for the nickel TArP **1b** (50 kJ mol^{-1}) despite the addition of eight phenyl rings to the porphyrin periphery. The lowest barrier for rotation of the 3-methoxyphenyl group in the dication of TArOPP **2b** was much higher (102 kJ mol^{-1}) and was obtained when the aryl group was rotated clockwise from the saddled minimum energy structure, which forced the *meso* aryl group to move out-of-plane; rotating the *meso* aryl group counterclockwise did not move the aryl group out-of-plane and gave a significantly higher barrier (133 kJ mol^{-1}). Unlike the case of the corresponding nickel complexes, the barrier for the dication of TArOPP **2b** (102 kJ mol^{-1}) was much higher than that calculated for the dication of TArP **1b** (51 kJ mol^{-1}). The barrier calculated for the dication of **2b** (102 kJ mol^{-1}) was also considerably higher than the barrier for the nickel complex of **2b** (58 kJ mol^{-1}). The MM calculations are in excellent agreement with the NMR studies in that a small increase in the rotational barrier is found on going from the TArP **1b** to the TArOPP **2b** in the case of a nickel core (obs. 6; calc. 8 kJ mol^{-1}) and a much larger increase is found for the dication (obs. 44; calc. 51 kJ mol^{-1}).

Importantly, the direction of aryl rotation was found to matter for the dication of TArOPP **2b**. When the *meso* 3-methoxyphenyl group was rotated clockwise (Figure 5.2b) from the saddled minimum energy structure, it was forced to move out-of-plane and the barrier for rotation was 102 kJ mol^{-1}; rotating the *meso* aryl group counterclockwise, however, did not move the aryl group out-of-plane and gave a barrier of 133 kJ mol^{-1}, significantly higher (31 kJ mol^{-1} difference). As mentioned in the introduction, unidirectional rotation is often considered a prerequisite for a molecular motor.[111]

It is also worth noting that the only time the lowest energy pathway for aryl-porphyrin rotation is not calculated to involve out-of-plane movement of the *meso* aryl group is in the case of the dication of TArP **1b**. This may be because such a large amount of saddle deformation occurs with protonation of the core that in-plane rotation can compete with out-of-plane rotation. A similar in-plane rotation mechanism most likely cannot compete for the TArOPPs because the periphery is so highly substituted.

As noted earlier, an analysis of crystallographic data for the DArPs shows that the C_{ipso}(*meso*)-C(β) and C_{ipso}(*meso*)-C_{ipso}(β) distances are longer in the DArP dication **4e** (M = $4H^{2+}$) $(pic)_2$ than in the *ruf* nickel DPP (Table 5.3), implying that the rotational barrier should be lower in the dication. The NMR results (Section 5.2.1), however, showed that this is not the case, and the barrier in the dication of TArOPP **2b** is actually much higher than in the nickel complex (102 kJ mol^{-1} versus 58 kJ mol^{-1}). In contrast to the static picture obtained from the crystal structures, the MM calculations presented in Table 5.4 are in excellent agreement with the experimental results. The MM results show that the *meso* aryl rotational barrier in the TArOPP **2b** is strongly influenced by the deformability along the ruffling coordinate, i.e. the barrier can be effectively lowered if the macrocycle allows a concerted motion of the aryl group farther out of the porphyrin plane together with its rotation, thus minimizing interactions with the rest of the porphyrin. A core substituent which favors or permits ruffling, such as nickel, will facilitate the *meso* aryl group moving out-of-plane to minimize aryl-porphyrin interactions and decrease the rotational barrier. In contrast, a core substituent which disfavors ruffling (such as four protons, where severe steric crowding would occur in the core) will inhibit the aryl group from moving out-of-plane and increase the rotational barrier.

The experimental rotational barriers for porphyrins **1b** and **2b** with other core substituents are also consistent with this deformability model (Section 5.2.1). A larger metal (Zn vs. Ni) was seen (Table 5.1) to increase $\Delta G^{\ddagger}_{ROT}$ by 13 kJ mol^{-1} for TArPs **1b**; a related increase (12 kJ mol^{-1}) was seen for TArOPPs **2b** (Zn vs. Ni), presumably of similar origins, i.e. the ability of the nickel complex to more readily deform along the *ruf* coordinate and move the *meso* substituent out-of-plane to facilitate rotation (as supported by the deformations from X-ray structures for NiDPP and ZnDPP in Section 5.2.2). Although the NMR data for the β aryl-substituted porphyrins (**3b** and **4b**) was incomplete, the barriers which could be measured (Table 5.1) can be interpreted in terms of the out-of-plane deformability model discussed for the TArOPPs. Just as ruffling lowers the barrier for *meso* aryl rotation by moving the *meso* position out-of-plane, so saddling (which moves the pyrrole β positions out-of-plane) appears to lower the barrier for β aryl rotation.

5.5 Conclusions & Implications.

In conclusion, the molecular simulations were helpful in explaining the unusual aryl rotational behavior in aryl porphyrins and providing insights into their application as molecular rotors. The studies of the DArPs show that out-of-plane deformability of the macrocycle is important in lowering the activation energy for aryl-porphyrin rotation. Overall, they suggest a relationship between the position of the aryl substituent being rotated (*meso* or β) and the symmetry of the deformation mode required to lower the rotational barrier. Easier deformability along the ruffling coordinate lowers the barrier for *meso* aryl rotational barriers whereas saddling lowers the barrier for β aryl rotation. Furthermore, it was shown that for the saddled TArOPP **2b** (M = $4H^{2+}$), a significant difference in rotational barrier exists between the two directions of aryl rotation (31 kJ mol^{-1}), resulting in unidirectional rotation. This is likely the case for many other aryl-porphyrin rotors, particularly in similarly saddled structures.

While many molecular rotors have been designed, the porphyrin-based system has several distinct advantages. First, the rotors may be used not only in solution, but also in solids (molecular crystals) or mounted to surfaces. Porphyrins have many sites that could be used to tether them to surfaces or other molecules, and they may also stack together due to pi interactions. Secondly, as a delicate interplay of several forces determines the rotational barrier, it may be tweaked as desired via several factors such as bulk or the aryl rotor or non-planarity of the porphyrin macrocycle. Another advantage is the ability to produce unidirectional rotation, a challenging feature that is critical for molecular motors. Molecular motors would need a supply of energy, and porphyrin systems permit various mechanisms for the energy to be supplied, such as thermally, chemically, or photochemically; use of a charged aryl substituent would also enable rotation driven by an external electric field. Finally, the rotor system could be reversibly switched on and off via triggers that cause large structural changes in the porphyrin (as discussed in the previous chapter), such as metal exchange (e.g. Ni/Zn), axial ligation, or photo-excitation.

REFERENCES

(1) Makarska, M.; Radzki *Annales Universitatis Mariae Curie-Sklodowska Lublin* **2002**, *LVII*, 332.

(2) Senge, M. *CHEMICAL COMMUNICATIONS* **2006**, 243-256.

(3) Goldoni, A. Porphyrins: fascinating molecules with biological significance.

(4) Milgrom, L. *The colours of life : an introduction to the chemistry of porphyrins and related compounds*; Oxford University Press: Oxford ;;New York, 1997.

(5) Barkigia, K. M.; Renner, M. W.; Senge, M. O.; Fajer, J. *J. Phys. Chem. B* **2004**, *108*, 2173-2180.

(6) SCHEIDT, W. *J STRUCT BONDING BER 64*, 1.

(7) Jentzen, W.; Song, X. Z.; Shelnutt, J. A. *J. Phys. Chem. B* **1997**, *101*, 1684-1699.

(8) Jentzen, W.; Ma, J. G.; Shelnutt, J. A. *Biophys. J.* **1998**, *74*, 753-763.

(9) MAZZANTI, M.; MARCHON, J. C.; Shang, M. Y.; SCHEIDT, W. R.; Jia, S. L.; Shelnutt, J. A. *J. Am. Chem. Soc.* **1997**, *119*, 12400-12401.

(10) Shelnutt, J. A.; Song, X. Z.; Ma, J. G.; Jia, S. L.; Jentzen, W.; MEDFORTH, C. J. *Chem. Soc. Rev.* **1998**, *27*, 31-41.

(11) Platt, J. In *RADIATION BIOLOGY: VOLUME III: VISIBLE AND NEAR-VISIBLE LIGHT*; MCGRAW-HILL, 1956.

(12) Song, X. *Ph.D. Thesis*; University of New Mexico: New Mexico, 1997.

(13) Gouterman, M. *Journal of Molecular Spectroscopy* **1961**, *6*, 138-163.

(14) Gouterman, M.; Wagnière, G. H.; Snyder, L. C. *Journal of Molecular Spectroscopy* **1963**, *11*, 108-127.

(15) Spiro, T.; Li, X. In *Biological Applications of Raman Spectroscopy (Spiro, T. G., Ed.)*; John Wiley & Sons, 1988; Vol. 3.

(16) SPIRO, T. *IRON PORPHYRINS 2* 89.

(17) Li, X. Y.; CZERNUSZEWICZ, R. S.; KINCAID, J. R.; SU, Y. O.; SPIRO, T. G. *J. Phys. Chem.* **1990**, *94*, 31-47.

(18) Li, X. Y.; CZERNUSZEWICZ, R. S.; KINCAID, J. R.; SPIRO, T. G. *J. Am. Chem. Soc.* **1989**, *111*, 7012-7023.

(19) Hoard, J. L. *Ann. NY Acad. Sci.* **1973**, *206*, 18-31.

(20) Shelnutt, J. A.; MEDFORTH, C. J.; BERBER, M. D.; BARKIGIA, K. M.; Smith, K. M. *J. Am. Chem. Soc.* **1991**, *113*, 4077-4087.

(21) MAYO, S. L.; OLAFSON, B. D.; Goddard, W. A. *J. Phys. Chem.* **1990**, *94*, 8897-8909.

(22) Shelnutt, J. A.; MEDFORTH, C. J.; BERBER, M. D.; BARKIGIA, K. M.; Smith, K. M. *J. Am. Chem. Soc.* **1991**, *113*, 4077-4087.

(23) SPARKS, L. D.; ANDERSON, K. K.; MEDFORTH, C. J.; Smith, K. M.; Shelnutt, J. A. *Inorg. Chem.* **1994**, *33*, 2297-2302.

(24) SPARKS, L. D.; MEDFORTH, C. J.; Park, M. S.; Chamberlain, J. R.; ONDRIAS, M. R.; SENGE, M. O.; Smith, K. M.; Shelnutt, J. A. *J. Am. Chem. Soc.* **1993**, *115*, 581-592.

(25) Jentzen, W.; SIMPSON, M. C.; HOBBS, J. D.; Song, X.; Ema, T.; NELSON, N. Y.; MEDFORTH, C. J.; Smith, K. M.; VEYRAT, M.; MAZZANTI, M.; RAMASSEUL, R.; MARCHON, J. C.; Takeuchi, T.; Goddard, W. A.; Shelnutt, J. A. *J. Am. Chem. Soc.* **1995**, *117*, 11085-11097.

(26) VERLET, L. *PHYSICAL REVIEW* **1967**, *159*, 98-&.

(27) Zerner, M. In *Reviews in Computational Chemistry*; VCH: New York, 1991; Vol. 2 (Eds. K. B. Lipkowitz and D. B. Boyd), p. 313.

(28) Shimoboji, T.; Larenas, E.; Fowler, T.; Kulkarni, S.; Hoffman, A. S.; Stayton, P. S. *Proceedings of the National Academy of Sciences of the United States of America* **2002**, *99*, 16592.

(29) Dargiewicz-Nowicka, J.; Makarska, M.; Villegas, M. A.; Legendziewicz, J.; Radzki, S. *Journal of Alloys and Compounds* **2004**, *380*, 380–388.

(30) http://pubs.acs.org/cen/science/87/8732scic5.html.

(31) Medforth, C.; Wang, Z.; Martin, K.; Song, Y.; Jacobsen, J.; Shelnutt, J. *CHEMICAL COMMUNICATIONS* **2009**, 7261-7277.

(32) SENGE, M. *PORPHYRIN HDB 1*, 239.

(33) RAVIKANTH, M.; CHANDRASHEKAR, T. K. *STRUCT BOND* **1995**, *82*, 105-188.

(34) DIMAGNO, S. G.; WERTSCHING, A. K.; ROSS, C. R. *J. Am. Chem. Soc.* **1995**, *117*, 8279-8280.

(35) Parusel, A. B. J.; Wondimagegn, T.; Ghosh, A. *J. Am. Chem. Soc.* **2000**, *122*, 6371-6374.

(36) WERTSCHING, A. K.; Koch, A. S.; DIMAGNO, S. G. *J. Am. Chem. Soc.* **2001**, *123*, 3932-3939.

(37) Ryeng, H.; Ghosh, A. *J. Am. Chem. Soc.* **2002**, *124*, 8099-8103.

(38) BARKIGIA, K. M.; CHANTRANUPONG, L.; Smith, K. M.; FAJER, J. *J. Am. Chem. Soc.* **1988**, *110*, 7566-7567.

(39) MEDFORTH, C. J.; SENGE, M. O.; Smith, K. M.; SPARKS, L. D.; Shelnutt, J. A. *J. Am. Chem. Soc.* **1992**, *114*, 9859-9869.

(40) MAYO, S. *J PHYS CHEM-US 94*, 88.

(41) Song, X. Z.; Jentzen, W.; Jaquinod, L.; Khoury, R. G.; MEDFORTH, C. J.; Jia, S. L.; Ma, J. G.; Smith, K. M.; Shelnutt, J. A. *Inorg. Chem.* **1998**, *37*, 2117-2128.

(42) Franco, R.; Ma, J. G.; Lu, Y.; Ferreira, G. C.; Shelnutt, J. A. *Biochemistry* **2000**, *39*, 2517-2529.

(43) HANSCH, C.; LEO, A.; TAFT, R. *CHEMICAL REVIEWS* **1991**, *91*, 165-195.

(44) MEDFORTH, C. J.; BERBER, M. D.; Smith, K. M.; Shelnutt, J. A. *Tetrahedron Lett.* **1990**, *31*, 3719-3722.

(45) SENGE, M. O.; MEDFORTH, C. J.; SPARKS, L. D.; Shelnutt, J. A.; Smith, K. M. *Inorg. Chem.* **1993**, *32*, 1716-1723.

(46) ALDEN, R. G.; CRAWFORD, B. A.; DOOLEN, R.; ONDRIAS, M. R.; Shelnutt, J. A. *J. Am. Chem. Soc.* **1989**, *111*, 2070-2072.

(47) Jentzen, W.; Unger, E.; Karvounis, G.; Shelnutt, J. A.; Dreybrodt, W.; SchweitzerStenner, R. *J. Phys. Chem.* **1996**, *100*, 14184-14191.

(48) BRENNAN, T. D.; SCHEIDT, W. R.; Shelnutt, J. A. *J. Am. Chem. Soc.* **1988**, *110*, 3919-3924.

(49) KUTZLER, F. W.; SWEPSTON, P. N.; BERKOVITCHYELLIN, Z.; ELLIS, D. E.; IBERS, J. A. *J. Am. Chem. Soc.* **1983**, *105*, 2996-3004.

(50) GALLUCCI, J. C.; SWEPSTON, P. N.; IBERS, J. A. *Acta Crystallogr. Sect. B-Struct. Commun.* **1982**, *38*, 2134-2139.

(51) Ulman, A.; Gallucci, J.; Fisher, D.; IBERS, J. A. *J. Am. Chem. Soc.* **1980**, *102*, 6852-6854.

(52) NELSON, N. *THESIS U CALIFORNIA*.

(53) SENGE, M. O.; Bischoff, I.; NELSON, N. Y.; Smith, K. M. *J. Porphyr. Phthalocyanines* **1999**, *3*, 99-116.

(54) SENGE, M. O.; Ema, T.; Smith, K. M. *J. Chem. Soc.-Chem. Commun.* **1995**, 733-734.

(55) Haddad, R. E.; Gazeau, S.; Pecaut, J.; MARCHON, J. C.; MEDFORTH, C. J.; Shelnutt, J. A. *J. Am. Chem. Soc.* **2003**, *125*, 1253-1268.

(56) HOARD, J. *PORPHYRINS METALLOPO* 317.

(57) Roberts, S. A.; Weichsel, A.; Qiu, Y.; Shelnutt, J. A.; Walker, F. A.; Montfort, W. R. *Biochemistry* **2001**, *40*, 11327-11337.

(58) STREITWIESER, J. *MOL ORBITAL THEORY O*.

(59) GAZEAU, S. *CHEM COMMUN 0907* 1644.

(60) Haddad, R. E.; Gazeau, S.; Pecaut, J.; MARCHON, J. C.; MEDFORTH, C. J.; Shelnutt, J. A. *J. Am. Chem. Soc.* **2003**, *125*, 1253-1268.

(61) Song, Y.; Haddad, R.; Jia, S.; Hok, S.; Olmstead, M.; Nurco, D.; Schore, N.; Zhang, J.; Ma, J.; Smith, K.; Gazeau, S.; Pecaut, J.; Marchon, J.; Medforth, C.; Shelnutt, J. *JOURNAL OF THE AMERICAN CHEMICAL SOCIETY* **2005**, *127*, 1179-1192.

(62) MEDFORTH, C. *J CHEM SOC PERK APR* 839.

(63) SOMMA, M. *CHEM COMMUN 0707* 1221.

(64) SPAULDING, L. D.; Chang, C. C.; YU, N. T.; FELTON, R. H. *J. Am. Chem. Soc.* **1975**, *97*, 2517-2525.

(65) KIM, D.; HOLTEN, D. *CHEMICAL PHYSICS LETTERS* **1983**, *98*, 584-589.

(66) KIM, D.; KIRMAIER, C.; HOLTEN, D. *CHEMICAL PHYSICS* **1983**, *75*, 305-322.

(67) SPARKS, L. D.; MEDFORTH, C. J.; Park, M. S.; Chamberlain, J. R.; ONDRIAS, M. R.; SENGE, M. O.; Smith, K. M.; Shelnutt, J. A. *J. Am. Chem. Soc.* **1993**, *115*, 581-592.

(68) Song, X. Z.; Jaquinod, L.; Jentzen, W.; Nurco, D. J.; Jia, S. L.; Khoury, R. G.; Ma, J. G.; MEDFORTH, C. J.; Smith, K. M.; Shelnutt, J. A. *Inorg. Chem.* **1998**, *37*, 2009-2019.

(69) Shelnutt, J. A.; MEDFORTH, C. J.; BERBER, M. D.; BARKIGIA, K. M.; Smith, K. M. *J. Am. Chem. Soc.* **1991**, *113*, 4077-4087.

(70) Maclean, A. L.; Foran, G. J.; Kennedy, B. J.; Turner, P.; Hambley, T. W. *Aust. J. Chem.* **1996**, *49*, 1273-1278.

(71) KIRNER, J. F.; GAROFALO, J.; SCHEIDT, W. R. *INORG NUCL CHEM LETT* **1975**, *11*, 107-112.

(72) SENGE, M. O. *J. Porphyr. Phthalocyanines* **1998**, *2*, 107-121.

(73) Duval, H.; Bulach, V.; Fischer, J.; Weiss, R. *Inorg. Chem.* **1999**, *38*, 5495-5501.

(74) MEDFORTH, C. J.; Muzzi, C. M.; Smith, K. M.; ABRAHAM, R. J.; HOBBS, J. D.; Shelnutt, J. A. *J. Chem. Soc.-Chem. Commun.* **1994**, 1843-1844.

(75) SPARKS, L. D.; MEDFORTH, C. J.; Park, M. S.; Chamberlain, J. R.; ONDRIAS, M. R.; SENGE, M. O.; Smith, K. M.; Shelnutt, J. A. *J. Am. Chem. Soc.* **1993**, *115*, 581-592.

(76) Ulman, A.; Gallucci, J.; Fisher, D.; IBERS, J. A. *J. Am. Chem. Soc.* **1980**, *102*, 6852-6854.

(77) Shelnutt, J. A. *J. Phys. Chem.* **1983**, *87*, 605-616.

(78) Franco, R.; Ma, J. G.; Lu, Y.; Ferreira, G. C.; Shelnutt, J. A. *Biochemistry* **2000**, *39*, 2517-2529.

(79) Medforth, C.; Haddad, R.; Muzzi, C.; Dooley, N.; Jaquinod, L.; Shyr, D.; Nurco, D.; Olmstead, M.; Smith, K.; Ma, J.; Shelnutt, J. *INORGANIC CHEMISTRY* **2003**, *42*, 2227-2241.

(80) MEDFORTH, C. J.; Muzzi, C. M.; Smith, K. M.; ABRAHAM, R. J.; HOBBS, J. D.; Shelnutt, J. A. *J. Chem. Soc.-Chem. Commun.* **1994**, 1843-1844.

(81) MEDFORTH, C. *J CHEM SOC PERK APR* 833.

(82) Jentzen, W.; Song, X. Z.; Shelnutt, J. A. *J. Phys. Chem. B* **1997**, *101*, 1684-1699.

(83) FLACK, H. D. *Acta Crystallogr. Sect. A* **1983**, *39*, 876-881.

(84) Renner, M. W.; Furenlid, L. R.; BARKIGIA, K. M.; FAJER, J. *J. Phys. IV* **1997**, *7*, 661-662.

(85) Jentzen, W.; SIMPSON, M. C.; HOBBS, J. D.; Song, X.; Ema, T.; NELSON, N. Y.; MEDFORTH, C. J.; Smith, K. M.; VEYRAT, M.; MAZZANTI, M.; RAMASSEUL, R.; MARCHON, J. C.; Takeuchi, T.; Goddard, W. A.; Shelnutt, J. A. *J. Am. Chem. Soc.* **1995**, *117*, 11085-11097.

(86) VEYRAT, M.; RAMASSEUL, R.; MARCHON, J. C.; TUROWSKATYRK, I.; SCHEIDT, W. R. *New J. Chem.* **1995**, *19*, 1199-1202.

(87) SENGE, M. O.; Bischoff, I.; NELSON, N. Y.; Smith, K. M. *J. Porphyr. Phthalocyanines* **1999**, *3*, 99-116.

(88) Ema, T.; SENGE, M. O.; NELSON, N. Y.; OGOSHI, H.; Smith, K. M. *Angew. Chem.-Int. Edit. Engl.* **1994**, *33*, 1879-1881.

(89) Drain, C. M.; Gentemann, S.; Roberts, J. A.; NELSON, N. Y.; MEDFORTH, C. J.; Jia, S. L.; SIMPSON, M. C.; Smith, K. M.; FAJER, J.; Shelnutt, J. A.; Holten, D. *J. Am. Chem. Soc.* **1998**, *120*, 3781-3791.

(90) Jia, S. L.; Jentzen, W.; Shang, M.; Song, X. Z.; Ma, J. G.; SCHEIDT, W. R.; Shelnutt, J. A. *Inorg. Chem.* **1998**, *37*, 4402-4412.

(91) WERTSCHING, A. K.; Koch, A. S.; DIMAGNO, S. G. *J. Am. Chem. Soc.* **2001**, *123*, 3932-3939.

(92) Ryeng, H.; Ghosh, A. *J. Am. Chem. Soc.* **2002**, *124*, 8099-8103.

(93) MACCRAGH, A.; STORM, C. B.; KOSKI, W. S. *J. Am. Chem. Soc.* **1965**, *87*, 1470-&.

(94) MCLEES, B. D.; CAUGHEY, W. S. *Biochemistry* **1968**, *7*, 642-&.

(95) Song, X. Z.; Jentzen, W.; Jaquinod, L.; Khoury, R. G.; MEDFORTH, C. J.; Jia, S. L.; Ma, J. G.; Smith, K. M.; Shelnutt, J. A. *Inorg. Chem.* **1998**, *37*, 2117-2128.

(96) ABRAHAM, R. *J CHEM SOC B 8*, 903.

(97) Walker, F. A.; HUI, E.; Walker, J. M. *J. Am. Chem. Soc.* **1975**, *97*, 2390-2397.

(98) Shelnutt, J. A.; MAJUMDER, S. A.; SPARKS, L. D.; HOBBS, J. D.; MEDFORTH, C. J.; SENGE, M. O.; Smith, K. M.; Miura, M.; Luo, L.; QUIRKE, J. M. E. *J. Raman Spectrosc.* **1992**, *23*, 523-529.

(99) Song, X. Z.; Jentzen, W.; Jia, S. L.; Jaquinod, L.; Nurco, D. J.; MEDFORTH, C. J.; Smith, K. M.; Shelnutt, J. A. *J. Am. Chem. Soc.* **1996**, *118*, 12975-12988.

(100) Shelnutt, J. A.; Song, X. Z.; Ma, J. G.; Jia, S. L.; Jentzen, W.; MEDFORTH, C. J. *Chem. Soc. Rev.* **1998**, *27*, 31-41.

(101) Kim, D.; SPIRO, T. G. *J. Am. Chem. Soc.* **1986**, *108*, 2099-2100.

(102) Kim, D.; Miller, L. A.; SPIRO, T. G. *Inorg. Chem.* **1986**, *25*, 2468-2470.

(103) Shelnutt, J. A. *J. Am. Chem. Soc.* **1987**, *109*, 4169-4173.

(104) Jentzen, W.; Unger, E.; Song, X. Z.; Jia, S. L.; TUROWSKATYRK, I.; SchweitzerStenner, R.; Dreybrodt, W.; SCHEIDT, W. R.; Shelnutt, J. A. *J. Phys. Chem. A* **1997**, *101*, 5789-5798.

(105) GAZEAU, S. *CHEM COMMUN 0907* 1644.

(106) Jentzen, W.; Ma, J. G.; Shelnutt, J. A. *Biophys. J.* **1998**, *74*, 753-763.

(107) HOBBS, J. D.; Shelnutt, J. A. *J. Protein Chem.* **1995**, *14*, 19-25.

(108) Retsek, J. L.; Drain, C. M.; Kirmaier, C.; Nurco, D. J.; MEDFORTH, C. J.; Smith, K. M.; Sazanovich, I. V.; Chirvony, V. S.; FAJER, J.; Holten, D. *J. Am. Chem. Soc.* **2003**, *125*, 9787-9800.

(109) DESBOIS, A.; MOMENTEAU, M.; Lutz, M. *Inorg. Chem.* **1989**, *28*, 825-834.

(110) David, S.; JAMES, B. R.; Dolphin, D.; TRAYLOR, T. G.; Lopez, M. A. *J. Am. Chem. Soc.* **1994**, *116*, 6-14.

(111) Kottas, G.; Clarke, L.; Horinek, D.; Michl, J. *CHEMICAL REVIEWS* **2005**, *105*, 1281-1376.

(112) Drain, C. M.; Kirmaier, C.; MEDFORTH, C. J.; Nurco, J.; Smith, K. M.; Holten, D. *J. Phys. Chem.* **1996**, *100*, 11984-11993.

(113) Retsek, J. L.; Gentemann, S.; MEDFORTH, C. J.; Smith, K. M.; Chirvony, V. S.; FAJER, J.; Holten, D. *J. Phys. Chem. B* **2000**, *104*, 6690-6693.

(114) Retsek, J. L.; MEDFORTH, C. J.; Nurco, D. J.; Gentemann, S.; Chirvony, V. S.; Smith, K. M.; Holten, D. *J. Phys. Chem. B* **2001**, *105*, 6396-6411.

(115) MEDFORTH, C. J.; Smith, K. M. *Tetrahedron Lett.* **1990**, *31*, 5583-5586.

(116) Tsuchiya, S. *Chem. Phys. Lett.* **1990**, *169*, 608-610.

(117) Takeda, J.; Ohya, T.; Sato, M. *Chem. Phys. Lett.* **1991**, *183*, 384-386.

(118) Tsuchiya, S. *J. Chem. Soc.-Chem. Commun.* **1991**, 716-717.

(119) Takeda, J.; Ohya, T.; Sato, M. *Inorg. Chem.* **1992**, *31*, 2877-2880.

(120) TSUCHIYA, S. *J CHEM SOC CHEM 1001* 1475.

(121) MEDFORTH, C. J.; SENGE, M. O.; Smith, K. M.; SPARKS, L. D.; Shelnutt, J. A. *J. Am. Chem. Soc.* **1992**, *114*, 9859-9869.

(122) Charlesworth, P.; TRUSCOTT, T. G.; Kessel, D.; MEDFORTH, C. J.; Smith, K. M. *J. Chem. Soc.-Faraday Trans.* **1994**, *90*, 1073-1076.

(123) Takeda, J.; Sato, M. *Chem. Lett.* **1995**, 971-972.

(124) Takeda, J.; Sato, M. *Chem. Lett.* **1995**, 939-940.

(125) Nurco, D. J.; MEDFORTH, C. J.; Forsyth, T. P.; Olmstead, M. M.; Smith, K. M. *J. Am. Chem. Soc.* **1996**, *118*, 10918-10919.

(126) Clement, T. E.; Nguyen, L. T.; Khoury, R. G.; Nurco, D. J.; Smith, K. M. *Heterocycles* **1997**, *45*, 651-658.

(127) Guilard, R.; Perie, K.; Barbe, J. M.; Nurco, D. J.; Smith, K. M.; Van Caemelbecke, E.; Kadish, K. M. *Inorg. Chem.* **1998**, *37*, 973-981.

(128) Kadish, K. M.; Van Caemelbecke, E.; D'Souza, F.; Lin, M.; Nurco, D. J.; MEDFORTH, C. J.; Forsyth, T. P.; Krattinger, B.; Smith, K. M.; Fukuzumi, S.; Nakanishi, I.; Shelnutt, J. A. *Inorg. Chem.* **1999**, *38*, 2188-2198.

(129) Muzzi, C. M.; MEDFORTH, C. J.; Voss, L.; Cancilla, M.; Lebrilla, C.; Ma, J. G.; Shelnutt, J. A.; Smith, K. M. *Tetrahedron Lett.* **1999**, *40*, 6159-6162.

(130) Kadish, K. M.; Lin, M.; Van Caemelbecke, E.; De Stefano, G.; MEDFORTH, C. J.; Nurco, D. J.; NELSON, N. Y.; Krattinger, B.; Muzzi, C. M.; Jaquinod, L.; Xu, Y.; Shyr, D. C.; Smith, K. M.; Shelnutt, J. A. *Inorg. Chem.* **2002**, *41*, 6673-6687.

(131) EATON, S. S.; EATON, G. R. *J. Am. Chem. Soc.* **1977**, *99*, 6594-6599.

(132) DIRKS, J. W.; Underwood, G.; MATHESON, J. C.; Gust, D. *J. Org. Chem.* **1979**, *44*, 2551-2555.

(133) Walker, F. A.; AVERY, G. L. *Tetrahedron Lett.* **1971**, 4949-&.

(134) EATON, S. S.; EATON, G. R. *J. Chem. Soc.-Chem. Commun.* **1974**, 576-577.

(135) EATON, S. S.; EATON, G. R. *J. Am. Chem. Soc.* **1975**, *97*, 3660-3666.

(136) CROSSLEY, M. J.; FIELD, L. D.; Forster, A. J.; HARDING, M. M.; STERNHELL, S. *J. Am. Chem. Soc.* **1987**, *109*, 341-348.

(137) Takeda, J.; Sato, M. *Chem. Pharm. Bull.* **1994**, *42*, 1005-1007.

(138) FREITAG, R. A.; WHITTEN, D. G. *J. Phys. Chem.* **1983**, *87*, 3918-3925.

(139) Takeda, J.; Ohya, T.; Sato, M. *Chem. Pharm. Bull.* **1990**, *38*, 264-266.

(140) Barkigia, K.; Nurco, D.; Renner, M.; Melamed, D.; Smith, K.; Fajer, J. *JOURNAL OF PHYSICAL CHEMISTRY B* **1998**, *102*, 322-326.

(141) BRENNAN, T. D.; SCHEIDT, W. R.; Shelnutt, J. A. *J. Am. Chem. Soc.* **1988**, *110*, 3919-3924.

(142) ALDEN, R. G.; CRAWFORD, B. A.; DOOLEN, R.; ONDRIAS, M. R.; Shelnutt, J. A. *J. Am. Chem. Soc.* **1989**, *111*, 2070-2072.

(143) MEDFORTH, C. *J CHEM SOC PERK APR* 833.

(144) GONG, L.; DOLPHIN, D. *CANADIAN JOURNAL OF CHEMISTRY-REVUE CANADIENNE DE CHIMIE* **1985**, *63*, 401-405.

(145) BHYRAPPA, P.; Krishnan, V. *Inorg. Chem.* **1991**, *30*, 239-245.

(146) OCHSENBEIN, P.; AYOUGOU, K.; MANDON, D.; FISCHER, J.; WEISS, R.; AUSTIN, R.; JAYARAJ, K.; GOLD, A.; TERNER, J.; FAJER, J. *ANGEWANDTE CHEMIE-INTERNATIONAL EDITION IN ENGLISH* **1994**, *33*, 348-350.

(147) MANDON, D.; OCHSENBEIN, P.; FISCHER, J.; WEISS, R.; JAYARAJ, K.; AUSTIN, R.; GOLD, A.; WHITE, P.; BRIGAUD, O.; BATTIONI, P.; MANSUY, D. *INORGANIC CHEMISTRY* **1992**, *31*, 2044-2049.

(148) Woller, E.; DiMagno, S. *JOURNAL OF ORGANIC CHEMISTRY* **1997**, *62*, 1588-1593.

(149) MERZ, A.; SCHROPP, R.; LEX, J. *ANGEWANDTE CHEMIE-INTERNATIONAL EDITION IN ENGLISH* **1993**, *32*, 291-293.

(150) BIRNBAUM, E.; HEDGE, J.; GRINSTAFF, M.; SCHAEFER, W.; HENLING, L.; LABINGER, J.; BERCAW, J.; GRAY, H. *INORGANIC CHEMISTRY* **1995**, *34*, 3625-3632.

(151) BYRN, M.; CURTIS, C.; HSIOU, Y.; KHAN, S.; SAWIN, P.; TENDICK, S.; TERZIS, A.; STROUSE, C. *JOURNAL OF THE AMERICAN CHEMICAL SOCIETY* **1993**, *115*, 9480-9497.

(152) SENGE, M. O.; Renner, M. W.; Kalisch, W. W.; FAJER, J. *J. Chem. Soc.-Dalton Trans.* **2000**, 381-385.

(153) NELSON, N. Y.; MEDFORTH, C. J.; Nurco, D. J.; Jia, S. L.; Shelnutt, J. A.; Smith, K. M. *Chem. Commun.* **1999**, 2071-2072.

(154) SENGE, M. *J CHEM SOC DA* 3539.

(155) HOBBS, J. D.; MAJUMDER, S. A.; Luo, L.; SICKELSMITH, G. A.; QUIRKE, J. M. E.; MEDFORTH, C. J.; Smith, K. M.; Shelnutt, J. A. *J. Am. Chem. Soc.* **1994**, *116*, 3261-3270.

APPENDICES

Appendix A

This appendix contains supplemental information for Chapter 3.

Table A-1 Absorption Maxima (λ_{max}, nm; in CH_2Cl_2 unless stated) and Out-of-plane Deformations (d_{total}, Å) for Sterically Crowded Free Base Porphyrins.

Porphyrin	$B_{(0,0)}$	$Q_{X(0,0)}$	d_{total}	$\Sigma\sigma_p$	Ref.
OETPP	456	706	3.511	-1.24	61
OET(NO_2)P	426	666	2.535 - 3.127	+1.92	144
Br_8TPP	469	743	3.856	+1.80	145
Cl_8TMsP	463	717	2.906	n/a	146
Br_8TMsP	465	n/o	3.012	n/a	147
Cl_8F_{20}TPP	436	n/o	1.915	+2.92	148
Br_8F_{20}TPP	453	n/o	2.750	+2.92	147
T(tBu)P	446	691	2.794	-0.80	87
DPP	468	724	3.034 - 3.901	-0.12	121
$(OMe)_{20}$DPP	472	718	3.260	n/a	130
F_8DPP (meso)	452	689	2.097	n/a	128
F_{20}DPP	444	n/o	2.383	+1.00	128
F_{28}DPP	442	n/o	0.660[a]	+1.56	128
RANGES	**426- 472**	**666- 743**	**1.915-3.901**	**-1.24/ +2.92**	

[a] The unusually small amount of total nonplanar deformation displayed in this crystal structures is a result of the distortion occurring in a high energy deformation mode (waving). MM calculations indicate that this is not the minimum energy structure, suggesting that the crystal structure may be the result of packing forces. This compound was therefore excluded when calculating the ranges.

Table A-2 Absorption Maxima (λ_{max}, nm ; in CH_2Cl_2) and Out-of-plane Deformations (d_{total}, Å) for Uncrowded Free Base Porphyrins.

Porphyrin	$B_{(0,0)}$	$Q_{X(0,0)}$	d_{total}	$\Sigma\sigma_p$	Ref.
P	394	613	0.084-0.104	0.00	[148]
O(OMe)P (toluene)	377	618	0.127	-2.16	[149]
OEP	400	622	0.126	-1.20	[149]
T(Bu)P	417	659	0.120	-0.64	[87]
T(Pe)P	416	658	0.509	-0.60	[52]
T(iPr)P	420	658	1.207	-0.60	[87]
TPP	418	646	0.046-1.082	-0.04	[148]
F_{20}TPP	412	638	0.053-0.080	+1.08	[148,150,151]
RANGES	**377-420**	**613-659**	**0.046-1.207**	**-2.16/+1.08**	

Table A-3 Absorption Maxima (λ_{max}, nm; in CH_2Cl_2 unless stated) and Out-of-plane Deformations (d_{total}, Å) for Sterically Crowded Nickel Porphyrins

Porphyrin	$B_{(0,0)}$	$Q_{(0,0)}$	d_{total}	$\Sigma\sigma_p$	Ref.
TC6TPP	424	579	3.320	-1.24	61
T(Bu)OEP	459	635	2.844	-1.80	152
T(OCOPh)OEP	424	583	2.291	-0.68	130
$Br_8T(CF_3)P$	444	690	2.880	+4.00	153
OETPP	432	588	3.817	-1.24	61
OPrTPP	434	590	3.955 - 4.003	-1.24	22
$F_{20}OETPP$	426	595	3.567	-0.12	130
Br_8TMP (in $CHCl_3$)	449	593	3.315	n/a	147
$Br_8F_{20}TPP$	436	600	3.631 - 3.663	+2.92	147
OETNP	416	585	3.010 - 3.312	+1.92	154,155
DPP	449	613	2.435 - 3.550	-0.12	22
F_8DPP	446	610	2.499 - 3.208	+0.44	130
F_8DPP (meso)	436	598	2.374	n/a	130
$F_{20}DPP$	432	596	2.682 - 3.382	+1.00	130
$F_{28}DPP$	432	596	3.136	+1.56	130
$F_{36}DPP$	434	595	2.287	n/a	130
$(OMe)_{20}DPP$	452	612	3.229	n/a	79
RANGES	**416-459**	**579-690**	**2.287-4.003**	**-1.80/+4.00**	

Table A-4 Absorption Maxima (λ_{max}, nm; in CH_2Cl_2) and Out-of-plane Deformations (d_{total}, Å) for Sterically Uncrowded Nickel Porphyrins.

Porphyrin	$B_{(0,0)}$	$Q_{(0,0)}$	d_{total}	$\Sigma\sigma_p$	Ref.
P	385	536	0.094	0.00	[22]
OEP	391	551	0.087-1.461	-1.20	[22]
TPP	414	557	1.295	-0.04	[61]
T(Me)P	416	n/o	0.296	-1.20	[49-51]
T(iPr)P	423	586	2.085	-0.60	[87]
T(cyclohexyl)P	425	586	2.143	-0.60	[86]
TC5TC5P	422	582	2.238	-1.80	[121]
TC5T(3,4,5-OMeP)P	408	554	2.153	n/a	[61]
RANGES	**385-425**	**536-586**	**0.087-2.238**	**-1.80/0.00**	

Table A-5 In-plane Totally Symmetric Deformations for Nickel Tetraalkylporphyrin Molecular Mechanics Structures (Å).

Entry	Compound	d_{total}	tot A_{1g}	$1A_{1g}$	$2A_{1g}$	$3A_{1g}$	$4A_{1g}$	$5A_{1g}$	$6A_{1g}$
1A	T(Me)P	0.5493	0.5491	-0.5096	0.1576	0.0200	-0.0950	-0.0282	0.0755
1B	T(tBu)P	1.1071	1.1071	-0.9679	0.4729	0.1011	-0.1141	-0.0627	0.1330
2	T(Me)P	1.1071[a]	1.1071	-0.9679	0.4729	0.1011	-0.1141	-0.0627	0.1330
3A	T(Me)P	0.9680	0.9679	-0.8548	0.3804	0.0634	-0.1886	-0.0193	0.1199
3B	T(Me)P	1.0732	1.0732	-0.9406	0.4355	0.0731	-0.2141	-0.0154	0.1297
4A	T(Me)P	1.0708	1.0708	-0.9389	0.4283	0.0667	-0.2296	-0.0129	0.1257
4B	T(Me)P	1.0970	1.0969	-0.9867	0.3806	0.0854	-0.2110	-0.0040	0.1471
4C	T(Me)P	0.1904	0.1900	-0.1497	-0.1050	-0.0316	-0.0398	-0.0194	0.0229
4D	T(tBu)P	0.3514	0.3119	-0.0502	-0.2919	-0.0360	-0.0844	-0.0153	0.0373
5	T(Me)P	0.9680[b]	0.9679	-0.8548	0.3804	0.0634	-0.1886	-0.0193	0.1199
6A	T(Me)P	1.3353	1.3353	-1.1290	0.6407	0.1103	-0.2270	-0.0506	0.1787
6B	19	1.1388	1.1365	-0.9758	0.5189	0.1067	-0.1403	-0.0675	0.1510
6C	T(Me)P	1.1154	1.1153	-0.9548	0.5132	0.1017	-0.1402	-0.0684	0.1530
7	T(Me)P	1.1234	1.1233	-0.9620	0.5163	0.1026	-0.1410	-0.0686	0.1536

[a] Same as entry 1B (core unchanged).

[b] Same as entry 3A (core unchanged).

Table A-6 In-plane Totally Symmetric Deformations for Zinc Tetraalkylporphyrin Molecular Mechanics Structures (Å).

Entry	Compound	d_{total}	tot A_{1g}	$1A_{1g}$	$2A_{1g}$	$3A_{1g}$	$4A_{1g}$	$5A_{1g}$	$6A_{1g}$
1A	T(Me)P	0.1020	0.1009	0.0562	-0.0390	0.0476	-0.0450	-0.0020	0.0384
1B	T(tBu)P	0.5448	0.5448	-0.4236	0.2830	0.1312	-0.0518	-0.0429	0.0991
2	T(Me)P	0.5448[a]	0.5448	-0.4236	0.2830	0.1312	-0.0518	-0.0429	0.0991
3A	T(Me)P	0.3970	0.3970	-0.2940	0.1917	0.0927	-0.1256	0.0024	0.0838
5	T(Me)P	0.3970[b]	0.3970	-0.2940	0.1917	0.0927	-0.1256	0.0024	0.0838
6B	19	0.6948	0.6917	-0.5053	0.4054	0.1539	-0.0749	-0.0600	0.1329
6C	T(Me)P	0.5736	0.5736	-0.4104	0.3374	0.1354	-0.0736	-0.0504	0.1208
7	T(Me)P	0.5815	0.5818	-0.4183	0.3404	0.1366	-0.0735	-0.0516	0.1220

[a] Same as entry 1B (core unchanged).
[b] Same as entry 3A (core unchanged).

Table A-7 NSD Analysis of the Out-of-plane Deformations (in Å) of Molecules in the X-ray Crystal Structures of the Bridled Nickel Chiroporphyrins 12a (M = Ni) and 12c (M = Ni).

Comp	Crystal Lattice[a]	Mol	d_{total}	d_{sad} (B_{2u})	d_{ruf} (B_{1u})	d_{dom} (A_{2u})	$d_{wav(x)}$ ($E_{g(x)}$)	$d_{wav(y)}$ ($E_{g(Y)}$)	d_{pro} (A_{1u})
12a	or	A	1.827	0.416	-1.778	0.021	0.046	0.026	0.020
		B	1.889	0.697	-1.753	-0.031	0.017	0.083	0.033
	mc	A	1.962	-0.502	1.893	0.066	0.096	0.022	0.035
		B	1.954	-0.205	-1.939	0.066	0.075	-0.063	0.038
12c	or	A	2.105	-0.829	-1.934	-0.014	0.004	0.047	-0.015
		B	1.664	0.000	1.664	0.000	0.000	-0.004	0.006
	mc	A	1.673	-0.008	1.673	-0.020	-0.013	0.032	0.000
		B	2.047	0.503	-1.983	-0.009	0.031	-0.016	0.042
		C	2.103	-0.823	1.934	-0.020	0.050	0.018	0.004

[a] or = orthorhombic; mc = monoclinic

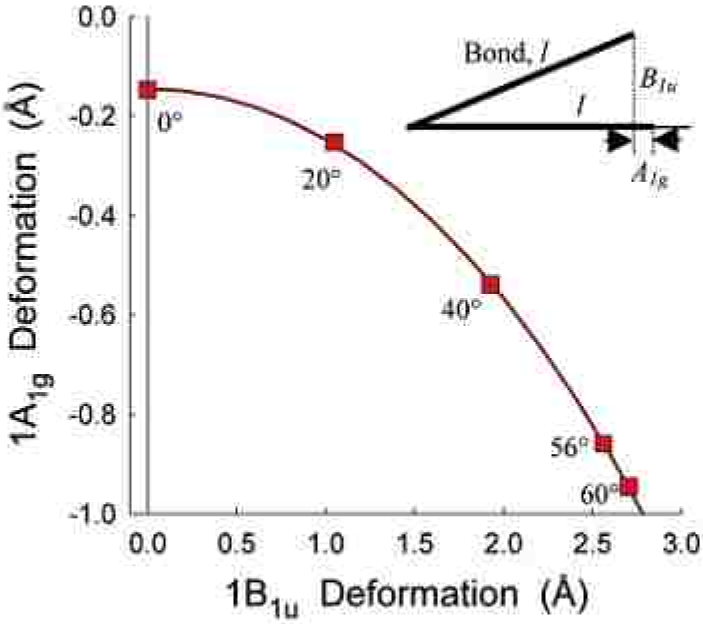

Figure A-1. Illustration of the geometric relationship between $1B_{1u}$ out-of-plane and $1A_{1g}$ in-plane deformations of the porphyrin macrocycle using the structures of nickel tetramethylporphyrin constrained to various ruffling angles (0°,20°,40°,56°,60°) as calculated by molecular mechanics. The expression used to fit the data relates the contraction of the projection of a rigid bond into the mean plane of the porphyrin to the out-of-plane displacement of an atom of the bond. The expression obtained from simple trigonometric relationships is

$$A_{1g} = A_0 - l + \sqrt{l^2 - {B_{1u}}^2},$$

where l is a fitting parameter interpreted as an effective radial bond length for the macrocycle and A_0 is the metal-induced contraction of the planar porphyrin relative to a reference Cu(II) porphine. The values of the fitting parameters l and A_0 for the nickel porphyrin curve shown are 4.957 Å and 0.145 Å (the small Ni(II) ion induces a small core contraction even when the porphyrin is planar).

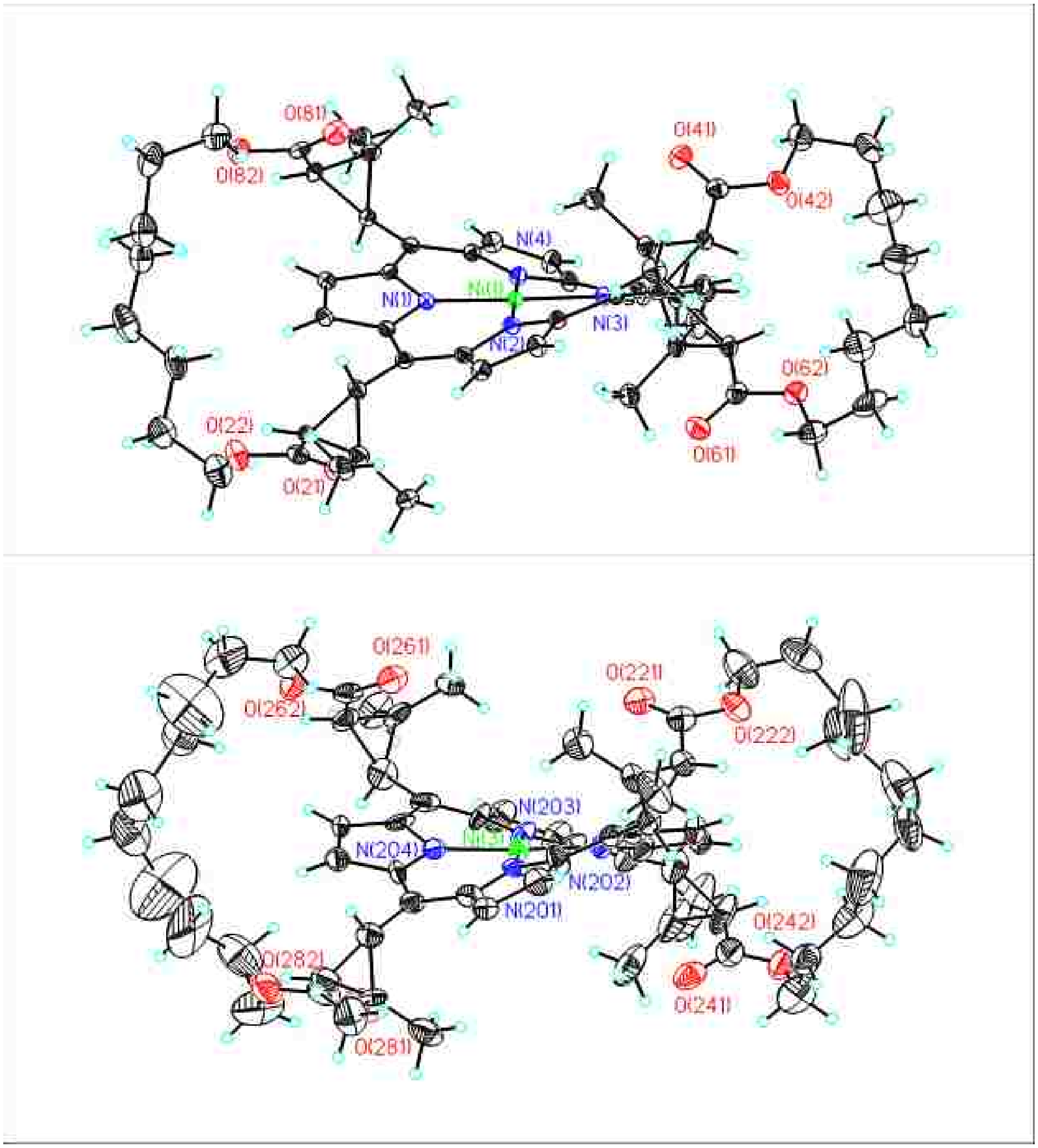

Figure A-2 ORTEP views of selected molecules from the X-ray structures[55] of crystals of the bridled chiroporphyrins:
Upper- orthorhombic 12a (M=Ni); Lower- monoclinic 12c (M=Ni).
The crystal structures confirm the αβαβ stereochemistry of the substituents and illustrate how the alkyl chains wrap around the edge of the porphyrin.

Appendix B

This appendix contains supplemental information for Chapter 4.

Table B-1. Energies (kcal mol^{-1}) of stable conformers calculated for the low-spin 4-coordinate nickel tetraalkylporphyrins.

Porphyrin Conformer	rel. E	total[a]	bond	angle	torsn	inversn	van der Waals	electro
TPP								
ruf	0	180.72	9.56	70.59	47.49	0.65	60.14	-7.71
sad	1.69	182.41	11.74	72.25	41.38	0.25	64.45	-7.64
planar	1.78	182.50	12.50	72.20	40.00	0.00	65.50	-7.63
T(Et)P								
αβαβ_jiji[b]	0	128.21	6.21	73.62	12.92	0.82	27.47	7.18
αβαβ_ijjj	1.28	129.39	6.12	73.61	14.26	0.80	27.41	7.18
αβαβ_iiii	2.36	130.57	6.05	73.63	15.53	0.78	27.39	7.19
αβαβ_iijj	2.37	130.58	6.06	73.64	15.46	0.78	27.45	7.19
αααα	6.15	134.36	8.86	76.41	7.62	0.67	33.56	7.25
ααββ	6.15	134.36	8.93	76.39	7.49	0.62	33.67	7.26
T(Pr)P								
αβαβ_jiji	0	131.26	6.94	73.94	12.63	0.82	32.22	4.72
αβαβ_ijjj	1.38	132.64	6.82	73.91	14.13	0.80	32.16	4.82
αβαβ_iiii	2.76	134.02	6.76	73.91	15.41	0.78	32.24	4.91
αβαβ_iijj	2.79	134.05	6.76	73.92	15.43	0.77	32.24	4.93
αααα_*sad*	6.36	137.62	9.49	76.73	7.64	0.68	38.09	4.98
ααββ_*sad*	6.35	137.61	9.61	76.71	7.43	0.60	38.26	4.99
ααββ_*wav*	6.59	137.85	10.67	76.72	5.66	0.13	39.66	5.01
T(Pe)P								
αβαβ_jiji	0	144.82	8.16	75.06	12.64	0.83	41.95	6.18
αβαβ_ijjj	1.36	146.18	8.02	75.02	14.26	0.80	41.82	6.25
αβαβ_iiii	2.70	147.52	7.98	75.04	15.47	0.78	41.95	6.32
αβαβ_iijj	2.76	147.58	7.98	75.04	15.43	0.77	42.00	6.35
αααα_*sad*	6.24	151.06	10.70	77.87	7.64	0.69	47.78	6.37
ααββ_*sad*	6.25	151.07	10.78	77.86	7.48	0.64	47.94	6.42
ααββ_*wav*	6.50	151.32	11.91	77.86	5.60	0.13	49.41	6.42
T(Me)P								
αβαβ	0	115.96	4.55	71.36	14.08	1.03	23.88	1.06
αααα_*sad*	8.14	124.10	8.13	74.81	8.02	0.20	31.67	1.26
αααα_*dom*	8.15	124.11	8.35	74.78	7.78	0.07	31.85	1.28
ααββ	7.93	123.89	7.98	74.60	8.52	0.22	31.32	1.26
T(cPr)P								
αβαβ	0	626.92	4.47	561.86	33.58	1.08	19.83	6.10
αααβ	4.44	631.36	5.58	563.31	32.94	0.90	22.51	6.10
αααα	8.02	634.94	7.87	564.75	30.01	0.13	25.99	6.19
ααββ	7.99	634.91	7.52	564.63	30.63	0.30	25.63	6.19

T(iPr)P								
αβαβ	0	139.03	8.19	80.12	22.23	0.83	33.66	-6.01
αααα_*sad*	13.75	152.78	11.66	85.24	20.60	0.60	40.44	-5.76
αααα_*dom*	13.92	152.95	12.18	85.10	20.52	0.12	40.76	-5.72
ααββ	13.30	152.33	11.51	84.76	21.21	0.50	40.08	-5.72
T(cH)P								
αβαβ	0	171.25	11.83	82.00	23.38	0.85	54.39	-1.20
αααα	14.85	186.10	15.82	87.06	22.67	0.14	61.41	-1.02
ααββ	14.17	185.42	15.13	86.72	23.25	0.58	60.76	-1.02
T(tBu)P								
αβαβ	0	164.36	17.59	85.84	39.36	0.60	56.76	-35.80
αααβ	11.87	176.23	17.52	87.74	46.50	1.49	58.77	-35.80
αααα	19.54	183.90	18.82	88.52	53.13	0.66	58.49	-35.71
ααββ	21.90	186.26	19.25	89.87	50.57	1.64	60.61	-35.68

[a] In all cases, the energy from the hydrogen bonding term was zero.

[b] Secondary conformations were obtained for the primary alkyl groups due to the different positions possible for the second carbon in the alkyl chain; i and j are used to specify the relative orientations of the second carbons in the alkyl chain.

Table B-2. Out-of-plane displacements (in Å) obtained from normal-coordinate structural decomposition of stable conformers calculated for the low-spin 4-coordinate nickel tetraalkylporphyrins.

Porphyrin Conformer	total		*sad*[c]	*ruf*	*dom*	*wav(x)*	*wav(y)*
	observed[a]	fit[b]					
TPP							
ruf	1.482	1.479	0.005	1.479	0.000	0.000	0.000
sad	1.091	1.090	1.090	0.027	0.000	0.000	0.000
planar	0.023	0.023	0.023	0.003	0.000	0.000	0.000
T(Et)P							
αβαβ_jiji[d]	1.812	1.808	0.000	1.808	0.000	0.000	0.000
αβαβ_ijjj	1.865	1.860	0.049	1.858	0.038	0.038	0.050
αβαβ_iiii	1.917	1.911	0.088	1.908	0.073	0.000	0.000
αβαβ_iijj	1.912	1.907	0.004	1.904	0.000	0.092	0.000
αααα_*sad*	1.670	1.663	1.649	0.000	0.209	0.000	0.000
ααββ_*sad*	1.566	1.560	1.529	0.000	0.016	0.310	0.000
T(Pr)P							
αβαβ_jiji	1.799	1.795	0.000	1.795	0.000	0.000	0.000
αβαβ_ijjj	1.858	1.852	0.049	1.850	0.037	0.049	0.037
αβαβ_iiii	1.907	1.901	0.092	1.898	0.069	0.000	0.000
αβαβ_iijj	1.908	1.903	0.000	1.901	0.000	0.090	0.000
αααα_*sad*	1.676	1.668	1.655	0.000	0.211	0.000	0.000
ααββ_*sad*	1.538	1.532	1.498	0.013	0.016	0.318	0.000
ααββ_*wav*	0.464	0.430	0.000	0.008	0.000	0.430	0.000
T(Pe)P							
αβαβ_jiji	1.797	1.793	0.000	1.793	0.000	0.000	0.000
αβαβ_ijjj	1.864	1.859	0.044	1.857	0.036	0.038	0.049
αβαβ_iiii	1.909	1.903	0.083	1.900	0.069	0.000	0.000
αβαβ_iijj	1.905	1.899	0.004	1.897	0.000	0.091	0.000
αααα_*sad*	1.685	1.678	1.665	0.007	0.210	0.000	0.000
ααββ_*sad*	1.579	1.573	1.543	0.000	0.016	0.308	0.000
ααββ_*wav*	0.462	0.428	0.004	0.004	0.000	0.000	0.428
T(Me)P							
αβαβ	1.892	1.885	0.000	1.885	0.000	0.000	0.000
αααα_*sad*	0.871	0.824	0.737	0.000	0.368	0.000	0.000
αααα_*dom*	0.487	0.386	0.040	0.000	0.384	0.000	0.000
ααββ	0.608	0.563	0.064	0.000	0.002	0.559	0.000
T(cPr)P							
αβαβ	1.857	1.850	0.000	1.850	0.000	0.000	0.000
αααβ	1.562	1.546	0.001	1.492	0.214	0.244	0.244
αααα	0.575	0.457	0.000	0.031	0.456	0.000	0.000

ααββ	0.557	0.521	0.000	0.000	0.001	0.521	0.000
T(iPr)P							
αβαβ	2.245	2.236	0.099	2.233	0.000	0.000	0.000
αααα_*sad*	1.519	1.453	1.334	0.000	0.577	0.000	0.032
αααα_*dom*	0.785	0.615	0.012	0.013	0.614	0.000	0.000
ααββ	0.962	0.891	0.093	0.008	0.004	0.886	0.018
T(cH)P							
αβαβ	2.281	2.271	0.102	2.269	0.000	0.000	0.000
αααα	0.838	0.659	0.011	0.006	0.659	0.000	0.000
ααββ	1.023	0.949	0.125	0.069	0.006	0.938	0.012
T(tBu)P							
αβαβ	2.764	2.743	0.000	2.743	0.000	0.000	0.000
αααβ	2.320	2.267	0.000	2.005	0.601	0.617	0.617
αααα	1.455	1.195	0.015	0.000	1.195	0.000	0.000
ααββ	1.543	1.433	0.004	0.000	0.000	1.433	0.000

[a] Total out-of-plane deformation (in Å) calculated using all 21 out-of-plane modes.

[b] Total out-of-plane deformation (in Å) calculated using the 6 lowest-energy out-of-plane modes.

[c] Deformation in the lowest-frequency mode of each symmetry type (the A_{1u} *pro* mode is generally insignificant and is not shown).

[d] Secondary conformations were obtained for the primary alkyl groups due to the different positions possible for the second carbon in the alkyl chain; i and j are used to specify the relative orientations of the second carbons in the alkyl chain.

Table B-3. Selected structural parameters from MM structures of low-spin 4-coordinate nickel tetraalkylporphyrins.

Porphyrin Conformer	Ni-N bond (Å)	Ruf Angle (deg)[a]	π-overlap Angle (deg)[b]	NC$_\alpha$-C$_\beta$C$_\beta$ Angle (deg)	C$_\alpha$NC$_\alpha$ Angle (deg)	N-Ni-N Angle (deg)	C$_\beta$-C$_\beta$ Bond (Å)	C$_\alpha$-C$_m$ Bond (Å)	C$_\alpha$-N Bond (Å)
NiTPP									
ruf	1.924	30.7	12.7	1.9	105.2	180.0	1.327	1.386	1.382
sad	1.949	0.6	4.9	2.4	104.5	175.8	1.322	1.385	1.385
planar	1.955	0.1	0.1	0.1	104.4	179.9	1.320	1.384	1.387
NiT(Et)P									
αβαβ_jiji[c]	1.908	37.4	16.2	2.1	105.7	180.0	1.328	1.390	1.382
αααα_*sad*	1.938	0.0	7.5	3.6	104.8	173.6	1.322	1.389	1.386
ααββ_*sad*	1.939	1.1	8.4	3.3	104.8	174.0	1.322	1.389	1.386
NiT(Pr)P									
αβαβ_jiji	1.908	37.1	16.0	2.1	105.7	180.0	1.328	1.390	1.382
αααα_*sad*	1.938	0.0	7.5	3.6	104.8	173.6	1.322	1.389	1.386
ααββ_*sad*	1.939	1.1	8.4	3.3	104.8	174.1	1.322	1.389	1.386
ααββ_*wav*	1.949	1.4	9.6	1.7	104.6	180.0	1.319	1.388	1.389
NiT(Pe)P									
αβαβ_jiji	1.908	37.1	16.0	2.1	105.7	180.0	1.328	1.390	1.382
αααα_*sad*	1.938	0.1	7.6	3.6	104.8	173.5	1.322	1.389	1.386
ααββ_*sad*	1.938	1.1	8.4	3.3	104.8	174.0	1.322	1.389	1.386
ααββ_*wav*	1.949	1.5	9.5	1.7	104.6	180.0	1.319	1.388	1.389
NiT(Me)P									
αβαβ	1.902	39.1	17.9	1.1	105.8	180.0	1.331	1.389	1.379
αααα_*sad*	1.946	0.0	12.4	2.6	104.6	177.1	1.321	1.386	1.387
αααα_*dom*	1.949	0.0	13.5	2.7	104.5	178.0	1.320	1.386	1.387
ααββ	1.946	0.0	12.8	4.5	104.6	179.7	1.322	1.386	1.386
NiT(cPr)P									
αβαβ	1.904	38.3	105.7	180.0	1.331	1.387	1.379	17.9	0.9
αααβ	1.918	31.0	105.3	178.9	1.328	1.386	1.381	15.7	2.1
αααα	1.947	0.5	104.5	177.5	1.323	1.384	1.385	15.4	3.2
ααββ	1.943	2.1	104.6	180.0	1.323	1.384	1.384	15.0	3.1
NiT(iPr)P									
αβαβ	1.883	46.1	22.3	1.0	106.5	180.0	1.331	1.394	1.379
αααα_*sad*	1.936	0.3	19.7	3.7	104.9	175.0	1.322	1.389	1.386
αααα_*dom*	1.944	0.2	21.4	4.3	104.6	176.6	1.320	1.389	1.387
ααββ	1.396	3.5	20.4	3.7	104.8	179.9	1.322	1.390	1.386
NiT(cH)P									
αβαβ	1.881	46.8	22.7	1.0	106.6	179.9	1.331	1.395	1.379
αααα	1.943	0.1	22.6	4.6	104.7	176.4	1.320	1.389	1.387
ααββ	1.934	3.8	21.4	3.9	104.9	179.9	1.322	1.390	1.386
NiT(tBu)P									
αβαβ	1.845	56.6	31.2	1.6	107.7	180.0	1.336	1.401	1.375
αααβ	1.877	41.8	32.5	4.7	106.5	176.4	1.332	1.394	1.377
αααα	1.931	0.0	37.1	6.9	104.8	173.0	1.326	1.388	1.382
ααββ	1.912	7.7	34.0	6.7	105.4	180.0	1.329	1.393	1.380

[a] C_α-N-N-C_α torsion angle.

[b] N-C_α-C_m-C_α torsion angle.

[c] Secondary conformations were obtained for the primary alkyl groups due to the different positions possible for the second carbon in the alkyl chain; i and j are used to specify the relative orientations of the second carbons in the alkyl chain.

Table B-4. Energies (kcal mol^{-1}) of stable conformers calculated for the high-spin 4-coordinate nickel tetraalkylporphyrins.

Porphyrin	relat. E	total	bond	angle	torsn	inversn	van der Waal	electr
TPP	n/a	175.40	10.41	72.81	40.00	0.00	59.74	-7.57
T(Et)P αβαβ	0	127.27	9.30	75.96	5.64	0.10	28.79	7.49
αααβ	0.74	128.01	9.20	76.48	4.52	0.08	30.25	7.49
αααα	1.07	128.34	9.07	76.84	3.59	0.04	31.31	7.50
ααββ	1.18	128.45	9.14	76.85	3.59	0.06	31.31	7.50
T(Pr)P αβαβ	0	130.42	9.96	76.27	5.57	0.10	33.36	5.16
αααβ	0.83	131.25	9.85	76.81	4.42	0.08	34.86	5.22
αααα	1.18	131.60	9.72	77.15	3.60	0.04	35.84	5.25
ααββ	1.30	131.72	9.80	77.17	3.55	0.07	35.87	5.26
T(Pe)P αβαβ	0	143.90	11.19	77.38	5.65	0.10	43.00	6.57
αααβ	0.80	144.70	11.08	77.95	4.37	0.08	44.60	6.62
αααα	1.14	145.04	10.95	78.29	3.55	0.04	45.57	6.64
ααββ	1.27	145.17	11.02	78.30	3.57	0.07	45.56	6.66
T(Me)P αβαβ	0	116.52	8.08	74.07	7.44	0.16	25.36	1.41
αααβ	1.12	117.64	7.85	74.74	6.48	0.15	26.99	1.43
αααα	1.62	118.14	7.47	75.16	5.73	0.09	28.23	1.47
ααββ	1.90	118.42	7.70	75.30	5.33	0.12	28.52	1.46
T(cPr)P αβαβ	0	627.51	7.89	564.36	28.55	0.21	20.19	6.30
αααβ	1.50	629.01	7.41	564.93	28.50	0.23	21.63	6.31
αααα	1.70	629.21	6.93	565.12	28.41	0.18	22.26	6.32
ααββ	2.44	629.95	7.35	565.31	28.18	0.22	22.59	6.31
T(iPr)P αβαβ	0	143.56	13.99	83.52	16.79	0.11	34.78	-5.62
αααα	4.08	147.64	12.06	85.32	17.77	0.14	37.86	-5.52
ααββ	4.83	148.39	12.74	85.64	16.84	0.40	38.26	-5.49
T(cH)P αβαβ	0	176.44	18.05	85.41	18.12	0.11	55.59	-0.84
αααα	4.48	180.92	15.82	87.22	19.84	0.17	58.64	-0.79
ααββ	5.36	181.80	16.67	87.55	18.71	0.49	59.15	-0.77
T(tBu)P αβαβ	0	177.92	28.42	88.54	38.22	0.04	58.32	-35.61
αααβ	3.32	181.24	23.07	87.90	46.97	1.55	57.39	-35.64
αααα	2.03	179.95	19.02	87.22	52.96	0.83	55.52	-35.60
ααββ	8.80	186.72	23.27	88.38	48.93	2.70	59.07	-35.63

Table B-5. Energies (kcal mol^{-1}) of stable conformers calculated for the high-spin 5-coordinate (mono-pyrrolidine) nickel tetraalkylporphyrins.

Porphyrin	relat. E	total[a]	bond	angle	torsn	invers	van der Waal	electr
TPP 0[b]	0	181.22	10.87	78.08	45.50	0.04	56.45	-9.73
45	0.52	181.74	10.82	79.08	45.27	0.02	56.35	-9.81
T(Et)P αβαβ 45	0	133.38	9.61	82.52	10.49	0.11	26.06	4.60
αααβ 0	0.42	133.80	9.56	82.01	9.63	0.08	27.90	4.63
αααα 0	0.60	133.98	9.44	82.00	9.24	0.07	28.65	4.57
αααα 45	1.17	134.53	9.41	83.01	8.98	0.04	28.57	4.53
ααββ 0	0.81	134.19	9.62	82.16	8.93	0.11	28.68	4.69
ααββ 45	1.35	134.73	9.56	83.12	8.71	0.10	28.60	4.64
T(Pr)P αβαβ 45	0	136.42	10.27	82.82	10.44	0.11	30.53	2.25
αααβ 0	0.73	137.15	10.22	82.32	9.56	0.11	32.52	2.42
αααα 0	0.89	137.31	10.10	82.31	9.22	0.07	33.14	2.47
αααα 45	1.44	137.86	10.06	83.31	8.94	0.04	33.09	2.42
ααββ 0	1.05	137.47	10.25	82.48	8.95	0.17	33.21	2.40
T(Pe)P αβαβ 45	0	149.69	11.49	83.96	10.37	0.12	40.21	3.55
αααβ 0	0.58	150.27	11.43	83.45	9.48	0.09	42.12	3.70
αααα 0	0.89	150.58	11.31	83.45	9.20	0.07	42.81	3.73
αααα 45	1.44	151.13	11.28	84.44	8.90	0.04	42.79	3.68
ααββ 0	0.70	150.39	11.51	83.58	8.91	0.07	42.61	3.72
T(Me)P αβαβ 45	0	123.46	8.39	80.71	12.43	0.16	22.79	-1.01
αααβ 0	0.91	124.37	8.15	80.37	11.57	0.17	25.00	-0.90
αααβ 45	1.88	125.34	8.09	81.16	10.94	0.10	25.94	-0.87
αααα 0	0.97	124.43	7.82	80.26	11.42	0.12	25.66	-0.86
αααα 45	1.49	124.95	7.81	81.27	11.14	0.09	25.56	-0.93
ααββ 0	1.70	125.16	8.16	80.63	10.69	0.24	26.33	-0.88
T(cPr)P αβαβ 45	0	632.85	8.18	570.90	34.04	0.20	16.20	3.34
αααβ (ligand α, 0)[c]	0.94	633.79	7.69	570.30	34.10	0.23	18.08	3.38
αααβ (ligand β, 45)[d]	2.20	635.05	7.92	571.27	33.83	0.32	18.29	3.43
αααα (ligand α, 0)	0.54	633.39	7.23	570.07	34.36	0.19	18.20	3.35
αααα (ligand β, 0)	3.47	636.06	7.88	570.67	33.49	0.30	20.20	3.51
ααββ 0[e]	2.37	635.19	7.80	570.62	33.83	0.24	19.27	3.43
T(iPr)P αβαβ 45	0	149.08	14.12	90.38	22.12	0.09	30.92	-8.55
αααα 0	2.77	151.85	12.37	90.15	23.78	0.26	33.84	-8.56
ααββ 0	4.55	153.63	13.24	91.15	22.22	0.28	35.05	-8.29

T(cH)P αβαβ 45	0	181.60	18.13	92.25	23.71	0.09	51.22	-3.79
αααα 0	3.44	185.04	16.14	91.99	26.05	0.26	54.32	-3.73
ααββ 0	4.94	186.54	17.01	92.67	24.78	0.52	55.21	-3.64
T(tBu)P αβαβ 45	0	183.51	28.21	96.08	43.42	0.15	53.96	-38.30
αααβ 45	1.82	185.33	23.59	93.84	52.58	1.59	52.15	-38.42
αααα 0	0.51	184.02	20.21	90.95	58.84	1.58	50.79	-38.33
αααα 45	1.19	184.70	20.26	91.90	58.60	1.43	50.76	-38.26
ααββ 0	8.66	192.17	24.15	95.01	53.75	1.95	55.50	-38.19
ααββ 45	8.55	192.06	24.11	94.60	53.78	2.20	55.58	-38.21

[a] In all cases, the energy from the hydrogen bonding term was zero.

[b] 0 and 45 indicate that the N-H bond of the ligand sits along or between the Ni-N(porphyrin) bonds, respectively.

[c] N-H eclipses Ni-N bond closest to β cPr.

[d] N-H points in same direction as middle α cPr (*i.e.*, away from β cPr).

[e] Energies of structures with NHs between αα or ββ substituents are similar.

Table B-6. Energies (kcal mol^{-1}) of all the stable conformers calculated for the high-spin 6-coordinate (bis-pyrrolidine) nickel(II) tetraalkylporphyrins.

Porphyrin Conformers	rel. E	total[a]	bond	angle	torsn	inversion	van der Waals	electr
TPP perp 0[b]	0	188.33	11.91	83.65	50.88	0.09	53.42	-11.62
perp 45	0.91	189.24	11.68	85.72	50.57	0.05	52.96	-11.74
para 0	0.64	188.97	12.15	83.01	50.72	0.10	54.44	-11.45
para 45	1.34	189.67	11.83	85.58	50.02	0.01	53.91	-11.68
T(Et)P αβαβ perp 45	0	140.51	10.34	89.37	15.22	0.10	23.51	1.96
αβαβ para 45	1.80	142.31	10.74	89.43	13.58	0.04	26.48	2.05
αααβ perp 0	0.34	140.85	10.69	87.83	14.46	0.11	25.71	2.05
αααβ perp 45	0.67	141.18	10.40	89.57	14.62	0.10	24.53	1.97
αααβ para 45	1.96	142.47	10.64	89.72	13.21	0.04	26.81	2.04
αααα perp 0	0.52	141.03	10.65	87.73	14.17	0.17	26.27	2.05
αααα para 0	1.22	141.73	10.91	87.08	13.94	0.15	27.43	2.23
αααα perp 45	1.39	141.90	10.42	89.88	13.78	0.10	25.75	1.97
αααα para 45	1.96	142.47	10.58	89.65	13.21	0.07	26.92	2.05
ααββ perp 0	0.51	141.02	10.70	87.74	14.16	0.11	26.24	2.07
ααββ para 0	1.02	141.53	10.97	87.05	14.09	0.05	27.12	2.26
ααββ perp 45	1.43	141.94	10.50	89.92	13.72	0.07	25.75	1.98
ααββ para 45	2.04	142.55	10.64	89.74	13.10	0.04	26.98	2.05
T(Pr)P αβαβ perp 45	0	143.45	11.00	89.67	15.24	0.11	27.82	-0.39
αβαβ para 45	1.89	145.34	11.39	89.73	13.60	0.05	30.80	-0.23
αααβ perp 0	0.40	143.85	11.34	88.14	14.44	0.11	30.05	-0.24
αααβ perp 45	0.71	144.16	11.06	89.85	14.61	0.11	28.87	-0.34
αααβ para 45	2.02	145.47	11.29	90.04	13.17	0.05	31.17	-0.25
αααα perp 0	0.59	144.04	11.29	88.04	14.16	0.17	30.60	-0.23
αααα para 0	1.28	144.73	11.56	87.39	13.91	0.15	31.77	-0.04
αααα perp 45	1.48	144.93	11.07	90.18	13.74	0.10	30.14	-0.30
αααα para 45	2.01	145.46	11.23	89.96	13.21	0.07	31.24	-0.24
ααββ perp 0	0.57	144.02	11.35	88.05	14.16	0.11	30.56	-0.21
ααββ para 0	1.39	144.84	11.59	87.44	13.95	0.15	31.76	-0.04
ααββ perp 45	1.52	144.97	11.14	90.23	13.66	0.08	30.16	-0.30
ααββ para 45	2.10	145.55	11.29	90.04	13.11	0.05	31.30	-0.24
T(Pe)P αβαβ perp 45	0	157.81	12.28	92.54	15.45	0.11	36.45	0.99
αβαβ para 45	1.87	159.68	12.67	92.61	13.78	0.05	39.43	1.13
αααβ perp 0	0.48	158.29	12.55	91.09	14.75	0.19	38.60	1.10
αααβ perp 45	0.66	158.47	12.40	92.37	14.94	0.13	37.60	1.03
αααβ para 45	2.00	159.81	12.57	92.88	13.56	0.05	39.65	1.11
αααα perp 0	0.56	158.37	12.57	90.89	14.47	0.17	39.14	1.13
αααα para 0	1.25	159.06	12.84	90.25	14.22	0.15	40.30	1.31
αααα perp 45	1.44	159.25	12.35	93.03	13.95	0.10	38.76	1.05

αααα para 45	1.98	159.79	12.51	92.82	13.48	0.07	39.79	1.11
ααββ perp 0	0.54	158.35	12.63	90.91	14.45	0.11	39.10	1.15
ααββ para 0	1.35	159.16	12.86	90.30	14.25	0.15	40.28	1.32
ααββ perp 45	1.50	159.31	12.42	93.08	13.90	0.08	38.77	1.06
ααββ para 45	2.06	159.87	12.56	92.93	13.40	0.05	39.82	1.11
T(Me)P αβαβ perp 45	0	131.33	9.11	87.68	17.22	0.14	20.48	-3.30
αβαβ para 45	2.36	133.69	9.52	87.79	15.42	0.07	24.02	-3.12
αααβ perp 0	1.11	132.44	9.32	86.69	16.48	0.14	22.98	-3.17
αααβ para 45	2.76	134.09	9.28	88.23	15.22	0.08	24.45	-3.17
αααα perp 0	1.38	132.71	9.20	86.14	16.17	0.21	24.13	-3.13
αααα para 0	2.01	133.34	9.43	85.49	16.10	0.20	25.07	-2.96
αααα perp 45	2.11	133.44	8.99	88.32	15.71	0.16	23.51	-3.24
αααα para 45	2.73	134.06	9.10	88.04	15.39	0.12	24.56	-3.15
ααββ perp 0	1.48	132.81	9.33	86.29	16.01	0.13	24.17	-3.11
ααββ para 0	2.17	133.50	9.53	85.69	15.90	0.19	25.16	-2.97
ααββ para 45	2.78	134.11	9.24	88.36	15.00	0.08	24.81	-3.18
T(cPr)P αβαβ perp 45	0	639.28	8.86	577.81	39.31	0.16	12.46	0.69
αααβ perp 45	1.79	641.07	8.62	577.65	39.34	0.25	14.45	0.76
αααα perp 0	2.09	641.37	8.66	575.94	39.36	0.27	16.35	0.79
ααββ perp 0	2.51	641.79	8.90	576.24	39.26	0.19	16.38	0.81
T(iPr)P αβαβ perp 45	0	155.73	14.67	97.57	27.13	0.06	27.44	-11.13
αααα perp 0	4.27	160.00	13.96	96.46	27.86	0.38	32.24	-10.89
αααα para 0	4.96	160.69	14.16	95.73	27.95	0.37	33.19	-10.71
αααα perp 45	5.13	160.86	13.84	98.76	26.85	0.27	32.08	-10.93
ααββ para 0	6.81	162.54	15.05	95.70	27.72	0.17	34.48	-10.58
T(cH)P αβαβ perp 45	0	187.99	18.65	99.36	28.92	0.06	47.34	-6.34
αααα perp 0	4.67	192.66	17.76	98.12	30.22	0.44	52.32	-6.19
ααββ perp 0	5.06	193.06	18.23	98.73	29.35	0.35	52.55	-6.16
T(tBu)P αβαβ perp 45	0.00	191.08	28.94	103.82	47.51	0.22	51.17	-40.57
αααβ perp 45	2.62	193.70	25.40	102.83	56.20	1.04	49.13	-40.91
αααα perp 0	3.66	194.74	23.22	97.74	62.35	1.81	50.03	-40.41
αααα para 0	4.20	195.28	23.33	96.98	62.52	1.90	50.78	-40.24
αααα perp 45	4.16	195.24	23.05	98.66	61.97	1.73	50.27	-40.44
αααα para 45	5.03	196.11	23.17	99.59	61.56	1.56	50.61	-40.38
ααββ perp 0	8.66	199.74	25.62	101.46	58.24	1.94	52.79	-40.31
ααββ para 0	8.70	199.78	26.08	101.20	58.11	1.36	53.26	-40.24
ααββ perp 45	8.01	199.09	25.27	100.36	58.35	2.72	52.92	-40.54
ααββ para 45	7.76	198.84	24.24	98.22	60.08	4.15	52.63	-40.49

[a] In all cases, the energy from the hydrogen bonding term was zero.

[b] 0 and 45 indicate that the N-H bond of the ligand sits along or between the Ni-N(porphyrin) bonds, respectively. Para and perp indicate the relative orientations (parallel or perpendicular) of the planes of the axial ligands.

Table B-7. Out-of-plane displacements (in Å) obtained from normal-coordinate structural decomposition of stable conformers calculated for the high-spin 4-coordinate nickel tetraalkylporphyrins.

Porphyrin	total		*sad*[c]	*ruf*	*dom*	*wav(x)*	*wav(y)*
	obs[a]	fit[b]					
TPP	0.018	0.018	0.000	0.018	0.000	0.000	0.000
T(Et)P αβαβ	0.921	0.915	0.000	0.915	0.000	0.000	0.000
αααβ	0.665	0.655	0.000	0.620	0.114	0.125	0.125
αααα	0.296	0.252	0.000	0.000	0.252	0.000	0.000
ααββ	0.310	0.292	0.000	0.021	0.000	0.291	0.000
T(Pr)P αβαβ	0.918	0.912	0.000	0.912	0.000	0.000	0.000
αααβ	0.647	0.637	0.000	0.599	0.116	0.129	0.129
αααα	0.298	0.255	0.000	0.000	0.255	0.000	0.000
ααββ	0.309	0.291	0.000	0.005	0.000	0.291	0.000
T(Pe)P αβαβ	0.929	0.923	0.000	0.923	0.000	0.000	0.000
αααβ	0.641	0.631	0.000	0.593	0.117	0.129	0.129
αααα	0.297	0.255	0.009	0.006	0.255	0.000	0.000
ααββ	0.310	0.292	0.000	0.005	0.000	0.292	0.000
T(Me)P αβαβ	1.093	1.085	0.000	1.085	0.000	0.000	0.000
αααβ	0.843	0.829	0.000	0.777	0.170	0.166	0.166
αααα	0.442	0.382	0.006	0.000	0.382	0.000	0.000
ααββ	0.427	0.402	0.006	0.009	0.000	0.000	0.402
T(cPr)P αβαβ	1.168	1.158	0.000	1.158	0.000	0.000	0.001
αααβ	0.842	0.816	0.000	0.693	0.249	0.249	0.249
αααα	0.578	0.502	0.000	0.000	0.502	0.000	0.000
ααββ	0.557	0.521	0.000	0.000	0.001	0.521	0.000
T(iPr)P αβαβ	1.590	1.576	0.117	1.572	0.000	0.000	0.000
αααα	0.781	0.665	0.010	0.009	0.665	0.000	0.000
ααββ	0.792	0.746	0.000	0.004	0.000	0.014	0.746
T(cH)P αβαβ	1.655	1.640	0.083	1.638	0.000	0.000	0.000
αααα	0.842	0.719	0.000	0.000	0.719	0.000	0.000
ααββ	0.853	0.806	0.009	0.037	0.000	0.805	0.019
T(tBu)P αβαβ	2.281	2.250	0.000	2.250	0.000	0.000	0.000
αααβ	1.950	1.889	0.000	1.439	0.767	0.675	0.675
αααα	1.610	1.422	0.006	0.000	1.422	0.000	0.000
ααββ	1.506	1.436	0.002	0.000	0.000	1.436	0.000

[a] Total out-of-plane deformation (in Å) calculated using all 21 out-of-plane modes.

[b] Total out-of-plane deformation (in Å) calculated using the 6 lowest-energy out-of-plane modes.

[c] Deformation in the lowest-frequency mode of each symmetry type (the A_{1u} *pro* mode is generally insignificant and is not shown).

Table B-8. Out-of-plane displacements (in Å) obtained from normal-coordinate structural decomposition of the stable conformers calculated for the high-spin 5-coordinate (mono-pyrrolidine) nickel tetraalkylporphyrins.

Porphyrin	total		*sad*[c]	*ruf*	*dom*	*wav(x)*	*wav(y)*
Conformer	observed[a]	fit[b]					
TPP 0[d]	0.175	0.167	0.137	0.003	0.095	0.005	0.000
45	0.210	0.209	0.000	0.200	0.059	0.011	0.010
T(Et)P αβαβ 45	0.893	0.887	0.017	0.886	0.043	0.008	0.007
αααβ 0	0.621	0.609	0.247	0.491	0.176	0.131	0.141
αααα 0	0.430	0.402	0.271	0.000	0.297	0.000	0.000
αααα 45	0.393	0.362	0.000	0.232	0.278	0.006	0.006
ααββ 0	0.431	0.418	0.302	0.026	0.068	0.004	0.280
ααββ 45	0.389	0.378	0.022	0.245	0.054	0.002	0.282
T(Pr)P αβαβ 45	0.892	0.886	0.036	0.884	0.042	0.005	0.010
αααβ 0	0.632	0.623	0.279	0.494	0.177	0.125	0.137
αααα 0	0.428	0.400	0.266	0.000	0.298	0.000	0.000
αααα 45	0.378	0.345	0.000	0.200	0.281	0.006	0.006
ααββ 0	0.470	0.463	0.354	0.011	0.071	0.290	0.000
T(Pe)P αβαβ 45	0.886	0.880	0.036	0.879	0.042	0.009	0.006
αααβ 0	0.595	0.583	0.251	0.454	0.177	0.143	0.134
αααα 0	0.436	0.409	0.280	0.000	0.298	0.000	0.000
αααα 45	0.366	0.332	0.004	0.175	0.282	0.006	0.006
ααββ 0	0.406	0.389	0.264	0.043	0.073	0.273	0.003
T(Me)P αβαβ 45	1.071	1.062	0.015	1.061	0.052	0.008	0.011
αααβ 0	0.787	0.771	0.215	0.657	0.238	0.181	0.165
αααβ 45	0.588	0.566	0.000	0.416	0.254	0.203	0.203
αααα 0	0.519	0.469	0.210	0.000	0.419	0.000	0.000
αααα 45	0.511	0.459	0.000	0.231	0.397	0.006	0.006
ααββ 0	0.525	0.511	0.301	0.005	0.085	0.404	0.000
T(cPr)P αβαβ	1.176	1.165	0.000	1.164	0.036	0.009	0.009
αααβ (ligand α)	0.831	0.804	0.191	0.632	0.291	0.260	0.241
αααβ (ligand β)	0.861	0.835	0.000	0.731	0.185	0.254	0.254
αααα (ligand α)	0.616	0.541	0.172	0.001	0.513	0.007	0.000
αααα (ligand β)	0.555	0.465	0.264	0.000	0.383	0.013	0.000
ααββ	0.599	0.562	0.202	0.009	0.060	0.521	0.007
T(iPr)P αβαβ 45	1.559	1.544	0.057	1.542	0.049	0.008	0.018
αααα 0	0.883	0.781	0.413	0.000	0.664	0.005	0.001
ααββ 0	0.811	0.759	0.221	0.010	0.075	0.722	0.014
T(cH)P αβαβ 45	1.630	1.613	0.042	1.612	0.044	0.010	0.016
αααα 0	0.858	0.734	0.157	0.057	0.715	0.014	0.005
ααββ 0	0.894	0.846	0.186	0.014	0.063	0.823	0.006
T(tBu)P αβαβ 45	2.213	2.179	0.012	2.175	0.129	0.027	0.029
αααβ 45	1.905	1.840	0.090	1.397	0.706	0.669	0.692

αααα 0	1.559	1.363	0.078	0.000	1.361	0.014	0.000
αααα 45	1.547	1.347	0.000	0.099	1.343	0.000	0.000
ααββ 0	1.465	1.383	0.009	0.000	0.092	1.380	0.000
ααββ 45	1.485	1.408	0.230	0.064	0.090	1.384	0.003

[a] Total out-of-plane deformation (in Å) calculated using all 21 out-of-plane modes.

[b] Total out-of-plane deformation (in Å) calculated using the 6 lowest-energy out-of-plane modes.

[c] Deformation in the lowest-frequency mode of each symmetry type (the A_{1u} *pro* mode is generally insignificant and is not shown).

[d] 0 and 45 indicate that the N-H bond of the ligand sits along or between the Ni-N(porphyrin) bonds, respectively.

Table B-9. Out-of-plane displacements (in Å) obtained from normal-coordinate structural decomposition of the stable conformers calculated for the high-spin 6-coordinate (bis-pyrrolidine) nickel tetraalkylporphyrins.

Porphyrin Conformer	total		*sad*[c]	*ruf*	*dom*	*wav(x)*	*wav(y)*
	observed[a]	fit[b]					
TPP perp 0[d]	0.233	0.221	0.221	0.002	0.000	0.004	0.004
perp 45	0.401	0.400	0.055	0.396	0.000	0.003	0.017
para 0	0.080	0.024	0.000	0.021	0.000	0.011	0.000
para 45	0.032	0.029	0.011	0.000	0.000	0.019	0.019
T(Et)P αβαβ perp 45	0.873	0.867	0.024	0.866	0.000	0.000	0.013
αβαβ para 45	0.549	0.541	0.000	0.539	0.041	0.017	0.017
αααβ perp 0	0.763	0.755	0.170	0.716	0.090	0.089	0.111
αααβ perp 45	0.755	0.747	0.135	0.716	0.090	0.110	0.090
αααβ para 45	0.379	0.364	0.003	0.298	0.130	0.116	0.115
αααα perp 0	0.605	0.587	0.546	0.002	0.215	0.002	0.015
αααα para 0	0.283	0.234	0.081	0.000	0.220	0.006	0.000
αααα perp 45	0.558	0.544	0.007	0.508	0.192	0.006	0.016
αααα para 45	0.262	0.219	0.000	0.003	0.218	0.015	0.016
ααββ perp 0	0.572	0.559	0.499	0.034	0.006	0.251	0.005
ααββ para 0	0.297	0.262	0.004	0.017	0.262	0.000	0.000
ααββ perp 45	0.576	0.569	0.000	0.527	0.000	0.215	0.000
ααββ para 45	0.274	0.000	0.000	0.000	0.000	0.255	0.020
T(Pr)P αβαβ perp 45	0.879	0.873	0.042	0.872	0.000	0.002	0.013
αβαβ para 45	0.556	0.549	0.000	0.547	0.042	0.018	0.017
αααβ perp 0	0.677	0.665	0.477	0.419	0.102	0.115	0.124
αααβ perp 45	0.758	0.750	0.150	0.715	0.092	0.112	0.091
αααβ para 45	0.374	0.359	0.000	0.291	0.131	0.117	0.117
αααα perp 0	0.606	0.588	0.546	0.005	0.218	0.003	0.015
αααα para 0	0.286	0.238	0.085	0.007	0.222	0.006	0.000
αααα perp 45	0.545	0.529	0.003	0.419	0.197	0.005	0.016
αααα para 45	0.264	0.222	0.000	0.003	0.220	0.016	0.016
ααββ perp 0	0.571	0.559	0.497	0.004	0.006	0.255	0.007
ααββ para 0	0.296	0.271	0.000	0.003	0.000	0.271	0.003
ααββ perp 45	0.560	0.552	0.020	0.506	0.000	0.002	0.222
ααββ para 45	0.276	0.258	0.000	0.000	0.000	0.020	0.257
T(Pe)P αβαβ perp 45	0.867	0.861	0.011	0.861	0.000	0.000	0.012
αβαβ para 45	0.537	0.529	0.000	0.527	0.040	0.018	0.018
αααβ perp 0	0.701	0.693	0.509	0.414	0.108	0.141	0.134
αααβ perp 45	0.771	0.764	0.298	0.680	0.098	0.121	0.090
αααβ para 45	0.393	0.379	0.007	0.316	0.132	0.114	0.114
αααα perp 0	0.602	0.584	0.540	0.047	0.218	0.002	0.015
αααα para 0	0.284	0.237	0.081	0.010	0.222	0.000	0.005
αααα perp 45	0.521	0.504	0.004	0.463	0.201	0.005	0.014

αααα para 45	0.262	0.222	0.003	0.007	0.220	0.017	0.015
ααββ perp 0	0.574	0.562	0.501	0.036	0.006	0.007	0.252
ααββ para 0	0.295	0.271	0.004	0.000	0.000	0.004	0.271
ααββ perp 45	0.538	0.531	0.004	0.480	0.000	0.000	0.227
ααββ para 45	0.274	0.256	0.000	0.009	0.000	0.017	0.256
T(Me)P αβαβ perp 45	1.045	1.036	0.000	1.036	0.000	0.016	0.000
αβαβ para 45	0.749	0.738	0.008	0.735	0.062	0.018	0.020
αααβ perp 0	0.814	0.795	0.384	0.639	0.140	0.180	0.155
αααβ para 45	0.554	0.531	0.002	0.433	0.193	0.168	0.169
αααα perp 0	0.609	0.566	0.466	0.007	0.321	0.002	0.014
αααα para 0	0.411	0.338	0.094	0.006	0.325	0.008	0.000
αααα perp 45	0.617	0.581	0.036	0.495	0.302	0.014	0.004
αααα para 45	0.394	0.326	0.000	0.014	0.325	0.016	0.016
ααββ perp 0	0.589	0.564	0.424	0.000	0.008	0.004	0.372
ααββ para 0	0.421	0.405	0.000	0.003	0.000	0.000	0.405
ααββ para 45	0.401	0.372	0.000	0.000	0.000	0.371	0.021
T(cPr)P αβαβ	1.176	1.164	0.000	1.164	0.000	0.000	0.016
αααβ	0.905	0.879	0.149	0.760	0.209	0.252	0.257
αααα	0.661	0.587	0.406	0.006	0.423	0.016	0.008
ααββ	0.657	0.614	0.362	0.010	0.003	0.496	0.008
T(iPr)P αβαβ perp 45	1.512	1.495	0.007	1.495	0.000	0.007	0.023
αααα perp 0	0.900	0.802	0.564	0.004	0.571	0.003	0.024
αααα para 0	0.739	0.608	0.196	0.007	0.576	0.004	0.020
αααα perp 45	0.841	0.742	0.006	0.508	0.540	0.011	0.020
ααββ para 0	0.771	0.703	0.121	0.004	0.008	0.012	0.692
T(cH)P αβαβ perp 45	1.585	1.567	0.033	1.567	0.001	0.021	0.022
αααα perp 0	0.971	0.866	0.604	0.036	0.619	0.022	0.004
ααββ para 0	0.945	0.895	0.449	0.017	0.011	0.774	0.005
T(tBu)P αβαβ perp 45	1.869	1.824	0.135	1.819	0.001	0.021	0.022
αααβ perp 45	1.780	1.701	0.080	1.321	0.573	0.630	0.643
αααα perp 0	1.524	1.320	0.521	0.017	1.212	0.013	0.041
αααα para 0	1.488	1.273	0.378	0.007	1.215	0.000	0.055
αααα perp 45	1.459	1.241	0.159	0.182	1.216	0.035	0.014
αααα para 45	1.428	1.204	0.002	0.017	1.203	0.022	0.022
ααββ perp 0	1.456	1.378	0.051	0.160	0.009	1.365	0.005
ααββ para 0	1.418	1.326	0.000	0.004	0.000	0.000	1.326
ααββ perp 45	1.552	1.487	0.510	0.111	0.007	0.006	1.392
ααββ para 45	1.560	1.500	0.000	0.000	0.000	0.016	1.500

[a] Total out-of-plane deformation (in Å) calculated using all 21 out-of-plane modes.

[b] Total out-of-plane deformation (in Å) calculated using the 6 lowest-energy out-of-plane modes.

[c] Deformation in the lowest-frequency mode of each symmetry type (the A_{1u} *pro* mode is generally insignificant and is not shown).

[d] 0 and 45 indicate that the N-H bond of the ligand sits along or between the Ni-N(porphyrin) bonds, respectively. Para and perp indicate the relative orientations (parallel or perpendicular) of the planes of the axial ligands.

Table B-10. Selected structural parameters from MM structures of high-spin 4-coordinate nickel tetraalkylporphyrins.

Porphyrin	Ni-N bond (Å)	Ruf angle (deg)[a]	π-overlap angle (deg)[b]	N-C_α-C_β-C_β angle (deg)	C_α-N-C_α angle (deg)	N-Ni-N angle (deg)	C_β-C_β bond (Å)	C_α-C_m bond (Å)	C_α-N bond (Å)
NiTPP	2.042	0.4	0.2	0.0	107.4	180.0	1.331	1.400	1.380
NiT(Et)P αβαβ	2.028	17.9	10.6	0.3	107.8	180.0	1.331	1.404	1.380
αααβ	2.034	12.2	8.1	0.9	107.6	178.9	1.329	1.404	1.382
αααα	2.040	0.0	7.4	1.1	107.5	177.6	1.328	1.404	1.383
ααββ	2.039	1.7	6.9	1.2	107.5	180.0	1.328	1.404	1.382
NiT(Pr)P αβαβ	2.028	17.9	10.6	0.3	107.8	180.0	1.331	1.404	1.380
αααβ	2.036	11.8	8.0	0.9	107.6	178.9	1.329	1.404	1.382
αααα	2.040	0.0	7.5	1.1	107.5	177.6	1.328	1.404	1.382
ααββ	2.039	1.8	6.8	1.2	107.5	180.0	1.328	1.404	1.382
NiT(Pe)P αβαβ	2.028	18.1	10.6	0.4	107.8	180.0	1.331	1.404	1.380
αααβ	2.035	11.6	8.0	0.9	107.6	178.9	1.329	1.404	1.382
αααα	2.040	0.1	7.2	1.1	107.5	177.6	1.328	1.404	1.382
ααββ	2.039	1.8	1.8	1.2	107.5	180.0	1.328	1.404	1.382
NiT(Me)P αβαβ	2.023	21.3	13.2	0.2	107.9	180.0	1.333	1.403	1.378
αααβ	2.030	15.3	10.8	1.1	107.7	178.3	1.332	1.402	1.380
αααα	2.039	0.0	10.9	1.6	107.4	176.2	1.330	1.402	1.381
ααββ	2.037	2.5	9.6	1.8	107.5	180.0	1.330	1.403	1.381
NiT(cPr)P αβαβ	2.020	22.7	14.7	0.5	107.9	180.0	1.335	1.401	1.377
αααβ	2.030	13.6	13.8	1.7	107.6	177.4	1.333	1.400	1.378
αααα	2.038	0.0	14.2	2.0	107.4	174.9	1.332	1.399	1.379
ααββ	2.034	3.1	13.0	2.6	107.5	180.0	1.332	1.400	1.379
NiT(iPr)P αβαβ	2.005	30.7	19.7	0.4	108.5	179.9	1.334	1.407	1.378
αααα	2.037	0.1	19.9	2.9	107.5	173.3	1.329	1.404	1.381
ααββ	2.031	5.0	17.8	3.1	107.7	180.0	1.329	1.405	1.382
NiT(cH)P αβαβ	2.002	32.0	20.5	0.4	108.6	179.8	1.334	1.408	1.378
αααα	2.037	0.0	21.2	3.0	107.5	172.6	1.328	1.404	1.382
ααββ	2.029	5.7	18.9	6.5	107.7	180.0	1.329	1.406	1.382
NiT(tBu)P αβαβ	1.966	43.9	31.5	3.0	109.7	180.0	1.340	1.413	1.374
αααβ	2.005	28.4	33.9	4.0	108.4	170.3	1.337	1.407	1.376
αααα	2.043	0.0	38.1	4.5	107.3	163.1	1.333	1.401	1.378
ααββ	2.014	13.4	33.3	5.6	108.1	180.0	1.335	1.406	1.376

[a] C_α-N-N-C_α torsion angle.

[b] N-C_α-C_m-C_α torsion angle.

Table B-11. Selected structural parameters from MM structures of high-spin 5-coordinate (mono-pyrrolidine) nickel tetraalkylporphyrins.

Porphyrin	$Ni-N_P$ bond (Å)	$Ni-N_{ax}$ bond (Å)	Ruf angle (deg)[a]	π-overlap angle (deg)[b]	$NC_\alpha-C_\beta C_\beta$ angle (deg)	$NNi-N_{ax}H$ angle (deg)	$C_\alpha-N-C_\alpha$ angle (deg)	N-Ni-N angle (deg)	$C_\beta-C_\beta$ bond (Å)	$C_\alpha-C_m$ bond (Å)	$C_\alpha-N$ bond (Å)
NiTPP											
0[c]	2.044	2.129	1.3	2.8	1.1	0.0	107.3	175.9	1.331	1.400	1.380
45	2.042	2.126	4.0	2.0	0.3	45.0	107.4	176.1	1.331	1.400	1.379
NiT(Et)P											
αβαβ 45	2.030	2.123	17.3	10.4	0.4	43.8	107.7	176.5	1.331	1.404	1.381
αααβ 0	2.038	2.127	9.6	8.2	1.1	9.8	107.6	175.5	1.329	1.404	1.382
αααα 0	2.041	2.126	1.2	8.3	1.4	0.0	107.5	175.2	1.328	1.403	1.382
ααββ 0	2.040	2.129	2.9	6.5	1.5	2.9	107.5	175.9	1.328	1.404	1.382
NiT(Pr)P											
αβαβ 45	2.030	2.123	17.3	10.3	0.4	42.2	107.7	176.4	1.330	1.404	1.380
αααβ 0	2.038	2.127	9.6	8.0	0.9	6.9	107.6	175.5	1.329	1.404	1.382
αααα 0	2.042	2.158	1.2	7.7	1.0	0.1	107.5	175.1	1.328	1.404	1.382
ααββ 0	2.041	2.129	3.2	6.4	1.0	0.2	107.5	175.9	1.328	1.404	1.382
NiT(Pe)P											
αβαβ 45	2.030	2.123	17.2	10.4	0.8	42.7	107.7	176.4	1.330	1.404	1.381
αααβ 0	2.038	2.127	8.9	8.0	1.1	9.0	107.5	175.5	1.329	1.404	1.382
αααα 0	2.042	2.126	1.2	8.1	0.8	0.1	107.5	175.2	1.328	1.404	1.382
ααββ 0	2.040	2.130	1.0	6.5	1.4	0.6	107.5	175.8	1.328	1.404	1.382
NiT(Me)P											
αβαβ 45	2.029	2.142	18.7	13.3	0.4	43.8	107.8	174.5	1.333	1.402	1.379
αααβ 0	2.041	2.130	4.8	4.2	0.6	3.3	107.5	175.7	1.328	1.403	1.383
αααα 0	2.042	2.129	2.5	4.4	0.5	0.1	107.5	175.7	1.328	1.404	1.383
ααββ 0	2.039	2.129	3.9	9.3	1.6	0.4	107.5	175.8	1.330	1.403	1.381
T(cPr)P											
αβαβ	2.021	2.123	22.7	15.2	0.5	45.0	107.9	176.4	1.335	1.401	1.377
αααβ (ligand α)	2.033	2.127	12.3	14.2	1.7	5.7	107.6	175.0	1.333	1.400	1.378
αααα (ligand α)	2.039	2.123	1.2	14.7	1.8	0.0	107.4	174.3	1.332	1.399	1.379
ααββ	2.036	2.130	4.1	13.2	2.6	7.1	107.5	175.8	1.332	1.400	1.384
NiT(iPr)P											
αβαβ 45	2.018	2.123	29.9	20.0	0.5	43.3	108.4	176.2	1.334	1.407	1.378
αααα 0	2.036	2.120	1.3	20.1	2.7	0.0	107.6	173.9	1.329	1.404	1.382
ααββ 0	2.031	2.130	3.5	17.7	3.3	0.1	107.7	175.7	1.330	1.406	1.381
NiT(cH)P											
αβαβ 45	2.005	2.123	31.3	21.0	0.5	43.9	108.5	176.2	1.334	1.407	1.378
αααα 0	2.036	2.121	1.8	21.7	2.9	0.9	107.5	173.6	1.329	1.404	1.382
ααββ 0	2.031	2.131	6.4	19.3	3.4	9.5	107.7	175.6	1.330	1.406	1.381
NiT(tBu)P											
αβαβ 45	1.973	2.124	42.0	31.6	3.2	44.7	109.5	174.9	1.339	1.413	1.375
αααβ 45	2.002	2.115	27.4	34.1	4.2	34.9	108.5	173.7	1.337	1.407	1.375
ααββ 0	2.014	2.132	10.8	33.2	6.0	0.0	108.2	175.2	1.335	1.407	1.376
ααββ 45	2.014	2.134	12.3	33.1	5.7	19.6	108.2	174.9	1.335	1.407	1.376

[a] C_α-N-N-C_α torsion angle.

[b] N-C_α-C_m-C_α torsion angle.

[c] 0 and 45 indicate that the N-H bond of the ligand sits along or between the Ni-N(porphyrin) bonds, respectively.

Table B-12. Selected structural parameters from MM structures of high-spin 6-coordinate (bis-pyrrolidine) nickel tetraalkylporphyrins.

Porphyrin	Ni-N_P bond (Å)	Ni-N_{ax} bond (Å)	Ruf angle (deg)[a]	π-overlap angle (deg)[b]	NC_α-$C_\beta C_\beta$ angle (deg)	NNi-N_{ax}H angle (deg)	C_α-N-C_α angle (deg)	N-Ni-N angle (deg)	C_β-C_β bond (Å)	C_α-C_m bond (Å)	C_α-N bond (Å)
NiTPP											
perp 0[c]	2.043	2.142	2.7	1.6	1.3	0.3	107.4	177.5	1.331	1.400	1.380
perp 45	2.041	2.136	8.0	3.7	0.5	42.5	107.4	179.7	1.331	1.400	1.379
para 0	2.044	2.149	2.8	0.6	0.5	0.4	107.4	180.0	1.331	1.400	1.380
para 45	2.043	2.141	1.2	0.6	0.1	45.1	107.4	180.0	1.331	1.400	1.380
NiT(Et)P											
αβαβ perp 45	2.031	2.132	16.9	10.5	0.3	44.5	107.8	179.8	1.331	1.404	1.380
αααβ perp 0	2.038	2.141	8.2	8.0	0.9	8.9	107.7	177.6	1.329	1.404	1.381
αααα perp 0	2.041	2.141	2.6	5.9	0.5	0.5	107.6	177.4	1.328	1.404	1.383
ααββ perp 0	2.040	2.142	1.7	6.1	1.7	0.9	107.6	177.5	1.329	1.404	1.382
NiT(Pr)P											
αβαβ perp 45	2.031	2.133	17.1	10.3	0.3	43.7	107.8	179.8	1.331	1.404	1.381
αααβ perp 0	2.038	2.141	8.1	7.0	1.5	7.8	107.6	177.6	1.329	1.404	1.382
αααα perp 0	2.041	2.141	2.6	6.0	1.6	0.3	107.5	177.4	1.328	1.404	1.383
ααββ perp 0	2.040	2.142	1.8	6.1	1.7	1.8	107.6	177.5	1.329	1.405	1.382
NiT(Pe)P											
αβαβ perp 45	2.031	2.132	16.8	10.4	0.2	44.4	107.8	179.8	1.330	1.404	1.380
αααβ perp 0	2.038	2.140	8.1	6.8	1.4	10.3	107.6	177.6	1.329	1.404	1.382
αααα perp 0	2.046	2.141	2.6	5.9	1.2	0.8	107.5	177.4	1.328	1.404	1.383
ααββ perp 0	2.040	2.142	1.8	6.0	1.7	1.6	107.6	177.5	1.329	1.404	1.383
NiT(Me)P											
αβαβ perp 45	2.026	2.133	20.2	13.1	0.3	44.7	107.9	179.9	1.333	1.403	1.379
αααβ perp 0	2.033	2.141	12.5	10.4	1.7	19.2	107.6	177.9	1.331	1.403	1.381
αααα perp 0	2.039	2.142	2.7	9.5	1.8	0.4	107.5	177.5	1.330	1.403	1.382
ααββ perp 0	2.038	2.143	2.3	9.2	2.8	0.4	107.5	177.6	1.330	1.403	1.382
NiT(cPr)P											
αβαβ perp 45	2.021	2.132	22.5	15.6	0.5	45.0	107.9	179.9	1.335	1.401	1.377
αααβ perp 45	2.029	2.135	14.9	14.4	1.8	36.5	107.5	179.3	1.333	1.400	1.378
αααα perp 0	2.037	2.143	2.7	13.8	2.4	0.3	107.5	177.5	1.332	1.400	1.379
ααββ perp 0	2.035	2.143	2.6	13.3	2.8	3.6	107.5	177.6	1.332	1.401	1.379
NiT(iPr)P											
αβαβ perp 45	2.010	2.133	28.8	20.2	0.6	43.7	108.4	179.8	1.334	1.407	1.379
αααα perp 0	2.035	2.142	2.8	18.4	3.7	0.2	107.7	177.4	1.329	1.405	1.384
ααββ para 0	2.032	2.157	1.6	17.8	3.6	0.2	107.8	179.2	1.330	1.406	1.382
NiT(cH)P											
αβαβ perp 45	2.007	2.133	30.2	21.3	0.4	44.7	108.5	179.9	1.334	1.407	1.378
αααα perp 0	2.034	2.143	2.9	20.0	3.6	0.6	107.7	177.5	1.329	1.406	1.382
ααββ perp 0	2.030	2.144	4.9	18.8	3.6	4.3	107.8	177.7	1.330	1.406	1.381
NiT(tBu)P											
αβαβ perp 45	1.982	2.140	38.5	31.3	3.9	43.8	109.4	179.9	1.338	1.414	1.377
αααβ perp 45	2.000	2.136	25.6	33.4	4.8	37.3	108.6	178.9	1.337	1.409	1.375
αααα perp 0	2.024	2.148	3.5	35.7	5.6	0.9	107.8	177.6	1.334	1.405	1.378
ααββ para 45	2.026	2.151	17.6	33.2	5.3	10.1	108.0	180.0	1.334	1.406	1.378

[a] C_α-N-N-C_α torsion angle.

[b] N-C_α-C_m-C_α torsion angle.

[c] 0 and 45 indicate that the N-H bond of the ligand sits along or between the Ni-N(porphyrin) bonds, respectively. Para and perp indicate the relative orientations (parallel or perpendicular) of the planes of the axial ligands

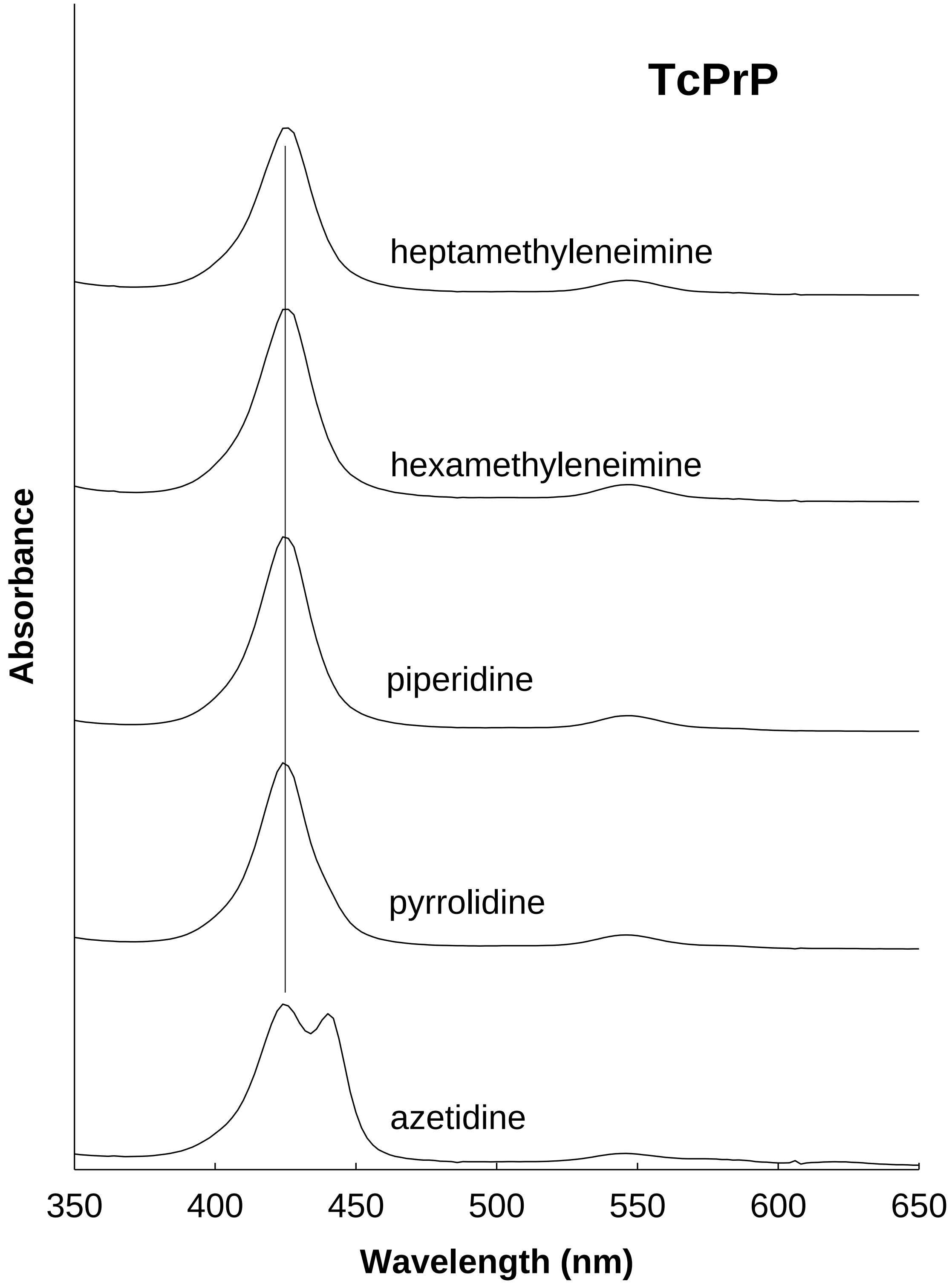
TcPrP
heptamethyleneimine
hexamethyleneimine
piperidine
pyrrolidine
azetidine
Absorbance
350
400
450
500
550
600
650
Wavelength (nm)

[redacted]

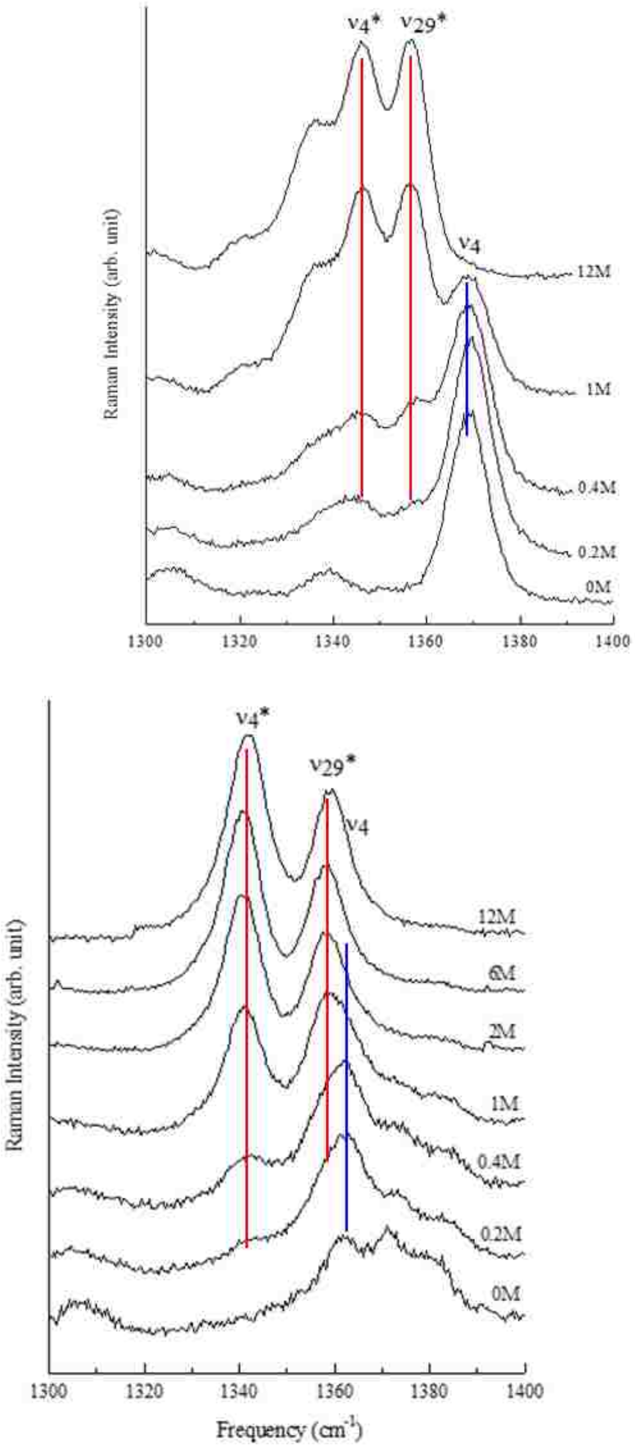

Figure B-2 Resonance Raman spectra for (a) NiT(Pr)P, and (b) NiT(Me)P in benzene with different pyrrolidine concentrations in the frequency region 1300-1400 cm^{-1} using 413.1 nm excitation.

(Note: Spectra collected by Dr. Yujiang Song[61])

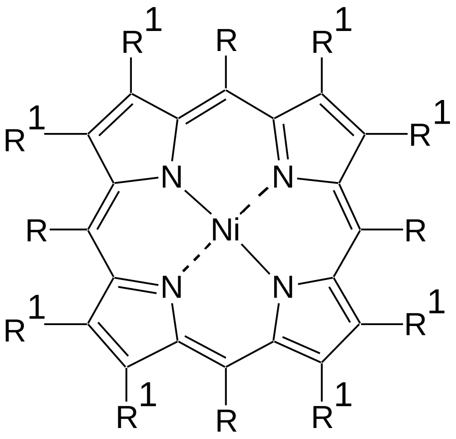

NiTPP R = C_6H_5, R^1 = H

NiOEP R = H, R^1 = CH_2CH_3

NiOETPP R = C_6H_5, R^1 = CH_2CH_3

Ni DPP R = R^1 = C_6H_5

NiOETNP R = NO_2, R^1 = CH_2CH_3

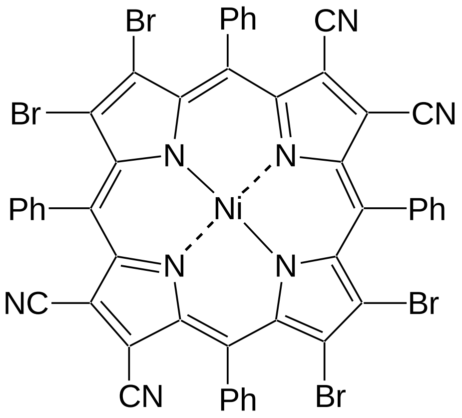

$NiBr_4(CN)_4TPP$

Figure B-3. Structures of several nickel porphyrins with known crystal structures of the 6-coordinate form.